Earth, Life & Social Sciences
Princetonlaan 6
3584 CB Utrecht
P.O. Box 80015
3508 TA Utrecht
The Netherlands

www.tno.nl

T +31 88 866 42 56
F +31 88 866 44 75

TNO report

TNO 2015 R11259

Injection Related Induced Seismicity and its relevance to Nitrogen Injection: Modelling of geomechanical effects of injection on fault stability

Date	11 November 2015
Author(s)	
Copy no	
No. of copies	
Number of pages	123 (incl. appendices)
Number of appendices	4
Sponsor	Nederlandse Aardolie Maatschappij B.V. (NAM)
Project name	
Project number	

Contents

1 Introduction

Pressure maintenance by injection of nitrogen into a reservoir is considered to be one of the potential options to mitigate induced seismicity during gas production. However, injection of nitrogen itself may be the cause of unwanted induced seismicity. At this stage it is unclear what seismic hazards are related to nitrogen injection.

Numerous field cases of injection-related induced seismicity have been described in literature, e.g. related to deep waste water injection, hydraulic fracturing for shale gas, Enhanced Oil and Gas Recovery (EOR and EGR) and Enhanced Geothermal Systems (EGS). NAM requested TNO to perform a generic study to estimate the potential for induced seismicity caused by the injection of nitrogen in a producing gas reservoir and to specify general operational guidelines for nitrogen injection to reduce the potential of injection-related seismicity.

As part of this generic study, a review of the literature on injection-related induced/triggered seismicity worldwide was performed. Results of the literature study have been reported in TNO-report 2014 R11761. In addition, a description and general analysis of a number of injection field cases in The Netherlands has been reported in TNO-report 2015 R10906. Focus of the current report is on geomechanical modelling of the effects of injection of nitrogen for pressure maintenance in a producing reservoir, and the potential consequences for fault reactivation. Since fault reactivation is considered to be the main cause of injection-induced seismicity, this study uses fault reactivation and fault slip (in terms of the amount of slip and size of the slip patches) as a proxy (i.e. indicative estimate) for induced seismicity. The assumption that fault reactivation, and more particularly fault slip lengths, can be used as an indicator of the (induced) seismicity potential is supported by dynamic rupture studies, such as reported in Uenishi et al. (2003) and TNO-report 2015 R10844. These studies show that a minimum nucleation length (i.e. fault slip length) needs to be exceeded for the onset of unstable, seismic fault rupture.

The literature review on injection-induced seismicity revealed that in the majority of the injection-related cases of seismicity, such cases were related to the increase of pore pressures above virgin reservoir pressures. In the Netherlands, when nitrogen injection is used for pressure maintenance, pressures are likely to remain below initial reservoir pressures. When injecting nitrogen for pressure maintenance in a producing reservoir (containing faults which may already be critically stressed during production), faults can potentially be reactivated at pressures below virgin reservoir pressure. At the start of the study presented in this report the following four mechanisms, which can potentially lead to the reactivation of faults, were identified:

- Mechanism 1: Differential pressure evolution and effects of stress arching;
- Mechanism 2: Pore pressure diffusion into faults;
- Mechanism 3: Irreversible stress paths during production and injection;
- Mechanism 4: Cooling and thermal stresses due to injection of nitrogen at injection temperatures lower than ambient reservoir temperatures.

In order to analyze the effects of nitrogen injection on fault stability, a synthetic geomechanical model, representative for a typical Dutch Rotliegend reservoir setting was constructed for each individual mechanism. Several sensitivity runs were performed to analyze the effect of initial stress conditions, fault offset, orientation and strength, injection pressure build up, geomechanical parameters of the reservoir and caprock, and distance of injection to faults. All analysis has been performed with the general purpose finite-element simulator DIANA (DIANA User Manual, 2014).

Geomechanical modelling and results are described in chapter 2 to 5. Each chapter consists of a short description of the mechanism, a description of the modelling approach chosen, the model results, a discussion of the results, and conclusions as they pertain to typical Dutch conditions. Chapter 6 contains the main conclusions, highlighting the main mechanisms which can lead to fault reactivation during injection. The main text of this report is supported by chapter 7 with references and by four appendices A-D which contain all main results for the four mechanisms as obtained for this study. All figures and tables as found in these appendices have been given a specific label referring to the appendix in which they are found (e.g. Figure A 2 is found in Appendix A, Table D 1 in Appendix D, etc.).

2 Mechanism 1: Differential pressure evolution and effects of stress arching

2.1 Description of mechanism

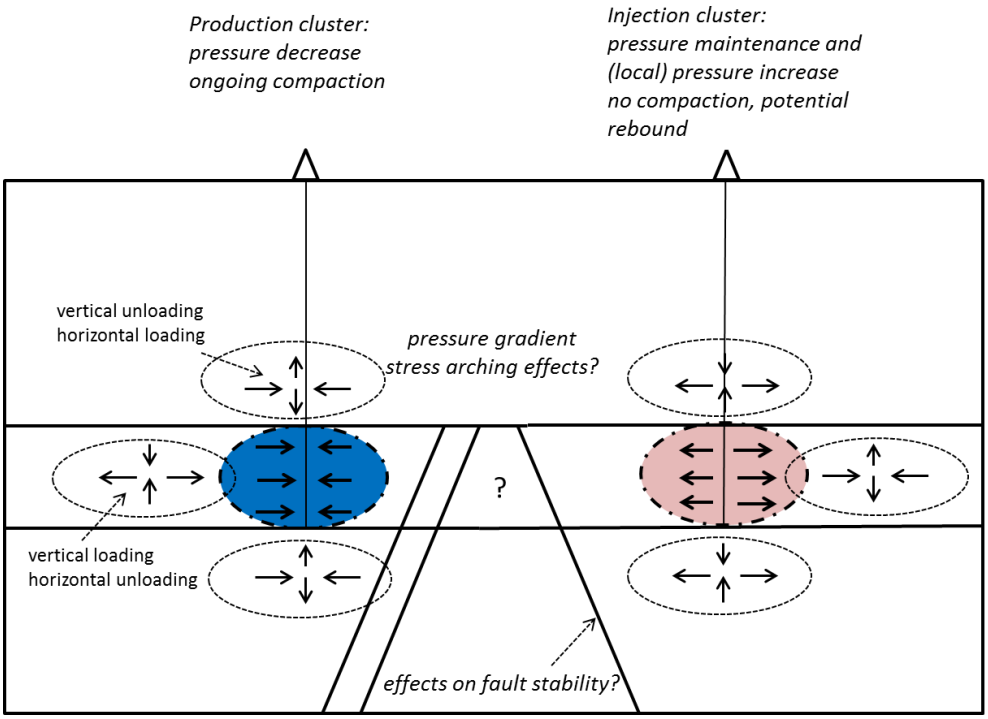

Figure 1: Schematic presentation of the effects of injection for pressure maintenance on stress arching in a producing reservoir.

Due to the injection for pressure maintenance in a producing gas reservoir, pressure gradients develop between the injection and production clusters. While the areas close to the production wells are characterised by ongoing reservoir compaction, the compaction of the reservoir rocks in the injection regions diminishes and a partial rebound of the reservoir rocks can be expected locally around the injection wells (depending on pressure levels and permanent plastic deformation). This differential compaction at reservoir level can potentially lead to stress transfer and stress arching around the regions of production and injection (see Figure 1).

Geomechanical modelling is used to quantify the effects of pressure gradients and differential compaction on fault stability and fault reactivation during nitrogen injection. DIANA models of a synthetic reservoir, representative for a typical Rotliegend sandstone reservoir setting in The Netherlands, are used to quantify the effects on fault stability and fault reactivation for a number of realistic pressure scenarios used for pressure maintenance.

2.2 Modelling approach

Model geometry

Both 2D plane strain and 3D models in DIANA of a typical Rotliegend sandstone synthetic reservoir in the Netherlands are used in this analysis[1]. The 2D and 3D models comprise a flat-lying 150 m thick Rotliegend reservoir at a depth of 2850 m, overlain by a Ten Boer claystone layer and Zechstein rock salt. The reservoir rock is underlain by a Carboniferous underburden. A more detailed specification is found in Table 1. Model sizes are selected in such a way as to minimize the effects of the boundary conditions on stress and deformation. The vertical boundaries of the model are assigned a boundary condition of no horizontal displacement while the bottom of the model has a boundary condition of no vertical displacement. The 2D plane strain model covers a domain of 50 x 10 km. For the 2D model, 8-node quadrilateral plane strain elements (CQ16E, see DIANA User Manual, 2014) are used for modelling with mesh size at reservoir level 25 x 16 m and increasing mesh size away from the reservoir. The horizontal dimensions of the 3D model vary, depending on the wavelength of the production scenarios introduced in the sequel of this section, i.e. 16 x 10 km for the 4 km wavelength scenario 3, 24 x 16 km for the 8 km wavelength scenario 4 and 40 x 28 km for the 16 km wavelength scenario 5. Vertical depth for the 3D model is 5.5 km as to reduce the amount of elements and computational effort. 2D plane strain calculations show that differences between the outcomes of a mesh with 5.5 km and 10 km vertical extent are negligible (see Figure A 4). In case of the 3D model, the twenty-node solid brick element (CHx60, see DIANA User Manual, 2014) is used. The mesh size at reservoir level varies from 50 x 50 x 25 m close to the well to 100 x 50 x 25 m further away from the wells and increases further towards the model boundaries. An outline of the 2D and 3D model geometries is presented in Figure 2. Figure 3 presents the dimensions and configuration of the injection and production wells for the 3D model, in which injection and production wells are located at a distance of 2 km. Additional 3D model geometries with larger distances between injection and production wells are shown in Figure A 1 to Figure A 3.

Geological units and related geomechanical parameters for both the 2D plane strain and 3D model are summarized in Table 1. Geomechanical parameters are average values representative for the rock formations in the northern parts of The Netherlands. All rock units are assumed to deform fully elastically and no plasticity and faults are accounted for in the models.

[1] For all 2D plane strain and 3D models a first quality check of the numerical calculations was performed, in which stress changes for a spatially uniform pressure depletion were found to be equal to the analytical solution for uniform pressure depletion.

Table 1: Lithological units, depth, geomechanical properties and initial pore pressures for the 2D plane strain and 3D geomechanical model.

Lithology	**Depth (m)**	**Density (kg/m^3)**	***E*** **(GPa)**	***v*** **(-)**	***K'$_0$*** **(-)**	**Pore pressure**
Overburden (undifferentiated)	0-2000	2270	10	0.25	0.51	Hydrostatic 0.0115 MPa/m
Zechstein (halite)	2000-2750	2150	35	0.30	1.0	Hydrostatic 0.0115 MPa/m
Zechstein (anhydrite)	2750-2800	2970	70	0.25	1.0	Hydrostatic 0.0115 MPa/m
Ten Boer claystone	2800-2850	2300	40	0.25	0.58	35 MPa (@top Slochteren) Gradient 0.0018 MPa/m
Slochteren sandstone (gas)	2850-2900	2300	15	0.20	0.49	35 MPa (@top Slochteren) Gradient 0.0018 MPa/m
Slochteren sandstone (water)	2900-3000	2300	15	0.20	0.49	35 MPa (@top Slochteren) Gradient 0.0115 MPa/m
Carboniferous	>3000	2300	40	0.25	0.61	Hydrostatic Gradient 0.0115 MPa/m

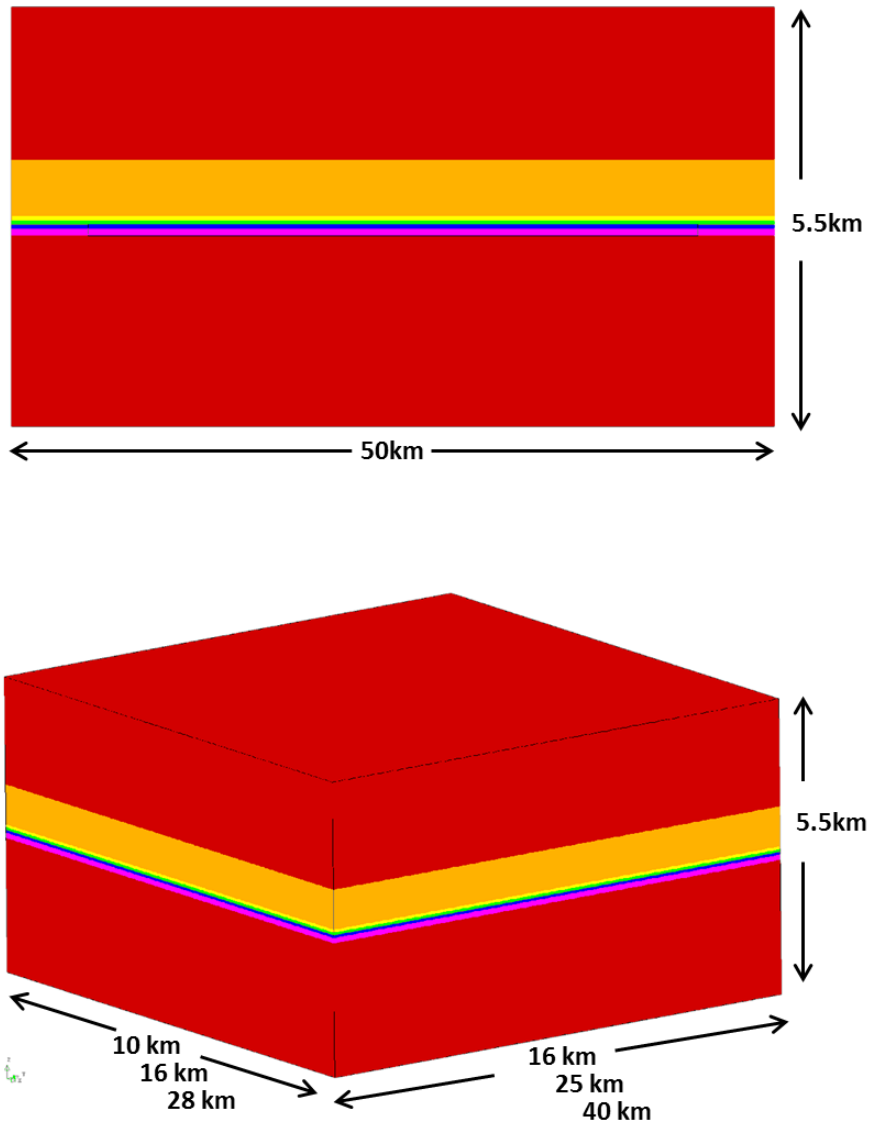

Figure 2: Dimensions and lithological units in the 2D plane strain (top) and 3D model (bottom) in DIANA. Undifferentiated under- and overburden, orange: rocksalt, yellow: Zechstein anhydrite, green: Ten Boer claystone, blue: Slochteren sandstone (gas), magenta: Slochteren sandstone (water). Dimensions of the 3D model depend on the pressure scenario. Three lateral dimensions of the model are shown, resp. for the 4 km, 8 km and 16 km dispersed injection/production scenario.

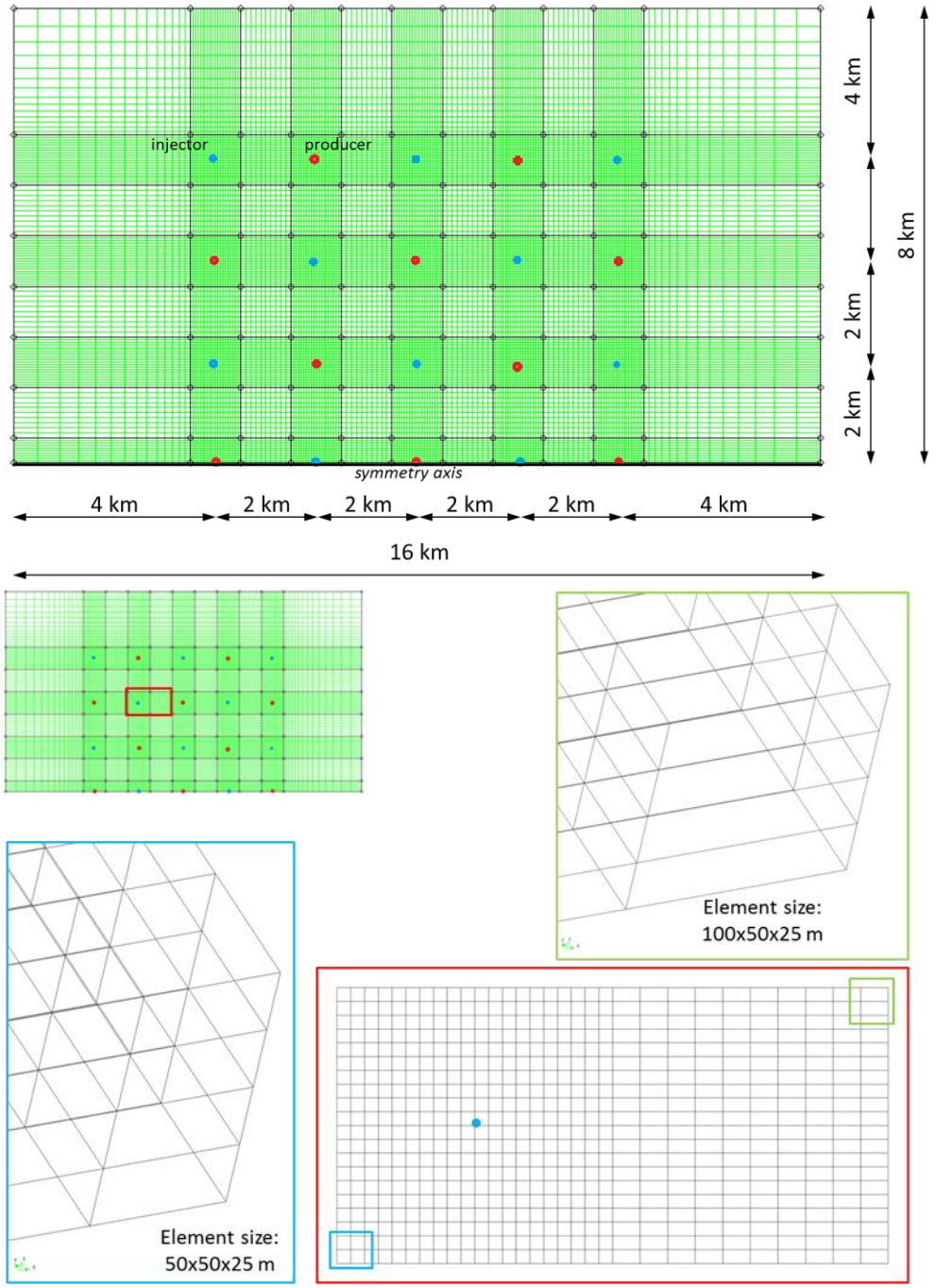

Figure 3: Dimensions and mesh size for the 3D model, 4 km wavelength scenario.

Pressure scenarios

The model geometries described in the previous section are used to analyze the effect of a number of pressure scenarios and related stress arching on fault stability. In total five different pore pressure scenarios have been selected to study the response of the reservoir to differential pore pressures and differential compaction. The initial reservoir pressure is identical for all five pressure scenarios and is found in Table 1.

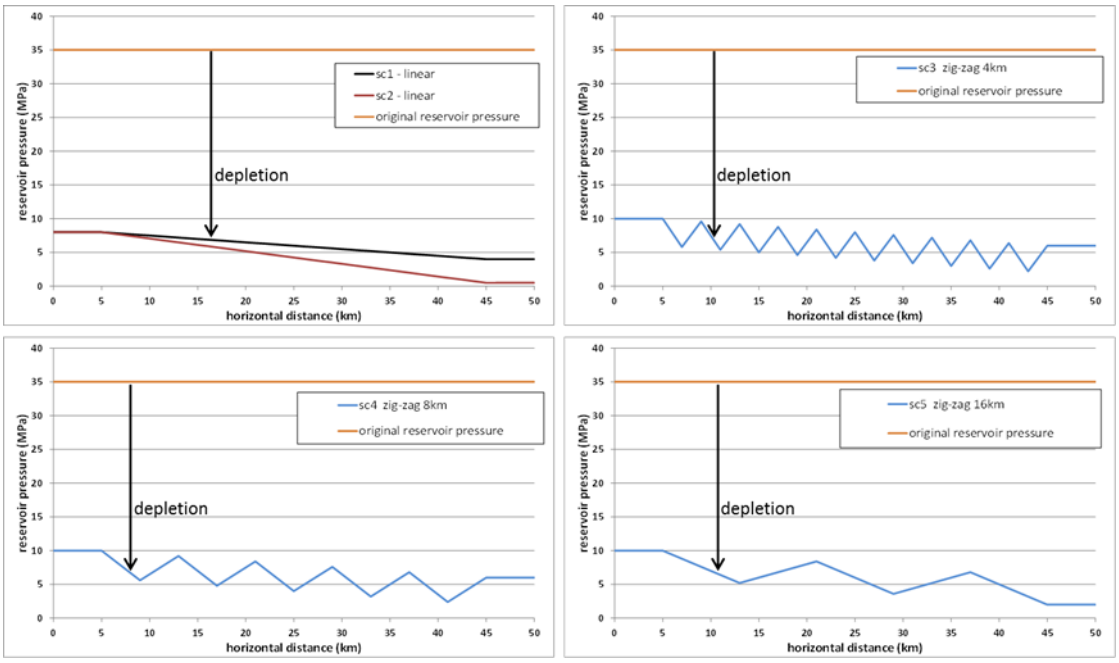

Figure 4: Definition of pressure scenarios for the 2D plane strain model: Clockwise and starting with top display on the left side: Scenarios 1 and 2, scenario 3, scenario 5 and scenario 4.

All details on the five pressure scenarios are given in Table 2. In the first pressure scenario, a linear gradient in pressure depletion is imposed on the Slochteren reservoir (gas and water), with pressure depletion linearly increasing from 27 MPa (left-hand side of the model, Figure 4) to 31 MPa (right-hand side of the model). In pressure scenario 2 the gradient of the depletion profile is steeper, with pressure depletion from 27 MPa to 34.5 MPa. In the 2D plane strain models of scenarios 3 to 5 a dispersed production-injection scenario is imposed on top of the linear pressure gradient of scenario 1, consisting of a zig-zag gradient with an amplitude of 2 MPa. Different wavelengths for this zig-zag gradient were studied: 4 km in scenario 3; 8 km in scenario 4; and 16 km in scenario 5 as shown in Figure 4.

For the 3D model, pressure scenarios 1 and 2 are similar to the ones for the 2D plane strain model. However, scenarios 3 to 5 differ from the 2D model as the imposed pressure gradients between injection and production wells are taken nonlinear, to represent steady state conditions for radial flow around the injection and production wells, according to the relation (Dake, 1978):

$$p(r) - p_E = C[\ln(r) - \ln(r_E)] = C \ln\left[\frac{r}{r_E}\right] \quad (1)$$

In this equation p is pressure, r is the radial distance from the well, r_E is radius of the pressure disturbance, p_E is pressure at distance r_E and the constant C depends on fluid and reservoir properties. In this study the value of C is tuned to the prescribed pressure in the injection and production wells.

Figure 5 shows the lateral pore pressure distributions at the top of the reservoir (according to the three wavelength scenarios) used in the 3D model configuration. Pore pressure changes on a cross section through the injection and production wells for the different 3D scenarios are shown in Figure A 4 to Figure A 8.

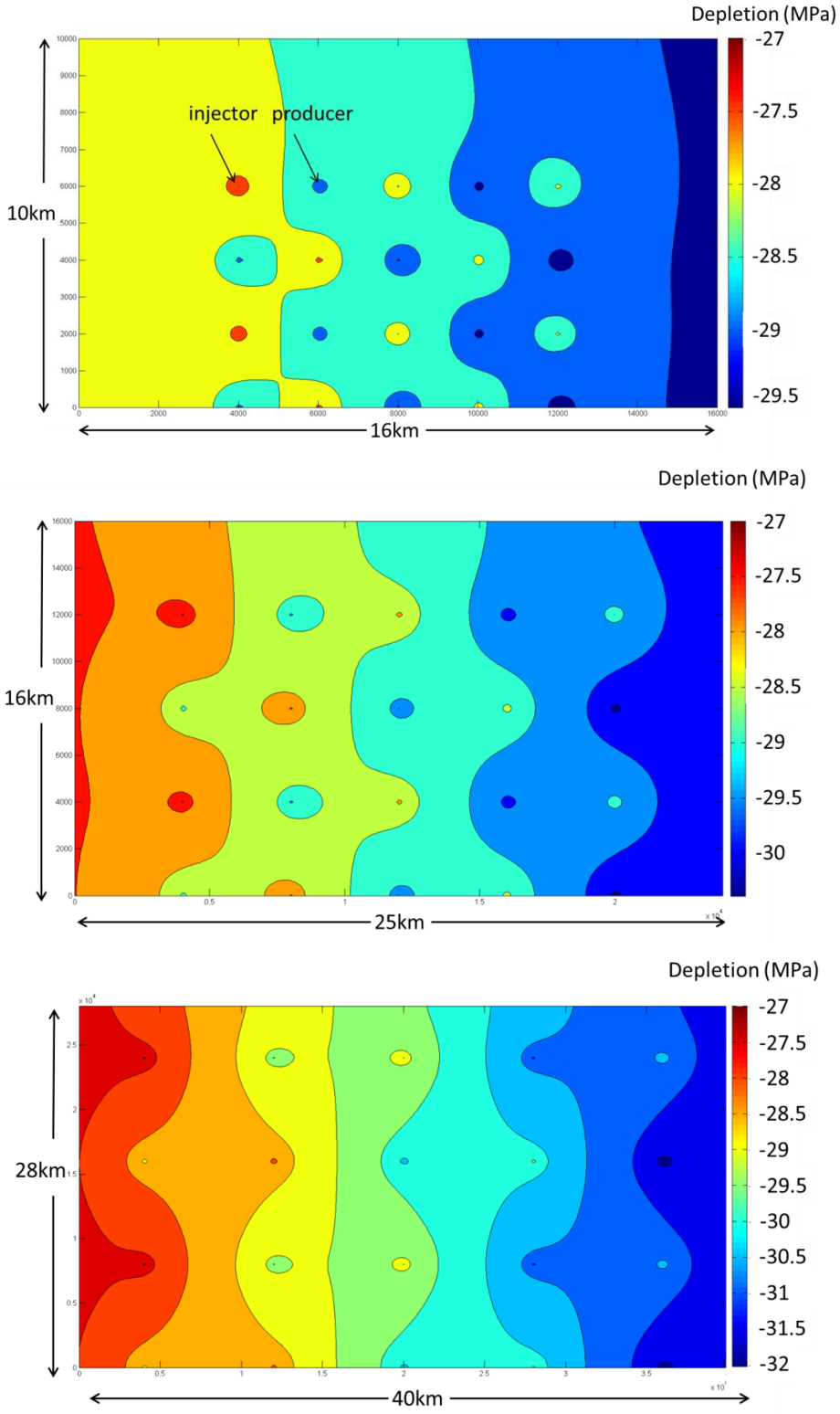

Figure 5: Top view of the dispersed injection-production scenarios for the 3D model in DIANA. Pressures are shown for the top of the reservoir. Top, scenario 3: Wavelength of 4 km, centre, scenario 4: Wavelength of 8 km, bottom, scenario 5: Wavelength of 16 km. On top of the dispersed injection-production scenarios the linear pressure gradient from scenario 1 is imposed to obtain the scenarios shown.

Table 2: Overview of pressure scenarios used for modelling (see also Figure 4).

Scenario	Description of pressure scenario
Scenario 1	Depletion only: Initial reservoir pressure is 35 MPa at top reservoir. 27 MPa depletion (left-hand side) increasing linearly to 31 MPa depletion (right-hand side).
Scenario 2	Depletion only: Initial reservoir pressure is 35 MPa at top reservoir. 27 MPa depletion (left-hand side) increasing linearly to 34.5 MPa depletion (right-hand side).
Scenario 3	Dispersed injection-production scenario: Initial reservoir pressure is 35 MPa at top reservoir. Imposed on top of scenario 1 (linear gradient) is a scenario of alternating injection and production wells. Distance between injection wells (or production wells) is 4 km, resulting in a 'zig-zag' depletion profile with an 'amplitude' of +/- 2 MPa and a 'wavelength' of 4 km.
Scenario 4	Dispersed injection-production scenario: Initial reservoir pressure is 35 MPa at top reservoir. Imposed on top of scenario 1 (linear gradient) is a scenario of alternating injection and production wells. Distance between injection wells (or production wells) is 8 km, resulting in a 'zig-zag' depletion profile with an 'amplitude' of +/- 2 MPa and a 'wavelength' of 8 km.
Scenario 5	Dispersed injection-production scenario: Initial reservoir pressure is 35 MPa at top reservoir. Imposed on top of scenario 1 (linear gradient) is a scenario of alternating injection and production wells. Distance between injection wells (or production wells) is 8 km, resulting in a 'zig-zag' depletion profile with an 'amplitude' of +/- 2 MPa and a 'wavelength' of 16 km.

2.3 Modelling results

2.3.1 Stress arching coefficients

The amount of stress arching caused by the evolution of differential pressures and differential compaction in the reservoir can be quantified by means of the horizontal and vertical stress path coefficients (γ_h and γ_v, respectively) for total stresses, and which are defined as:

$$\gamma_h = \frac{d\sigma_h}{dP} \quad (2)$$

and

$$\gamma_v = \frac{d\sigma_v}{dP} \quad (3)$$

in which dP is the pressure change, $d\sigma_h$ is the change in horizontal total stress and $d\sigma_v$ is the change in vertical total stress.

For all five pressure scenarios, horizontal and vertical stress path coefficients are determined. These stress paths coefficients are compared to the ones for a reservoir with uniform depletion and no differential compaction. When stress path coefficients for the different pressure scenarios are close to the stress path coefficients for uniform depletion, the effects of differential pressure development, differential compaction and stress arching on fault stability are expected to be limited. When large deviations in stress path coefficients are found instead, the

effects of stress arching on fault stability can be significant and need to be further quantified.

For a uniformly depleting horizontal reservoir with a large lateral extent, total stress path coefficients for horizontal and vertical stresses are given by equation (4) and (5) (Mulders, 2003):

$$\gamma_h = \alpha\left(\frac{1-2v}{1-v}\right) \tag{4}$$

$$\gamma_v = 0 \tag{5}$$

in which α is Biot's coefficient, here assumed to be 1, and v is Poisson's ratio, here assumed to be 0.20, a value typical for a Rotliegend reservoir.

For normalization purposes, stress path coefficients for the different pressure scenarios are rewritten to *effective* stress path coefficients γ'_h and γ'_v:

$$\gamma'_h = \frac{d\sigma'_h}{dP} = 1 - \gamma_h \tag{6}$$

and

$$\gamma'_v = \frac{d\sigma'_v}{dP} = 1 - \gamma_v \tag{7}$$

In terms of effective horizontal stresses σ'_h and effective vertical stresses σ'_v, a Poisson's ratio of 0.20 gives a horizontal *effective* stress path coefficient of γ'_h=0.25 and a vertical *effective* stress path coefficient equal to γ'_v=1.0.

Figure 6 presents the minimum and maximum horizontal and vertical effective stress path coefficients computed for the 2D and 3D models for different wavelengths of the pressure gradients. The values are normalized on the horizontal and vertical effective stress path coefficients for a uniformly depleting reservoir. Stress path coefficients for the linear pressure scenarios are not included in Figure 6, but are smaller than for the other scenarios. Results for individual pressure scenarios are also shown in Figure A 5 to Figure A 8.

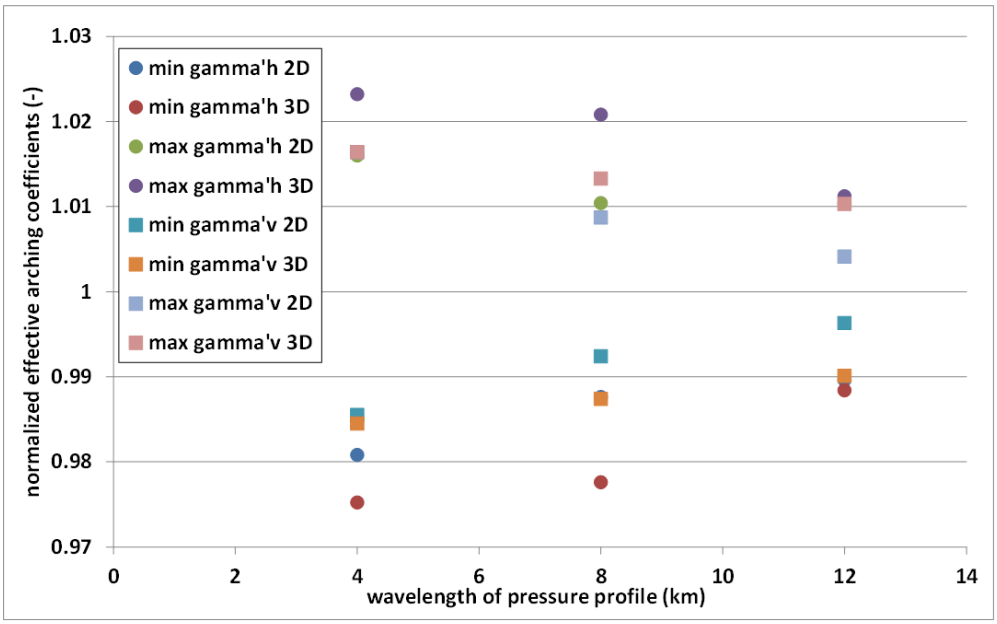

Figure 6: Minimum and maximum normalized effective stress path coefficients computed for the scenarios with dispersed injection and production and wavelengths of 4 km, 8 km and 16 km. These effective stress path coefficients are normalized to a horizontal effective stress path coefficient of γ'_h=0.25 and to a vertical effective stress path coefficient of γ'_v=1.0, respectively. Maximum and minimum values are determined using the data from Figure A5 to Figure A8.

The difference between the effective stress path coefficients for the modelled dispersed injection and depletion pressure scenarios and stress path coefficients for uniform depletion increases with decreasing distance between injection and production wells (i.e. shorter wavelengths). Differences between stress path coefficients computed for the 3D models and uniform depletion are slightly larger than for the 2D models. Stress gradients are steeper in the 3D models than in the 2D models. Hence, arching effects are larger for shorter distances between injection and production wells (i.e. shorter wavelengths) and steeper pressure gradients. However, for all modelled pressure scenarios, the difference between modelled stress path coefficients and coefficients for uniform depletion are very small, with normalized horizontal effective stress path coefficients varying between 0.97 and 1.03 and normalized vertical effective stress path coefficients varying between 0.98 and 1.02.

2.3.2 *Shear capacity utilization*

In addition to the effects on stress path coefficients, the effect of the different pressure gradients on the shear capacity utilization of potential faults are quantified. The shear capacity utilization (SCU) is used as a measure of the proximity of the faults to failure and is defined as:

$$SCU = \frac{\tau}{\tau_{max}} = \frac{\tau}{C+\mu\sigma'_n}\,. \tag{8}$$

In this equation τ is the shear stress, τ_{max} the maximum shear stress, C the cohesion and μ the friction coefficient of the fault. For this analysis, we assume a value of 1 MPa for C and a value of 0.6 for μ.

In Figure 7 for all five scenarios for the 2D plane strain model the shear capacity utilization for a fault dipping 60^0 (near-optimally oriented for failure, when μ=0.6) towards the right-hand side of the model is shown (see also Figure 8). In the same figure the case of a uniform depletion of 27 MPa is included. In all pressure scenarios analyzed, the shear capacity utilization stays well below 1, which suggests that faults remain stable during the injection phase. Differences in SCU caused by the differences in pore pressures are small. In all scenarios shown in Figure 7 modelled SCU varies between 0.8 and 0.85.

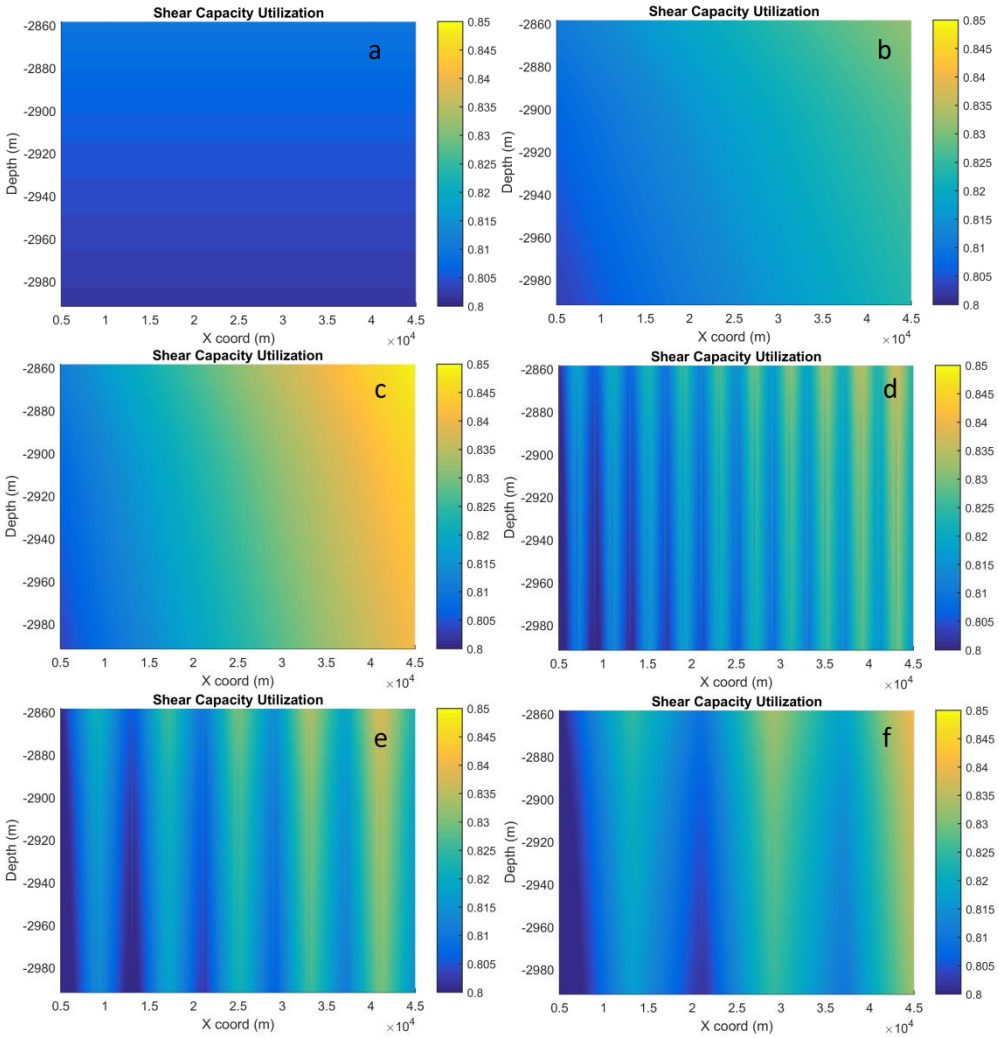

Figure 7: Cross sectional view of the shear capacity utilization computed from the 2D plane strain model in DIANA for pressure scenario: a) uniform depletion from 35 MPa to 8 MPa, b) linear depletion scenario 1, c) linear depletion scenario 2, d) zig-zag depletion, wavelength 4 km scenario 3, e) zig-zag depletion, wavelength 8 km scenario 4, f) zig-zag depletion, wavelength 16 km scenario 5.

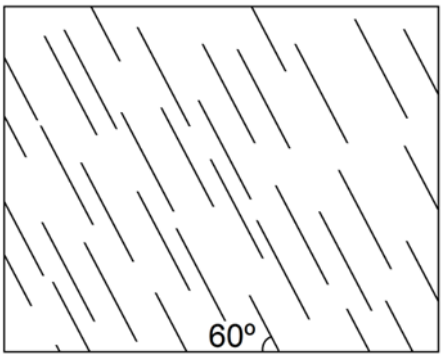

Figure 8: Cartoon displaying the ‘virtual faults’ running through the model. In Figure 7 the SCU is calculated at each point, assuming a fault with 1 MPa cohesion and a coefficient of friction of 0.6 runs through that point with a dip of 60º to the right

2.4 Discussion & conclusions

Both the analysis of the effects of the five pressure scenarios on stress path coefficients and fault shear capacity utilization (SCU) indicate that stress arching effects caused by the imposed pressure gradients and differential compaction are limited. The differences between the maximum/minimum stress path coefficients and coefficients for a uniformly depleting reservoir are computed to be less than 3%. Small differences arise between the 2D and 3D modelling results due to the different gradient of the pressure profile between wells. Based on both the 2D and 3D modelling results, it is concluded that for the modelled pressure scenarios (with wavelengths 4 km and higher, and a fixed amplitude of 2 MPa), the effect of stress arching on fault stability is very small.

Differences between both horizontal and vertical stress path coefficients for uniform depletion and compaction and the differential pressure depletion scenarios increase with decreasing wavelength, i.e. with decreasing distances between injection and production clusters. Stress arching effects may become more significant for distances between injection and production which are smaller, or amplitudes which are higher than modelled in the present study. In this study, only the sensitivity of the stress path coefficients to differential pore pressures (i.e. wavelengths of the pore pressure profiles) is tested. Coefficients can be affected by other parameters than wavelength, such as offset along faults and elasticity parameters of the reservoir and caprock (Van den Bogert, 2015, see also Chapter 3). Such sensitivities have not been addressed here.

3 Mechanism 2: Pressure diffusion into faults

3.1 Description of mechanism

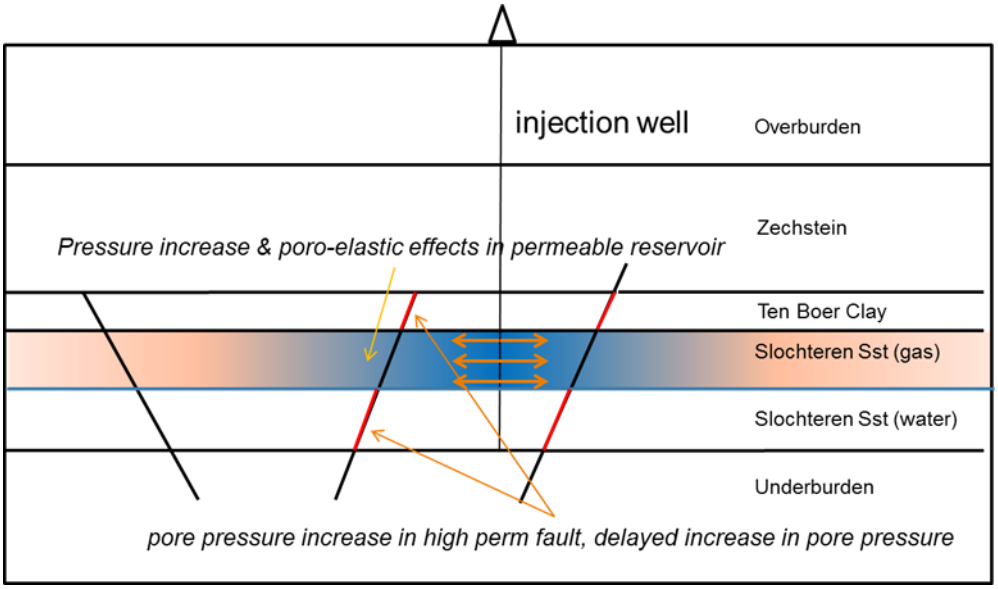

Figure 9: Schematic presentation of mechanism 2: Diffusion of pore pressures into high permeability faults above and below the reservoir, which are bounded by low permeability rocks (e.g. Ten Boer claystone).

A significant number of the field cases of injection-induced seismicity described in literature have been related to an increase of pore pressures within faults. Reported field cases of injection-induced seismicity encompass conditions where the pore pressure increase was due to the injection of fluids directly into the fault or fracture system (e.g. during stimulation of Enhanced Geothermal Systems or hydraulic fracking for shale gas) as well as conditions where the pore pressure increase occurred in faults which were positioned within low permeability rocks, but were hydraulically connected to a permeable reservoir. A recent example of the latter is the injection-induced seismicity caused by the disposal of large volumes of waste water in aquifers in Oklahoma US (see also Ellsworth, 2013 and TNO-report 2014 R11761). One of the concerns related to nitrogen injection into a depleted reservoir is that a similar mechanism of pore pressure increase within the faults might lead to injection-induced seismicity. The case of a local pressure increase (relative to the reservoir rocks) which is caused by a direct injection into a reservoir fault is here considered to be unlikely as fault permeabilities are in the same order of magnitude as permeabilities of the reservoir rocks (in case of cataclasis and clay smearing, fault permeabilities can be lower than reservoir permeabilities) and overpressures in the fault will quickly dissipate into the reservoir rocks. However, as shown below, a local increase in pore pressures due to pressure diffusion into faults which are embedded in a low-permeability matrix, but still hydraulically connected to the reservoir, is possible.

During the primary production phase, high permeability reservoir rocks and high permeability faults hydraulically connected to the reservoir are depleted. During relatively long production periods, less permeable rocks within and on top of the reservoir (e.g. the Ten Boer claystone) are also depleted, see schematic reservoir in Figure 9. When nitrogen is injected into the depleted reservoir, pressures in both the reservoir and the faults within the reservoir will increase and no pressure difference is expected between reservoir and faults. Stress paths on the faults within the reservoir will depend on both the poro-elastic response of the reservoir rocks and the pressures within the faults itself (direct pore pressure effect). Pressure response in the high permeability reservoir rocks and high permeability (open) faults, which are hydraulically connected to the reservoir, is expected to be almost immediate. The pressure response in rocks with a relatively low permeability and diffusivity, such as the Ten Boer claystone, lags behind compared to the pressures in the high permeability faults and reservoir rocks. This means that during injection, faults which are hydraulically connected to the reservoir and which are bounded by these low permeability rocks, will experience a larger pore pressure increase than the surrounding rocks and the effects of the poro-elastic rebound of the surrounding rocks on fault stresses will be limited. During injection, pressures in the faults bounded by the low permeability rocks can be higher than in the surrounding rocks.

Pore pressure diffusion into the faults, which are hydraulically connected to the reservoir, but embedded in low permeability rocks such as the Ten Boer clay will affect the stability of these faults. This effect of pore pressure diffusion and a local increase in fault pressures (relative to the surrounding rocks) on fault stability is analysed in DIANA. In the analysis, the time-dependent pore pressure diffusion and pore pressure increase in the fault and low permeability Ten Boer claystone is not explicitly modelled. Instead, the mechanism of pore pressure diffusion into the fault bounding the Ten Boer clay layer is modelled by imposing 100% of the reservoir pressure change to both the Ten Boer layer and the Ten Boer fault segment during depletion, while during injection applying 100% of the reservoir pressure change to the Ten Boer fault segment and keeping the Ten Boer formation itself at post-depletion pressures. This marked difference in pore pressure within the fault compared to the rest of the formation represents a situation where the fault gouge adjacent to the Ten Boer claystone is in direct communication with the reservoir, whilst due to the low permeability of the Ten Boer claystone no significant pore pressure increase occurs in the Ten Boer claystone itself during (the early stages) of injection. This end-member, where diffusion into the Ten Boer clay is not considered, is used to maximize the effect of differential pore pressures.

3.2 Modelling approach

3.2.1 General model properties

The effects of pore pressure diffusion into faults are investigated using a 2D plane strain model in DIANA[2]. The model of a synthetic reservoir represents a typical Rotliegend sandstone reservoir setting in the Netherlands, consisting of 7

[2] As a quality check of the numerical results, solutions for a model with similar reservoir and fault properties, but no fault offset were compared to the analytical solution for uniform pressure depletion and were found to be similar.

formations of uniform thickness. For modelling a base case scenario is defined. The geometry of the base case scenario is presented in Figure 10 and the depth of the individual layers is presented in Table 3. The model is 4 km wide and 10 km high. The formations are flat-lying and have uniform isotropic properties. A single planar fault with a 75º dip and an offset of 100 m runs through the centre of the model. The fault zone has a uniform width of 1 m. Due to the fault offset of 100 m, in the base case configuration the Ten Boer clay in the hanging wall block is juxtaposed against the Slochteren reservoir sandstone (water), whereas the higher Ten Boer clay in the footwall bock is juxtaposed against the Zechstein rock salt.

Mesh, boundary and loading conditions, material properties of the fault and rocks and results for the base case scenario are presented in section 3.2 and 3.3. In addition to the base case scenario, sensitivities for reservoir and fault material properties, fault offset and loading conditions are analysed, which are described in section 3.4.

In the following sections, a number of points of interest along the fault are used to present the change in criticality and stress paths due to the imposed depletion and injection scheme. These points of interest are chosen based on the juxtaposition of formations across the fault and are therefore dependent on the offset. In Figure 10 the chosen points of interest along the fault are shown for the base case scenario. The labelling introduced for these points is consistently used throughout this report.

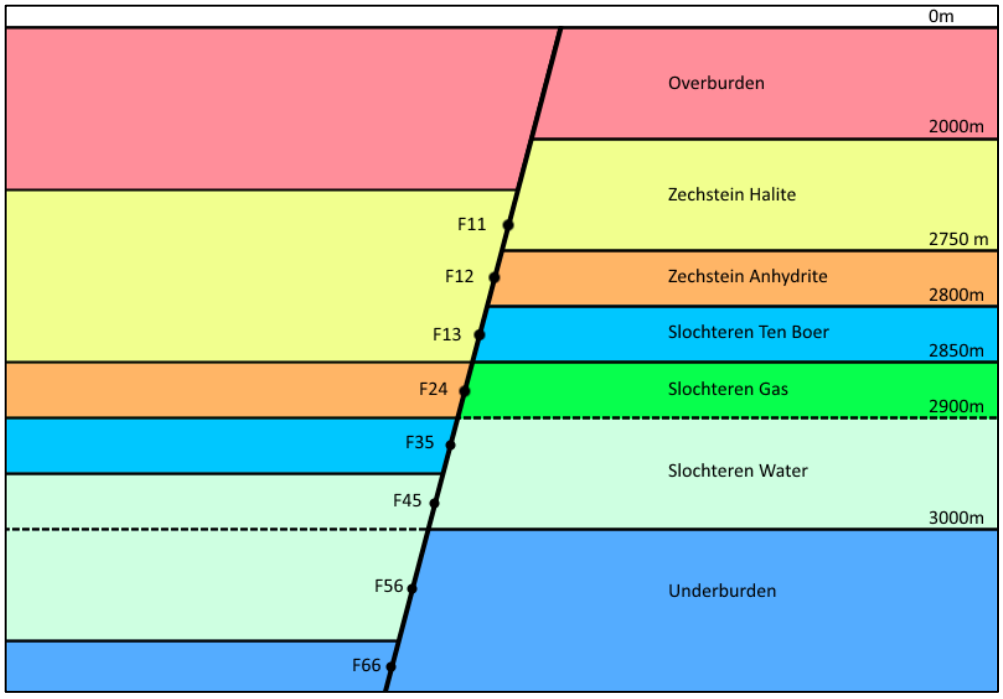

Figure 10: Schematic geometry for 100 m offset base case scenario (not to scale). Points F11 to F56 are chosen in the centre of their respective formation contact. Point F66 is chosen 25 m away from the formation boundary above.

3.2.2 Mesh

The mesh consists of linear elements and is created using the so-called FAULT module, developed by TNO DIANA specifically for NAM (more background in Van den Bogert, 2015). The fault is modelled using one layer of interface elements with 2+2 nodes while the rest of the model uses 4-node quadrilateral plane strain elements. These plane strain elements represent linearly elastic material behaviour and do not have an associated failure criterion. This forces failure to occur only on the interface elements, which have a constant and static cohesion and coefficient of friction. Small mesh sizes are found in the fault zone and in the reservoir layers (middle 5 layers). Mesh resolution at reservoir level in the fault and in the rocks adjacent to the fault zone is around 1 m. The mesh size gets coarser towards the boundaries of the model as shown in Figure 11.

3.2.3 Properties and boundary conditions

The lithologies, depths and material properties of the base case scenario are summarized in Table 3. These are similar to the properties used for modelling mechanism 1 to study stress arching (see Table 1). As the FAULT module is used for model generation, the total stress ratio $K_{0,total}$ is used for initialization (as opposed to the effective stress ratio K'_0 in Table 1). A base case scenario is defined with a fault offset of 100 m, a fault strength described by 1 MPa cohesion and a coefficient of friction of 0.6.

Table 3: Summary of material properties of the base case scenario. Depths indicated are formation depths in the footwall. Total stress ratio $K_{0,total}$ is calculated based on a frac gradient of 0.017 MPa for the overburden and Slochteren formation and a frac gradient of 0.018 MPa for the Ten Boer clay and the Carboniferous. Pore pressure gradient is based on a fluid density of 1.153 kg/m^3 and a gas density of 0.1835 kg/m^3 in the Ten Boer clay and Slochteren Sandstone (gas). The high value for the Young's modulus for the Ten Boer clay and the Carboniferous results from the assumption that the rock reacts undrained. The undrained response results in a higher apparent stiffness at the moment of the pressure increase in the faults.

Lithology	**Depth**	**Density**	***E***	***v* (-)**	***$K_{0,total}$* (-)**	***P_p***
Overburden undifferentiated	0 m - 2000 m	2270 kg/m^3	10 GPa	0.25	0.76	Hydrostatic
Zechstein (halite)	2000 m – 2750 m	2150 kg/ m^3	35 GPa	0.30	1.0	Hydrostatic
Zechstein (anhydrite)	2750 m - 2800 m	2970 kg/ m^3	70 GPa	0.25	1.0	Hydrostatic
Ten Boer clay	2800 m - 2850 m	2300 kg/ m^3	40 GPa	0.25	0.82	Initial 35 MPa at top of Ten Boer
Slochteren Sandstone (gas)	2850 m - 2900 m	2300 kg/ m^3	15 GPa	0.20	0.77	Initial 35 MPa at top of Ten Boer
Slochteren Sandstone (water)	2900 m - 3000 m	2300 kg/ m^3	15 GPa	0.20	0.77	Initial 35 MPa at top of Ten Boer
Carboniferous	>3000 m	2300 kg/ m^3	40 GPa	0.25	0.81	Hydrostatic

The normal stiffness of the interface elements is calculated from:

$$D_n = \frac{(1-\nu)E}{(1+\nu)(1-2\nu)h} \tag{9}$$

where E is Young's Modulus, ν is Poisson's ratio and h is thickness of the fault. The shear stiffness of the interface elements is determined using:

$$D_s = \frac{E}{2(1+\nu)h} \tag{10}$$

The values for D_n and D_s were calculated using the properties of the Slochteren Sandstone and h is taken to be equal to 1 m. The left and right side boundaries of the model are assigned the boundary condition of no horizontal displacement while the bottom of the model has the boundary condition of no vertical displacement.

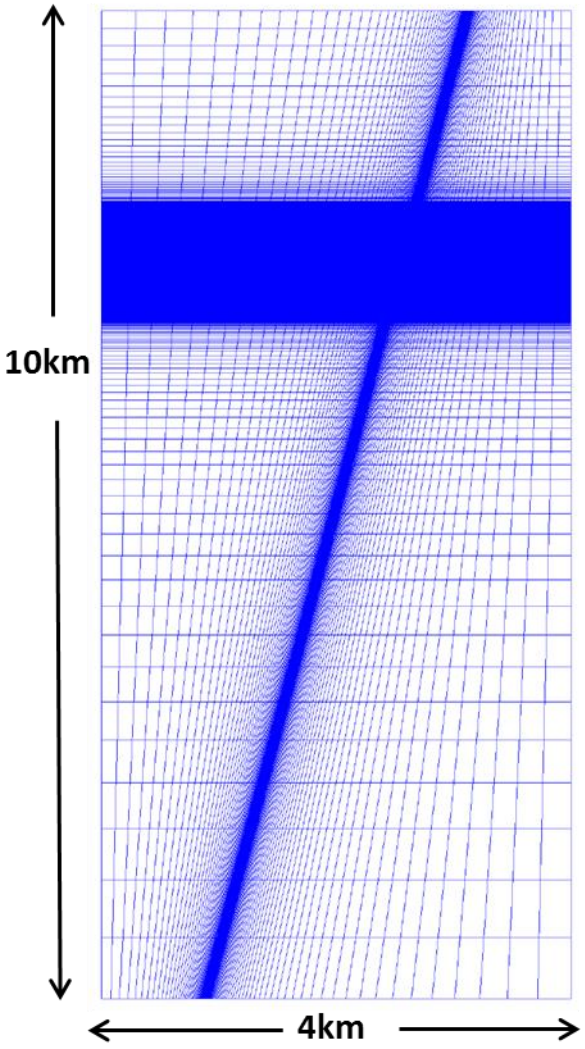

Figure 11: Mesh and geometry: Mesh size is small close to the fault and in the 5 centre layers and gets larger towards the edges of the geometry.

3.2.4 Loading conditions

The model is initialized using the GEOMEC initialization procedure which is part of the FAULT module: Stresses and displacements are calculated based on the weight of the overburden and the $K_{0,total}$ values from Table 3. Displacements during the depletion and injection steps are measured relative to the position of the mesh nodes after initialization (i.e. displacements during initialization are not considered). A depletion of the Ten Boer clay and Slochteren Sandstone by 28 MPa is modelled. Figure 12 presents the pressure changes for the base case scenario at the end of the depletion phase. Pore pressure changes during depletion are imposed on the reservoir elements, the Ten Boer clay elements and the fault elements bounding the reservoir and Ten Boer clay. Pressure diffusion during the injection phase is modelled by a 5 MPa increase of the pore pressure in the Slochteren Sandstone and the adjacent fault elements, as well as the fault elements adjacent to the Ten Boer clay. The pore pressure in the elements covering the Ten Boer clay outside of the fault does not change during the injection phase.

Figure 13 presents the evolution of the pore pressure gradients *within* the fault at the start of depletion and during the depletion and injection phase. Depletion of the Ten Boer clay and Slochteren Sandstone by 28 MPa is modelled in ten equal pressure steps of 2.8 MPa each. Injection by 5 MPa is modelled in ten equal pressure steps of 0.5 MPa. These step sizes are chosen to allow sufficient resolution in the evolution of slip patches and stress path coefficient. Figure 14 presents the evolution of the pore pressure gradients *outside* the fault before depletion and during the depletion and injection phase, for both the hanging wall (left) and footwall block (right).

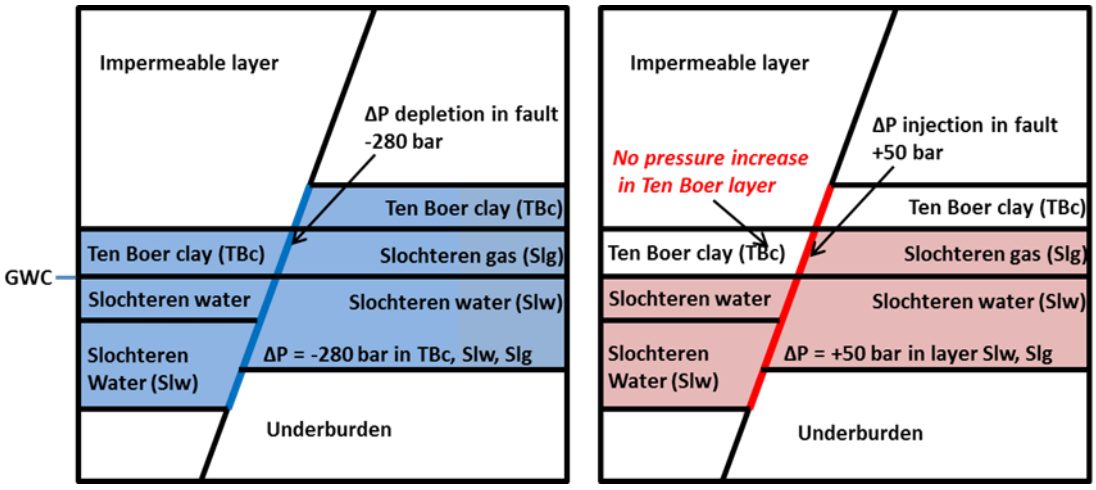

Figure 12: Left: Depletion of the Ten Boer clay, Slochteren Sandstone and fault. Layers and fault segments which are depleted are presented in blue. Right: Injection in the Slochteren Sandstone and fault, including the fault segment bounding the Ten Boer claystone. Layers and fault segments in which a pressure increase occurs are presented in red. Set-up is shown for the 100 m offset base case scenario, layer abbreviations refer to Table 1, and GWC is gas water contact.

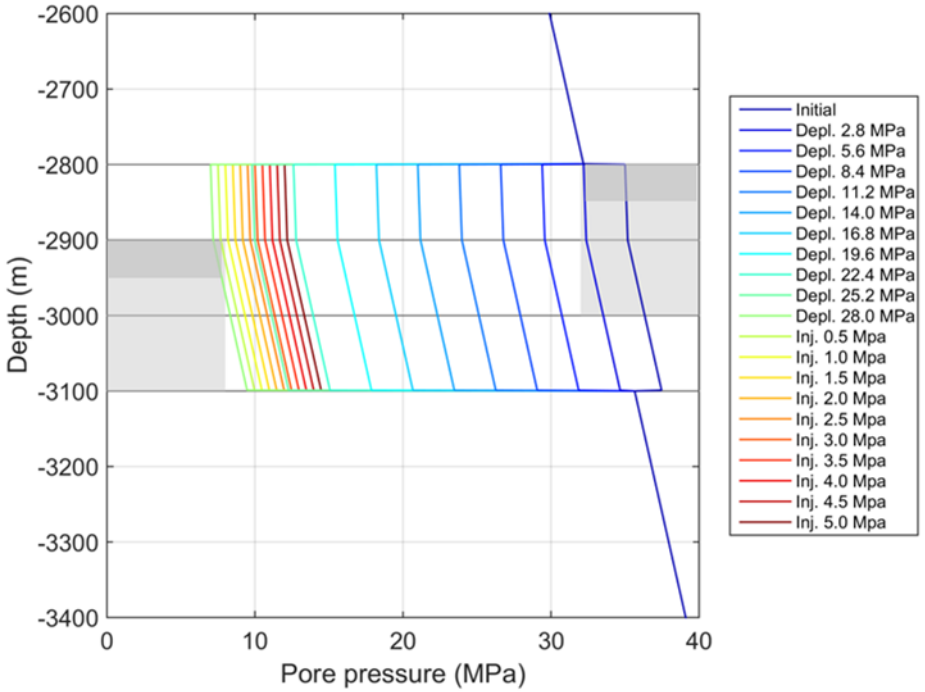

Figure 13: Evolution of pore pressures *within* the fault at the start of depletion and during depletion and injection. Light-grey blocks on the left and right indicate the position of the Slochteren Sandstone reservoir in the hanging wall and footwall, respectively. Dark-grey blocks indicate the position of the Ten Boer claystone in the hanging and footwall block. The change in slope is caused by the difference in density between water and gas. Geometry and pore pressures for the base case scenario of 100 m fault offset.

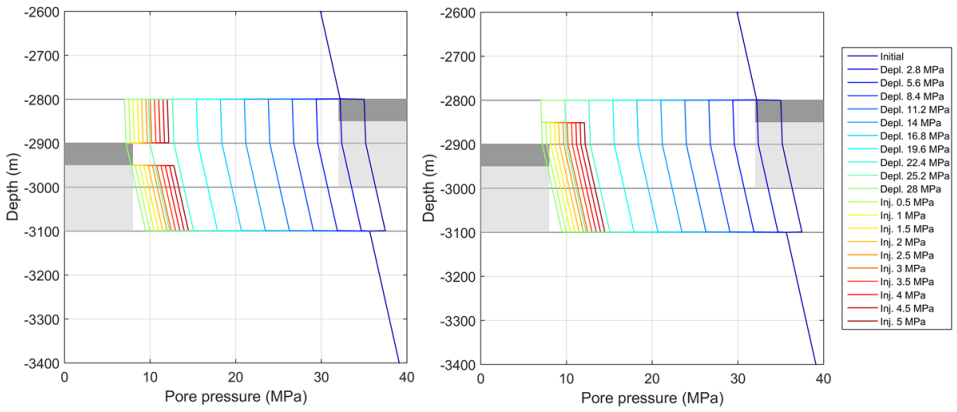

Figure 14: Evolution of pore pressures *outside* the fault at the start of depletion and during depletion and injection, left) hanging wall and right) footwall block. Light-grey blocks on the left and right indicate the position of the Slochteren Sandstone reservoir in the hanging wall and footwall respectively. Dark-grey blocks indicate the position of the Ten Boer claystone in the hanging and footwall block. The change in slope is caused by the difference in density between water and gas. Geometry and pore pressures for the base case scenario of 100 m fault offset.

3.3 Modelling results base case scenario

In this section the results of the base case scenario are presented and discussed. These concern the evolution of stresses, slip lengths and displacements on the faults both during first-time depletion and injection. These results are presented using the shear capacity utilisation (SCU) of the fault, the total slipped length and maximum relative shear displacement as well as the stress paths of several points along the fault introduced in Figure 10. Next to the results found in this paragraph, additional figures with normal stress, shear stress, shear capacity utilisation and shear displacement are found in Appendix B

Figure 15 shows the normal effective stresses, shear stresses, relative shear displacements and the shear capacity utilization (SCU) on the fault for the base case scenario at different stages of the depletion/injection scheme, i.e. at the start of depletion, at the end of depletion and at the end of the injection phase. In the same graph (Figure 15d), the position of the slip patch at the end of depletion (start injection) and at the end of the injection phase is indicated. The slip patch length is defined as the length along the fault where the SCU is equal to 1.

The length of the slip patch and the relative shear displacement along the fault at the point of maximum displacement are shown in Figure 16. The base case shows that no failure occurs during the first 14 MPa of depletion. Failure is initiated once the depletion reaches 16.8 MPa. During depletion, failure along the fault is reached in the region that includes point F35, i.e. at the juxtaposition of the Slochteren Ten Boer (hanging wall) block and the Slochteren Water (footwall) block, and point F45 at the juxtaposition of the Slochteren Water) in both hanging wall and footwall block (Figure 15d). Failure is also reached over a limited section at the juxtaposition of Slochteren Water (hanging wall) and underburden (footwall), just below the footwall reservoir block and at the base of the hanging wall reservoir block (see Figure 15d).The slip patch grows to 117 m and the maximum relative shear displacement reaches 28.2 mm (normal slip) when the depletion reaches 28 MPa (see Figure 16). The stress paths for eight points of interest along the fault are shown in Figure 17.

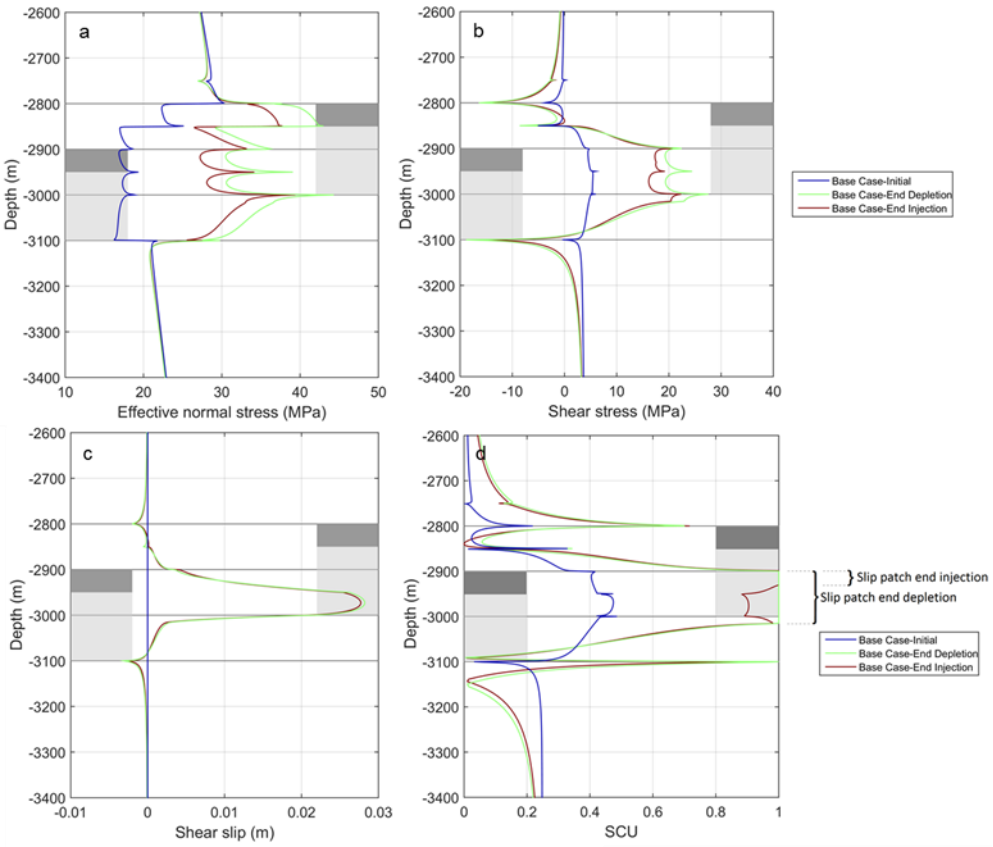

Figure 15: Evolution of stresses and slip during depletion and injection for the base case scenario. a) Effective normal stress, b) shear stress, c) relative shear displacement during the injection phase and d) shear capacity utilization (SCU) of the fault. Base case scenario in which no poro-elastic response of the Ten Boer layer occurs during injection. Light-grey blocks on the left and right indicate the position of the Slochteren Sandstone reservoir in the hanging wall and footwall respectively. Dark-grey blocks indicate the position of the Ten Boer claystone in the hanging and footwall block.

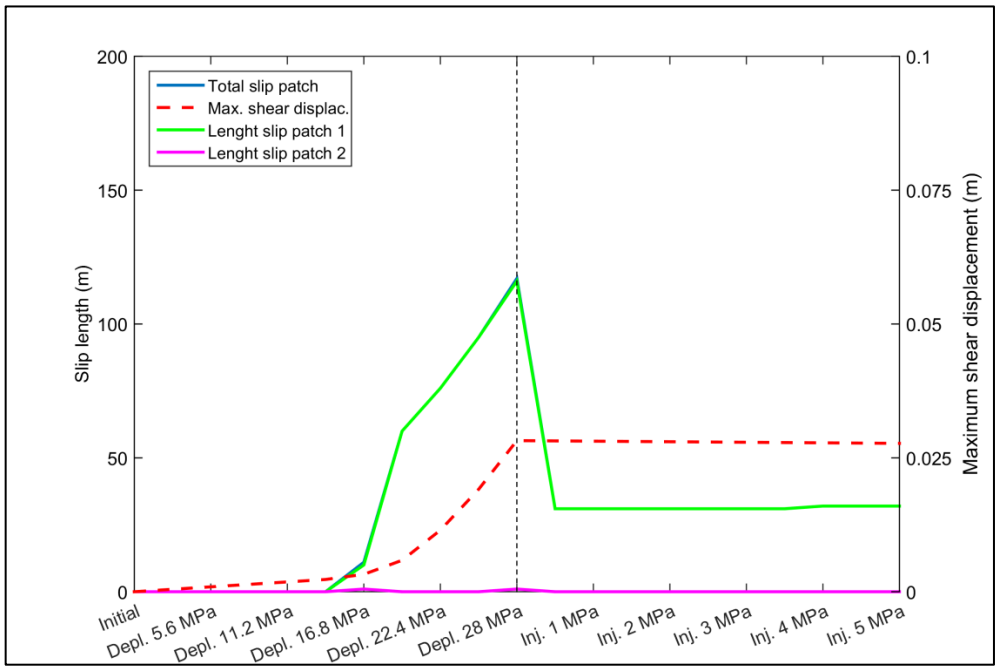

Figure 16: Length of the slip patches and maximum relative shear displacement during depletion and injection period for base case scenario. The black vertical dashed line indicates the transition from depletion to injection. Patch 1 is initiated at a depth of 3000 m, on the transition between Slochteren Sandstone and the Carboniferous in the footwall.

Figure 17 shows that during injection, the stress path of F45 moves away from the failure line – which is confirmed by the evolution of the SCU of the fault segment at the juxtaposition of Slochteren Water and lower fault segments during injection (Figure 15d) and by the decrease in slip length in Figure 16. With the first 0.5 MPa of injection the total length of the slip patch decreases to 31 m. Hence, the fault segments at the juxtaposition of Slochteren Water and lower fault segments, which were at failure during the depletion phase, re-stabilize during injection.

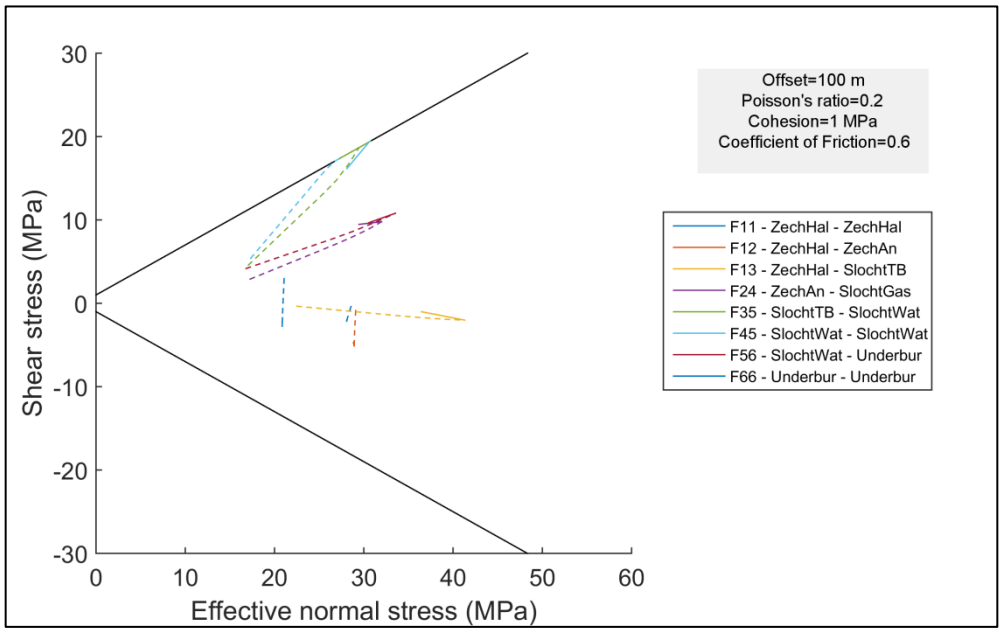

Figure 17: Stress path for points of interest along the fault for the base case scenario. The dashed portion of the stress path represents depletion, the solid part of the stress path represents injection.

In contrast to the stress path of F45, the stress path of F35 does not diverge from the failure line during injection, but lies on top of the failure line during the entire injection period (see Figure 17). At this position the Ten Boer clay and Slochteren Water are juxtaposed. A large part of the fault segment bounding the Ten Boer layer in the hanging wall block remains critically stressed during the entire injection period (see also Figure 15d). Figure 18d shows the changes in shear capacity utilization (dSCU) since the start of injection. A positive change in the shear capacity utilization means the stress conditions on the fault move towards less stable conditions. This figure clearly illustrates stabilizing and destabilizing effects of injection. Figure 18d shows that the main (upper) part of the fault segment at the juxtapostion of Ten Boer layer and Slochteren Water does not stabilize during injection (dSCU=0).

Although parts of the fault remain critically stressed during injection, the changes in the maximum relative shear displacement during injection are very small (Figure 15c and Figure 18c). A small decrease in maximum relative shear displacements is observed (see Figure 16 and Figure 18c). During injection, additional relative shear displacements along the fault do not exceed 0.8 mm, and act in a direction opposite to the direction of relative shear displacements during depletion.

Juxtaposition of the Ten Boer clay also occurs at the fault segment represented by the stress path of F13. At this depth, the Ten Boer clay layer is juxtaposed against Zechstein rock salt. Initial shear stresses on the fault segment are very low, due the isotropic initial stress conditions in the Zechstein rock salt. The effect of pore pressure diffusion in the fault (and the absence of a poro-elastic rebound in the Ten Boer clay) on fault stability is very small, and shear capacity utilization on the fault during both depletion and injection remains far from critical.

The base case scenario is defined by a normal fault of 75º dip with an offset of 100 m. As shown in earlier publications by Roest (1994), Mulders (2003), Orlic (2013) and Van den Bogert (2015), fault offsets are of paramount importance for the evolution of fault stresses during reservoir depletion and re-pressurization. This means that, in addition to the poro-elastic response of the Slochteren Sandstone and Ten Boer clay and the pore pressures in the faults and pressure differences over the fault, other factors like stiffness contrasts between juxtaposed lithologies and differential compaction will control the stress paths during depletion and injection.

The specific geometry of the base case strongly contributes to the failure during depletion. For a uniformly depleted, horizontally layered, Slochteren Sandstone reservoir with no fault offset, the stress path coefficients (γ_h=0.75, γ'_h=0.25) for the base case parameters (fault dip 75º, v=0.2 and a fault friction coefficient of 0.6) would produce no significant change in the shear capacity utilization of the fault. For uniform depletion of the Ten Boer clay and no fault offset, the stress path coefficients (γ_h=0.57, γ'_h =0.43, v=0.3) for the base case parameters would even result in a lowering of the SCU. The failure observed during depletion in the base case scenario can be explained by the occurrence of differential compaction due to the existence of pressure differences between depleting and non-depleting formations, stiffness contrasts (Ten Boer clay, Slochteren Sandstone and underburden) and the offset between footwall and hanging wall reservoir blocks (see also Mulders, 2003 and Van den Bogert, 2015).

In a similar way, the geometry of the base case and fault offset have a large impact on the evolution of fault stresses during the injection phase. At the juxtaposition of Slochteren Water in both footwall and hanging wall block, the fault segments restabilize during the injection phase. At this location, the decompaction of the reservoir on both sides of the fault caused by injection results in a differential movement along the fault plane and causes a negative incremental shear stress which acts in opposite direction as during depletion, reducing the total shear stress along the fault. This re-stabilization is not observed at position F35, where the Ten Boer clay in the hanging wall block is juxtaposed against the Slochteren Sandstone (water) in the footwall block. At this position, negative incremental shear stresses develop during injection (Figure 15c and Figure 18c), reducing the total amount of shear stress on this fault segment. However, at the same time, the normal effective stresses on this part of the fault also decrease, due to the increase in pore pressures (Figure 15a and Figure 18a). Normal effective stresses on the fault segment at the juxtaposition of the Ten Boer clay and the Slochteren Water decrease faster than at the juxtaposition of the Slochteren Water, whereas the (negative) incremental shear stresses are less than at the juxtaposition of the Slochteren Water. This explains the higher SCU of the fault segment at the juxtaposition of the Ten Boer clay and the Slochteren Water. The differences in the changes in effective normal stresses and shear stresses can be explained by the absence of the poro-elastic rebound (and decompaction) of the Ten Boer claystone.

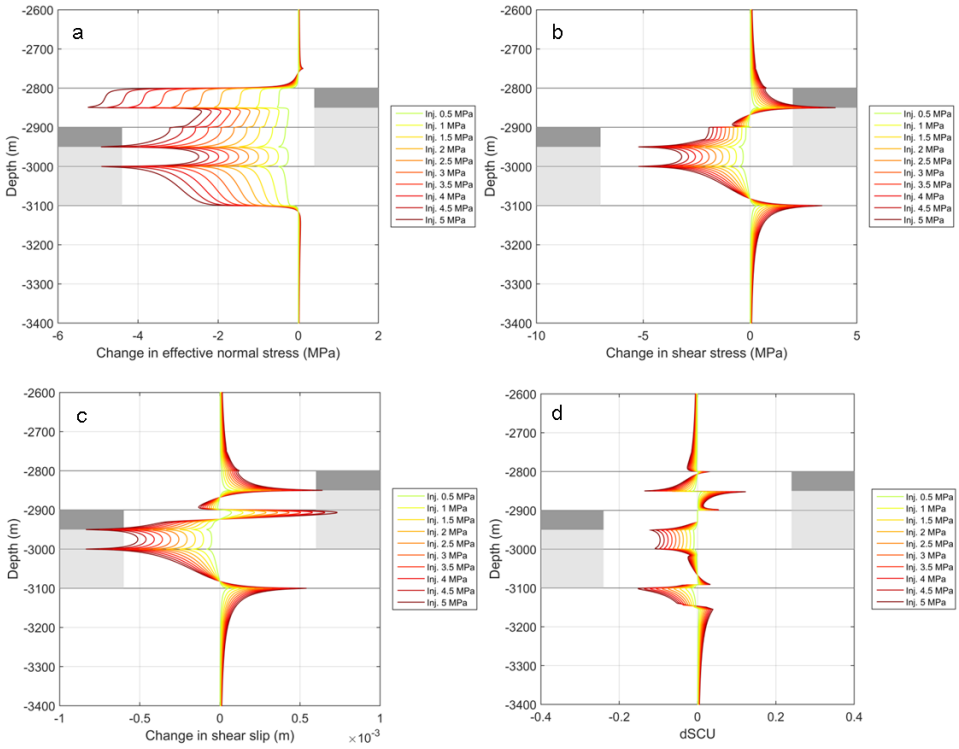

Figure 18: C*hanges* in a) effective normal stress, b) shear stress, c) shear capacity utilization (dSCU) of the fault and d) fault slip during the injection phase. Base case scenario in which no poro-elastic response of the Ten Boer layer occurs during injection.

As shown above, in the base case scenario fault reactivation during depletion and injection results from the complex interplay of many factors, one of the components being pressure diffusion. In order to 'isolate' the effect of pore pressure diffusion on fault reactivation during injection, a variation of the base case is modelled. In this variation of the base case, during injection, the pore pressure increases in the entire Ten Boer layer. Figure 19 shows the SCU at the end of depletion and injection and the change in shear capacity utilization when a poro-elastic response of the Ten Boer layer is modelled (i.e. when a pressure increase in the Ten Boer layer during injection is modelled). In this case, the entire fault section at the juxtaposition of Ten Boer layer and Slochteren Water would stabilize during injection. Hence, the locally high pore pressures in the fault segment bounded by the Ten Boer as compared to the Ten Boer rocks, which occur during injection due to differences in the diffusivities of the fault and low permeability rocks, have an adverse effect on fault stability.

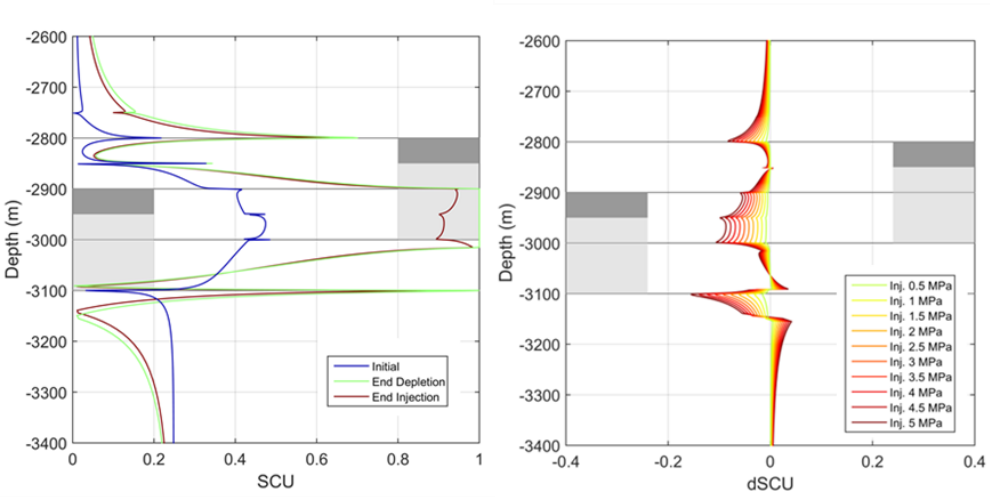

Figure 19: Variation on the base case in which a poro-elastic response occurs in the Ten Boer (i.e. injection results in a pressure increase in the Ten Boer layer). Left: Shear capacity utilization at start depletion, end depletion and end injection. Right: *Change* in shear capacity utilization (dSCU) during injection. The light-grey blocks on the left and right indicate the position of the reservoir (Slochteren Gas and Water) in the hanging wall and footwall respectively. The dark-grey blocks indicate the position of the low-permeability Ten Boer layer.

3.4 Sensitivities

In addition to the base case scenario, sensitivities for reservoir material properties and fault material properties are analysed using the range of properties given in Table 4. These reservoir material properties are only changed within the Slochteren Sandstone formation (both water and gas), whereas fault properties are changed along the entire length of the fault.

Table 4: Model parameters used for sensitivity study.

Sensitivity	**Values**	**Basecase**
Cohesion and friction coefficient of fault	Cohesion: 1, 2, 3 MPa μ: 0.5, 0.6, 0.7	Cohesion: 1 MPa μ: 0.6
Poisson's ratio	0.10, 0.20, 0.30	0.20
Offset	0, 100, 200 m	100 m
Amount of slip during depletion	Slip during depletion No slip during depletion	Slip during depletion (100 m offset case)
Pressure during depletion and injection	Depletion: Down to 2.0 MPa Injection: Up to 12.0 MPa	Depletion: Down to 7.0 MPa Injection: Up to 12.0 MPa

3.4.1 Cohesion and coefficient of friction of the fault

Four DIANA runs are performed to assess the sensitivity to fault cohesion and the sensitivity to the coefficient of friction along the fault. The mesh geometry and the imposed pore pressure changes are identical to the base case.

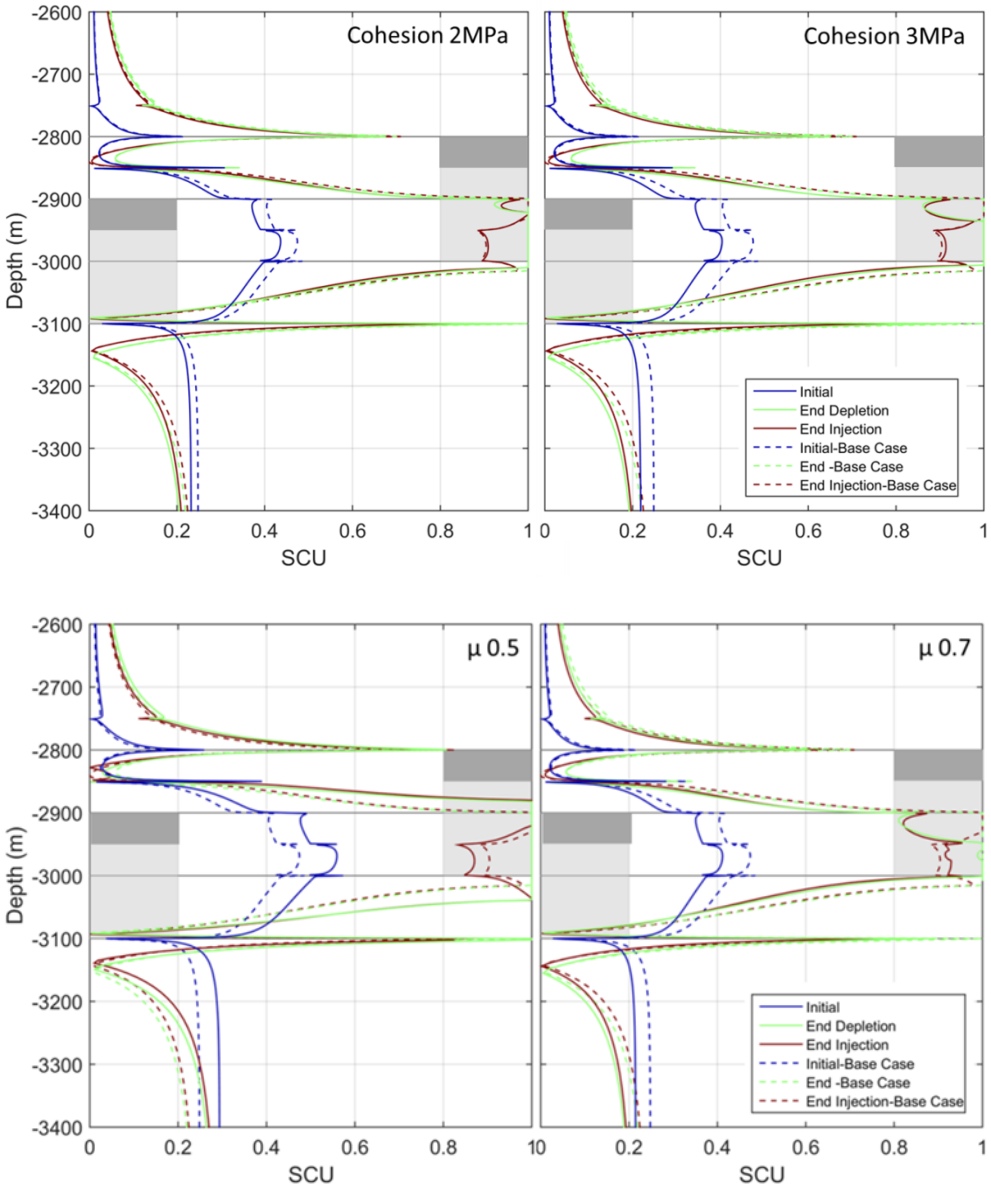

Figure 20: Overview of shear capacity utilization (SCU) for different fault cohesion (first row) and fault friction coefficient (bottom row). Dashed lines represent SCU for the base case. Solid lines represent SCU for the different sensitivity scenarios. The light-grey blocks on the left and right indicate the position of the reservoir (Slochteren Gas and Water) in the hanging wall and footwall respectively. The dark-grey blocks indicate the position of the low-permeability Ten Boer layer.

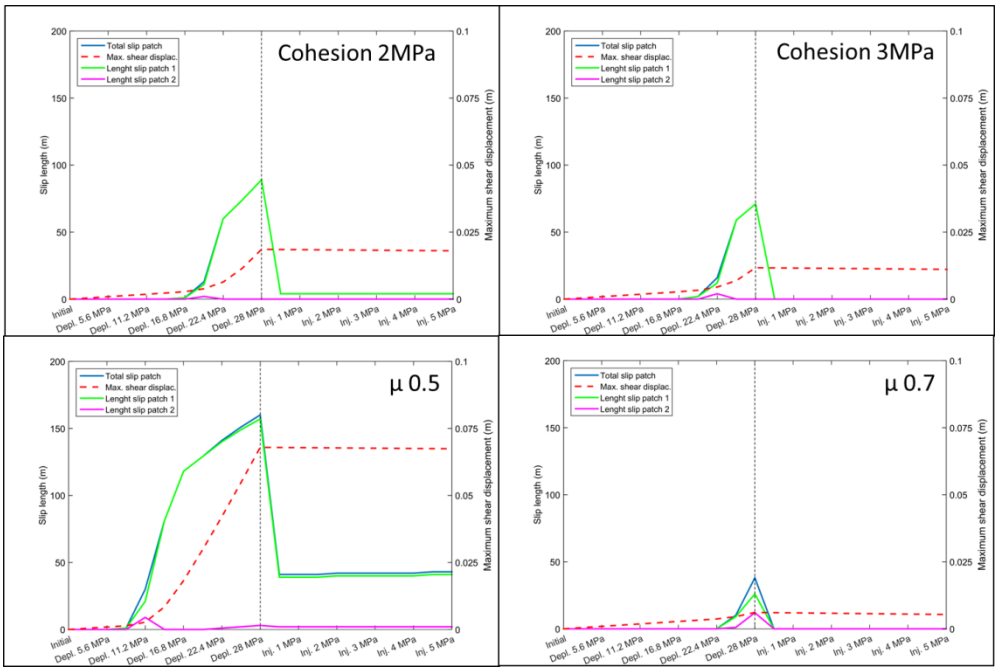

Figure 21: Evolution of slip length and maximum relative shear displacement for different fault cohesion (first row) and fault friction coefficient (bottom row).

The results from Figure 20 and Figure 21 show that for higher cohesion of 2 MPa and 3 MPa and for a friction coefficient μ of 0.7, initial shear capacity utilization is lower than for the base case and the onset of fault slip occurs at a later depletion stage, i.e. at lower reservoir pressures. At higher cohesion and fault friction coefficient, less shear displacement occurs on the faults and slip lengths are shorter than for the base case (see Figure 21 and also Table 5 for an overview of slip lengths and shear displacements). For a friction coefficient μ of 0.5, the onset of slip occurs at higher reservoir pressures than for the base case and slip length and relative shear displacement are larger. Stress paths and changes in shear capacity utilization for the individual sensitivities are presented in Figure B 5 to Figure B 17.

For a cohesion of 2 MPa, the main part of the fault which is critically stressed during depletion, stabilizes during the injection phase (Figure 20). At the end of the depletion phase the average shear capacity utilization of the fault at the juxtaposition of Ten Boer clay and Slochteren Water is smaller than for the base case, and only the lower part of the fault segment is critically stressed. During injection, the lower part of the fault segment at the juxtaposition of Ten Boer clay and Slochteren Water partially stabilizes. The upper part of the fault segment shows a small increase in shear capacity utilization during injection, but the failure criterion is not reached. Only a very limited section of the fault bounding the Ten Boer in the hanging wall block is still critically stressed at the end of injection. The same trend in evolution of fault stresses is observed for the 3 MPa cohesion scenario. For this sensitivity, however at the end of the injection phase all fault segments have stresses below the failure criterion.

For a friction coefficient μ of 0.5 during depletion a larger fault segment reaches the failure criterion than for the base case. A significant part of the fault stabilizes during

injection. The upper part of the fault segment at the juxtaposition of Ten Boer clay and Slochteren Water remains critically stressed at the end of the injection phase. For a friction coefficient of 0.7, the entire fault stabilizes during the injection phase.

It is noted here that although in case of the cohesion of 2 MPa and friction coefficient μ of 0.5 the fault section bounding the Ten Boer in the hanging wallblock remains partially critically stressed, the maximum relative shear displacement during injection is very small (i.e. almost equal to the elastic rebound of the 3 MPa cohesion and friction coefficient μ=0.7 scenario). In all cases, the total length of the slip patch decreases during the injection phase.

3.4.2 Poisson's ratio of the reservoir

Two DIANA runs are performed to assess the sensitivity to Poisson's ratio of the reservoir. The mesh geometry and the imposed pore pressure changes are identical to the base case.

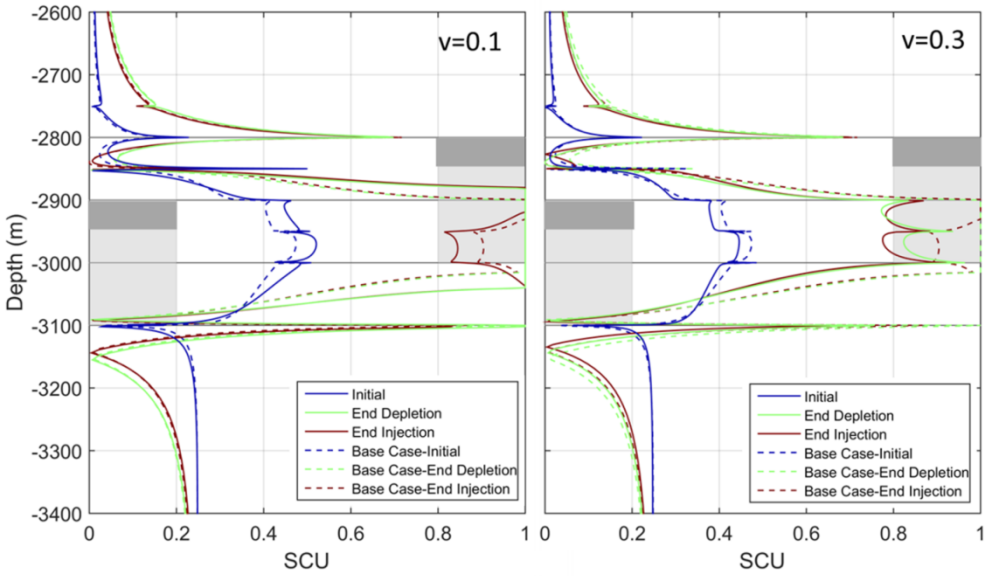

Figure 22: Overview of shear capacity utilization (SCU) for different Poisson's ratio values of the reservoir rocks. Dashed lines represent SCU for the base case. Solid lines represent SCU for the different sensitivity scenarios. The light-grey blocks on the left and right indicate the position of the reservoir (Slochteren Gas and Water) in the hanging wall and footwall respectively. The dark-grey blocks indicate the position of the low-permeability Ten Boer layer.

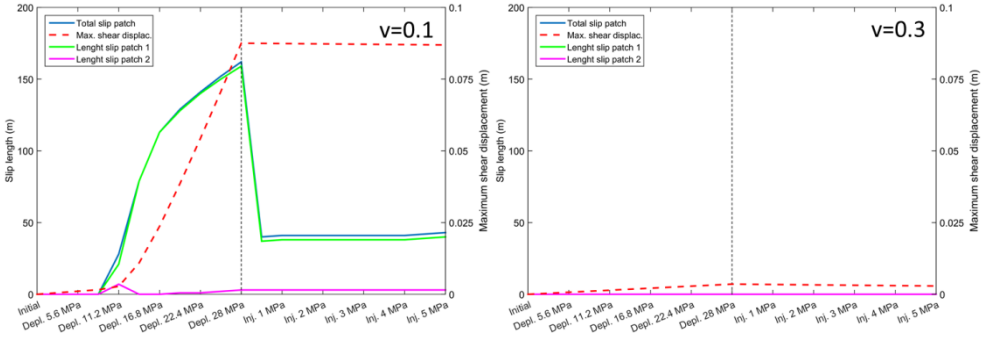

Figure 23: Evolution of slip length and maximum relative shear displacement for different Poisson's ratio values for the reservoir rocks.

Figure B 18 and Figure B 21 show that the Poisson's ratio value for the reservoir determines the slope of the stress path (Van den Bogert, 2015). A lower Poisson's ratio *v* of 0.1 leads to steeper stress paths which has a destabilizing effect on the fault. The length of the fault segment, that slips during depletion in the scenario of *v*=0.1, is significantly larger than for the base case scenario. A large part of the fault section that slips during depletion, stabilizes during injection. However, the upper part of the fault segment between a depth of 2880 m and 3025 m, which comprises part of the fault section bounding the Ten Boer layer in the hanging wall block, remains critically stressed during injection. The total length of the slip patch decreases during the injection phase. The maximum relative shear displacement along the fault during injection is very small, i.e. 1.0 mm.

A higher Poisson's ratio leads to a lower stress path gradient which has a stabilizing effect on the fault. No fault slip occurs in the scenario of *v*=0.3, neither during depletion nor injection.

3.4.3 No slip during depletion and increased depletion

The base case model involves fault slip during depletion of the reservoir. To investigate the influence of the amount of slip during depletion on the amount of slip during injection, two scenarios are modelled; one scenario that does not slip at all during depletion, and another scenario that involves more slip during depletion than the base case scenario.

The condition of no slip during depletion is modelled by changing the imposed pore pressure during the depletion phase in such a way that the most critical point on the fault gets to the verge of failure, but does not actually exceed the failure criterion. To do so, the total depletion is set to 13.72 MPa in ten equal steps. The subsequent injection scheme is unchanged and remains at 5.0 MPa in ten equal steps. The changed pore pressure depletion/injection scheme is shown in Figure B 25. The mesh geometry and the material properties are identical to the base case.

Figure 24 (left) presents the shear capacity utilization for depletion and injection for the scenario of no fault reactivation during depletion, compared to the shear capacity utilization for the base case scenario, where fault reactivation does occur

during depletion (base case depletion is 28 MPa in ten equal steps). For the major part of the fault, shear capacity utilization decreases during the injection phase, except for the upper part of the fault segment at the juxtaposition of the Ten Boer layer and the Slochteren Water and the fault segment above, which shows an increase in shear capacity utilization between 2850 m and 2925 m depth. Stress paths and changes in shear capacity utilization for this scenario are presented in Figure B 26 to Figure B 28. In this particular depletion/injection scheme, stresses on the fault (75º fault dip) do not reach the failure criterion and no fault slip is observed. In case of the increased depletion scenario, the pore pressure change during depletion is set to 33.0 MPa in ten equal steps. The subsequent injection scheme is changed to 10.0 MPa in ten equal steps to arrive at a final pore pressure profile that is identical to the final pore pressure profile in the base case. The changed pore pressure depletion/injection scheme is shown in Figure B 30. Again, the mesh geometry and the material properties are identical to the base case.

Figure 24 (right) presents the shear capacity utilization for depletion and injection for the scenario of increased depletion. Due to the different load step sizes, there are no steps in the model which can be directly compared to the base case scenario. However, when comparing loads steps which are close (e.g. 19.8 MPa depletion vs 19.6 MPa depletion), the results are very similar. Additionally, the onset of failure is at a reservoir pressure comparable to that of the base case, with a stable fault at 13.2 MPa of depletion and a slipping fault at 15.5 MPa of depletion. This implies that the load step size does not significantly influence the results. At 33 MPa depletion, the slip patch length is 129 m and the maximum relative shear displacement is 45.9 mm.

The slip length at the end of depletion includes the juxtaposition of Ten Boer layer in the hanging wall block and Slochteren Water in the footwall block, as well as the fault section bounded on both sides by Slochteren Water and the fault section directly below the footwall reservoir block. A significant decrease in shear capacity utilization during injection occurs at the fault segments where Slochteren Water is juxtaposed on both sides of the fault and at deeper fault segments. Shear capacity utilization at the lower part of the fault section bounding the Ten Boer layer in the hanging wall block also decreases, whereas stresses on the upper part of this fault section remain critical.

Stress paths and changes in shear capacity utilization for the scenario of increased depletion are presented in Figure B 31 to Figure B 34

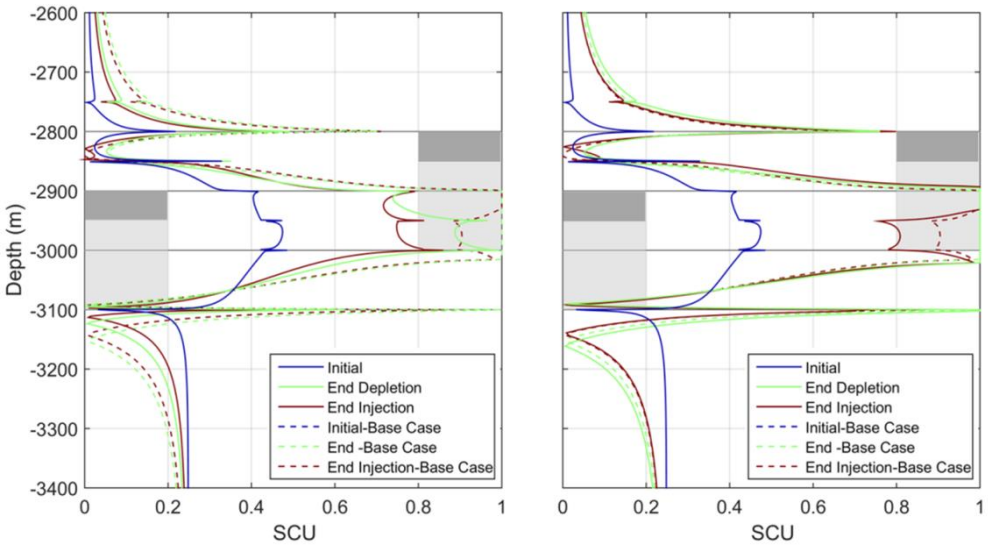

Figure 24: Shear capacity utilization (SCU): Left: SCU for the scenario without slip during depletion. Right: SCU for the scenario with increased depletion. Dashed lines represent SCU for the base case. Solid lines represent SCU for the scenario of no slip during depletion (left) and increased depletion (right). The light-grey blocks on the left and right indicate the position of the reservoir (Slochteren Gas and Water) in the hanging wall and footwall respectively. The dark-grey blocks indicate the position of the low-permeability Ten Boer layer.

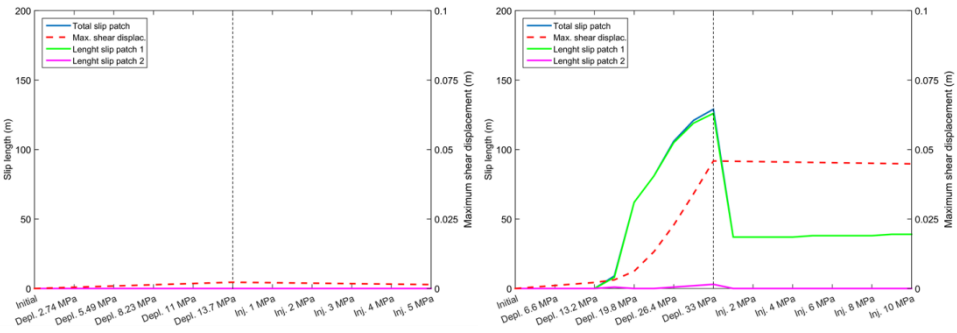

Figure 25: Evolution of slip length and maximum relative shear displacement for the condition of no slip during depletion (left graph) and increased depletion (right graph).

3.4.4 Different offset along fault

Two DIANA runs are performed with different meshed geometries to investigate the effect of a different offset. One case has an offset of 0 m (Figure 26) and the other case has an offset of 200 m (Figure 27). The imposed pore pressure change with depth is changed to represent the presence of reservoir formations at different depths (see Figure 28) for the pore pressure profiles within the fault and in hanging and footwall block).

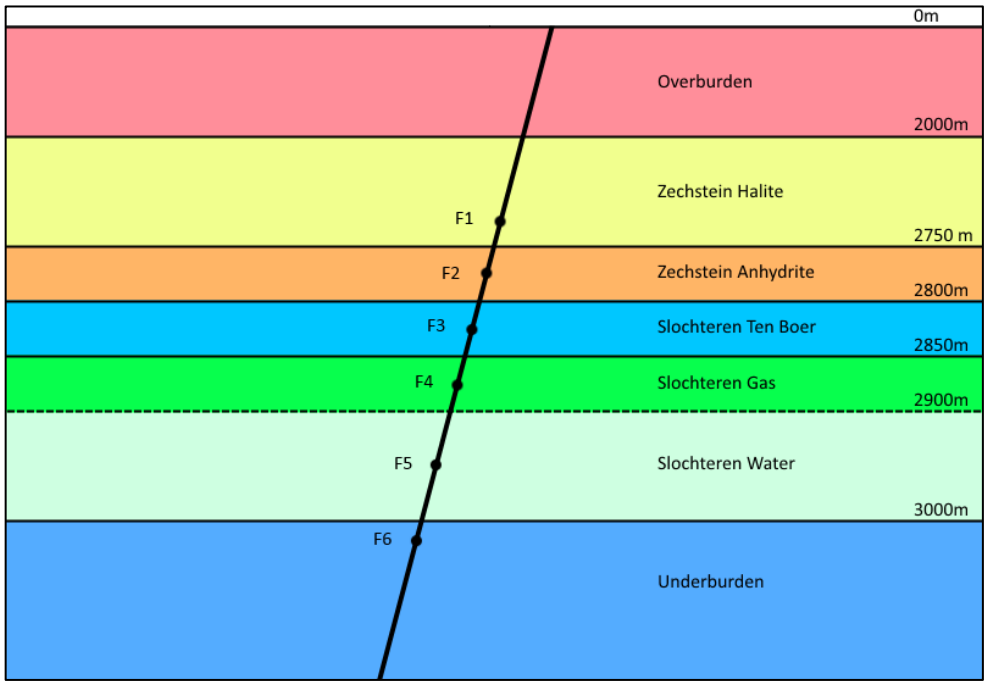

Figure 26: Schematic geometry for 0 m offset case (not to scale). Points F2 to F5 are chosen in the centre of their respective formation. Points F1 and F6 are chosen 25 m away from the neighbouring formation.

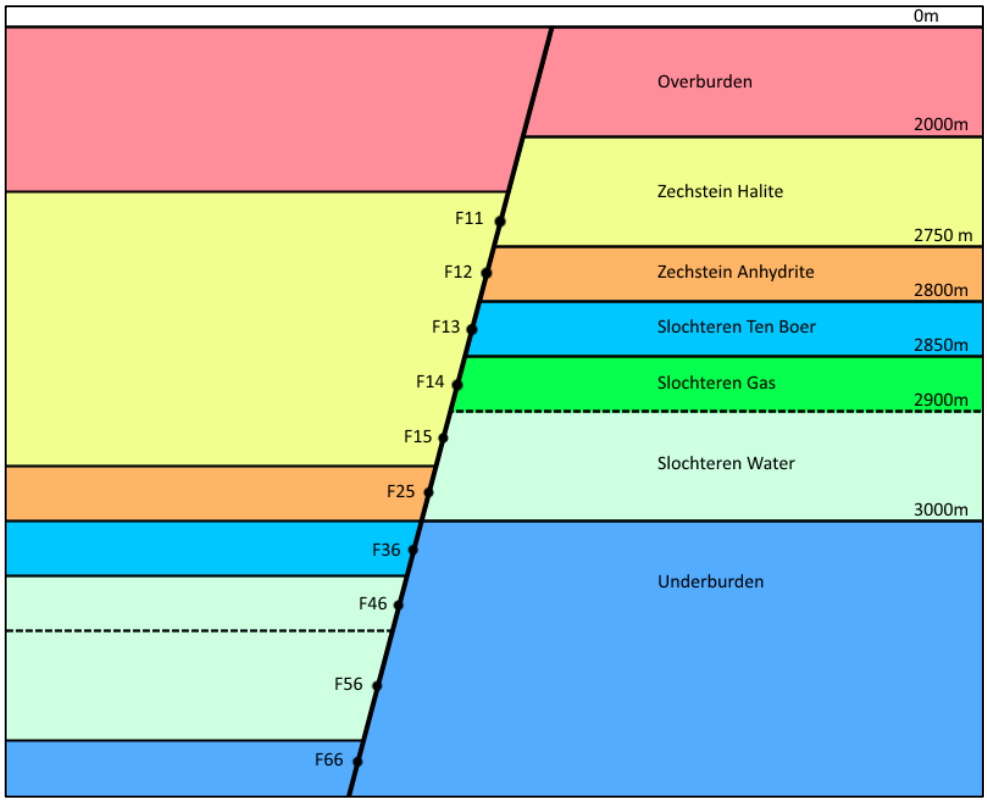

Figure 27: Schematic geometry for 200 m offset case (not to scale). Points F11 to F56 are chosen in the centre of their respective formation contact. Point F66 is chosen 25 m away from the formation boundary above.

The material properties are identical to the base case. For the 200 m offset case, failure is not reached at any of the predefined points. However, failure does occur just below point F25 and between F56 and F66. The point of maximum slip occurs at a depth of 3000 m (at the bottom of the Slochteren reservoir block in the footwall block) and is plotted as an extra stress path (labelled “Max Slip” in Figure B 38).

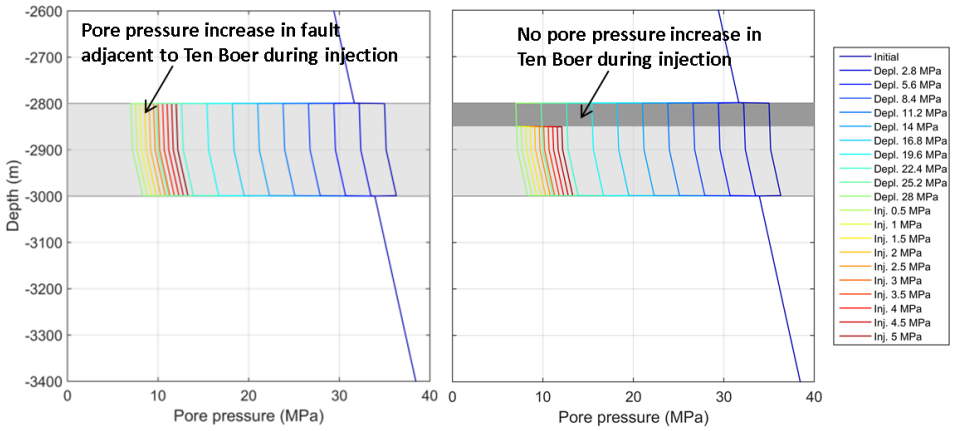

Figure 28: Overview of different pore pressure profiles for the 0 m offset scenario. Left: *within* the fault, right: Hanging- and footwall block.

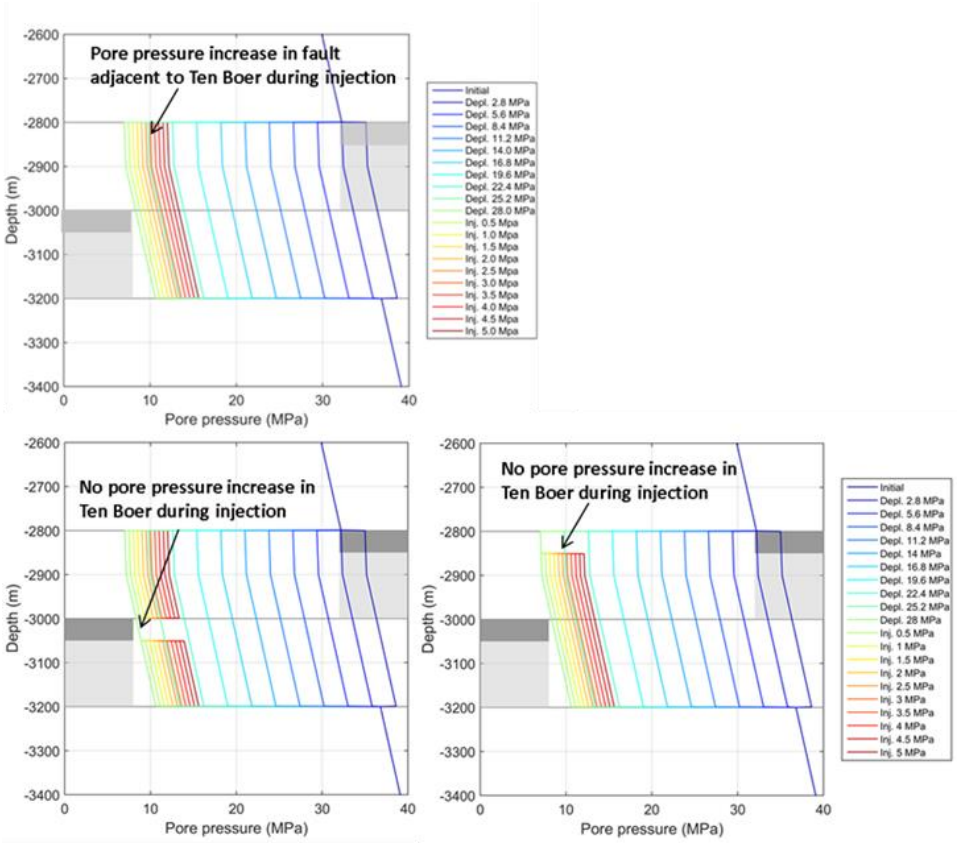

Figure 29: Overview of different pore pressure profiles within the fault for the 200 m offset scenario. Upper plot: *Within* the fault. Lower left plot: Hanging wall block and lower right plot: Footwall block.

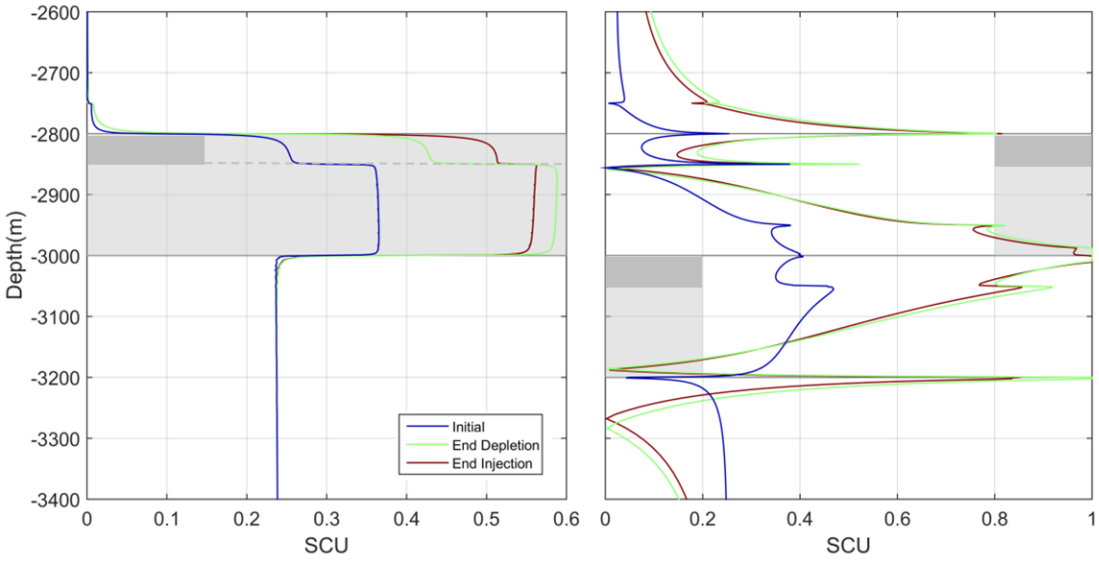

Figure 30: Shear capacity utilization SCU): Solid lines represent SCU for the scenario of 0 m offset (left) and 200 m offset (right). The light-grey blocks on the left and right indicate the position of the reservoir (Slochteren Gas and Water) in the hanging wall and footwall respectively. The dark-grey blocks indicate the position of the low-permeability Ten Boer layer.

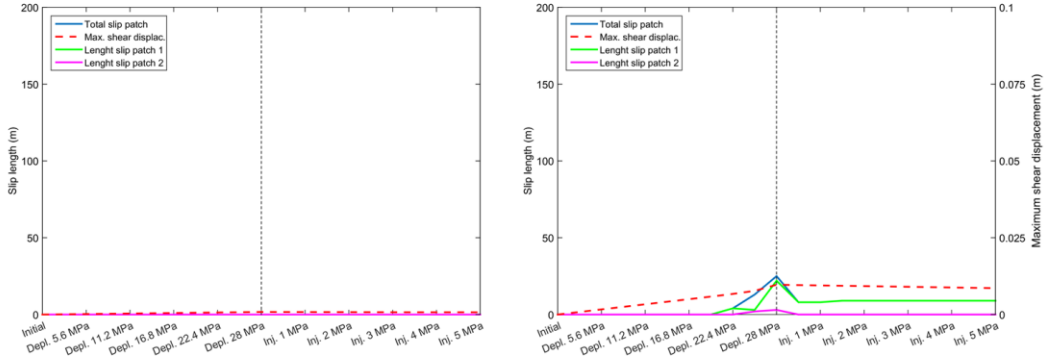

Figure 31: Evolution of slip length and maximum relative shear displacement for the 0 m offset (left graph) and 200 m offset (right graph) scenario.

The zero fault offset case does not reach failure during either depletion or injection, while the 200 m offset case results in significantly less relative shear displacement and smaller slip patches than the base case.

For the 0 m offset case, the fault stresses on the fault segment bounding the Slochteren Gas and Water move towards more stable conditions, whereas the stresses on the fault segment bounding the Ten Boer layer become more critical. In this scenario part of the fault is bounded on both sides by the Ten Boer layer. For this fault segment entirely embedded within the Ten Boer, no poro-elastic effects occur in the bounding rocks during injection. Figure 30 (left) shows the effect of the direct pore pressure increase in the fault and the simultaneous absence of the poro-elastic effect in the surrounding rocks. The shear capacity utilization for the fault

segment embedded in the Ten Boer increases, whereas shear capacity utilization of the fault segments in the deeper Slochteren Gas and Water decreases. The increase in the shear capacity utilization of the faults embedded in the Ten Boer is significant, i.e. SCU increases by 0.1.

For the 200 m offset scenario, again two fault segments exist which are bounded by the impermeable Ten Boer. Similar to the base case scenario of 100 m offset the upper fault segment is positioned next to the Ten Boer in the footwall block and the Zechstein Halite in the hanging wall block. Due to the very low initial shear capacity utilization, stress changes on this fault segment during depletion and injection do not result in failure. The lower fault segment is bounded by the Ten Boer and Carboniferous underburden. As no pore pressure increase for the injection phase is modelled for both the Ten Boer and underburden, the lower fault segment is only affected by the direct pore pressure increase due to pressure diffusion into the fault. This fault segment bounding the Ten Boer layer becomes critically stressed during depletion and stays critically stressed during injection. Again, relative shear displacements along this fault segment during injection are very small (cf. Table 5). For the 200 m offset case, a small segment of the fault around a depth of 3000 m, which is bounding the Ten Boer layer, remains critically stressed during injection. The total slip length decreases during injection, as compared to the end of depletion. Maximum relative shear displacement along the fault for the 200 m offset case during injection is small, i.e. 1.1 mm.

3.5 Discussion & conclusions

The base case scenario with 100 m fault offset shows that the shear capacity utilization of a large part of the fault decreases during the injection phase, which means that for these fault segments injection has a stabilizing effect. However, simultaneously the scenario also shows that due to the differential pore pressures, which develop due to different diffusivities of the Ten Boer clay layer and the fault, fault segments locally remain critically stressed during the injection phase. For comparison, in a scenario where pore pressures in the Ten Boer clay are allowed to increase as much as in the reservoir and faults (i.e. no difference in the diffusivities for the faults and the Ten Boer clay is assumed and a full poro-elastic response of the Ten Boer clay is taken into account during the injection phase), the entire fault stabilizes during injection. Hence it is concluded that the higher pore pressures which develop in the faults adjacent to the Ten Boer clay compared to the Ten Boer clay rocks and the absence of a poro-elastic response in the Ten Boer rocks locally have an adverse effect on the stability of the fault. Base case results show that even though locally the faults remain critically stressed due to the effect of pressure diffusion, during the injection phase the total length of the slip patch decreases and additional fault slip is limited to 0.8 mm.

A similar result is obtained for the scenario of 200 m offset. Again, in this scenario the shear capacity utilization of a large part of the fault decreases during the injection phase, which means that for these fault segments injection has a stabilizing effect and the total slip length during the injection phase decreases as compared to the end of depletion. Similar to the base case, due to the increase in pore pressures caused by pressure diffusion into the lower fault segment bounded by the Ten Boer layer, this fault segments locally remains critically stressed during

injection. The additional relative shear displacements along this fault segment during injection is limited, i.e. 1.1 mm (see Table 5).

The effect of pore pressure diffusion and the differential pressures in the Ten Boer clay and Ten Boer faults on fault stresses is even more pronounced in the case of the 0 m offset scenario. In the 0 m offset scenario part of the fault is bounded on both sides by the Ten Boer layer. For this fault segment entirely embedded within the Ten Boer layer, during injection no poro-elastic effects occur in the bounding rocks. The direct pore pressure increase in the fault and the simultaneous absence of the poro-elastic effect in the surrounding rocks translates into an increasing shear capacity utilization for the fault segment embedded in the Ten Boer layer. Fault segments in the deeper Slochteren Gas and Water, which are affected by the poro-elastic response of the surrounding rocks show a decreasing SCU. The increase in the shear capacity utilization of the faults embedded in the Ten Boer layer is significant, and though in this specific case (75º fault dip) failure is not reached, faults which are more critically oriented may be reactivated during injection. The latter would present a scenario where fault reactivation and slip is *initiated* during the injection phase.

Sensitivities other than for variation in fault offset, show that the length of the fault segment which remains critically stressed during the injection phase, decreases with increasing strength of the fault. For a very strong fault (cohesion 3 MPa and friction coefficient μ=0.7), the entire fault stabilizes during the injection phase (including the fault segments bounded by the Ten Boer layer). The length of the fault segment, which is critically stressed at the end of injection, increases for a fault of lower fault strength (μ=0.5), a steeper stress path (v=0.1) and for an increase in depletion.

For all scenarios, the lengths of the fault segment which is critically stressed at the end of injection and the maximum relative shear displacements during injection are summarized in Table 5. Comparison of slip lengths and maximum relative shear displacements during injection and depletion shows that in all modelled scenarios, fault movements which occur during the injection phase are very small compared to the fault movements during the depletion phase. Moreover, for all the scenarios with faults critically stressed during the depletion phase, the total slip lengths decrease during the injection phase.

Table 5: Overview of maximum slip lengths and maximum relative shear displacements (rsd) along the fault during depletion and injection.

Scenario	**Maximum rsd depletion**	**Maximum rsd injection**	**Maximum slip length during depletion**	**Maximum slip length during injection**
Base case	28.2 mm	0.8 mm	117 m	32 m
Cohesion 2 MPa	18.6 mm	0.8 mm	89 m	4 m
Cohesion 3 MPa	11.7 mm	0.8 mm	71 m	0 m
Friction coefficient 0.5	67.9 mm	0.8 mm	160 m	43 m
Friction coefficient 0.7	6.1 mm	0.8 mm	38 m	0 m
Poisson's ratio 0.1	87.5 mm	1.0 mm	162 m	43 m
Poisson's ratio 0.3	3.5 mm	0.6 mm	0 m	0 m
No slip during depletion	2.2 mm	0.8 mm	0 m	0 m
Increased depletion	45.9 mm	2.1 mm	129 m	39 m
Offset 0 m	0.8 mm	0.1 mm	0 m	0 m
Offset 200 m	9.7 mm	1.1 mm	25 m	9 m

In summary, model results show that due to an increase in pore pressures in the faults bounding the Ten Boer layers and a delayed response in the pore pressure increase in the Ten Boer clay in the hanging wall and footwall block:

- During injection into a reservoir with faults already critically stressed during depletion, faults bounding the Ten Boer clay locally remain critically stressed.
- During injection into a reservoir with faults already critically stressed during depletion, total slip lengths decrease during the injection phase. Additional relative shear displacement during the injection phase are very small with a maximum of 2.1 mm.
- In case of the 0 m offset scenario and the scenario of no slip during depletion, no fault slip occurs during either depletion or injection. However, the shear capacity utilization of the faults bounding the Ten Boer clay increases during the injection phase. This indicates fault slip on more critically oriented faults than modelled can potentially be initiated during the injection phase. This scenario has not been analyzed in this study.

4 Mechanism 3: Irreversible stress paths during production and injection

4.1 Description of mechanism

Analysis by Santarelli et al. (1998) of stress paths during depletion and re-pressurization of a number of reservoirs indicates that stress path coefficients can be much lower during re-pressurization then during virgin reservoir depletion. For the specific field cases in Santarelli et al. (1998) horizontal total stress path coefficients $\gamma_{h,depl}$ between 0.42-0.7 have been reported, whereas for re-pressurization a value for $\gamma_{h,inj}$ as low as zero has been reported. This irreversibility of the stress path can cause fault reactivation to occur at reservoir pressures that are lower than the virgin reservoir pressure. Stress path irreversibility can be caused by the elasto-plastic behaviour of the reservoir rocks during reservoir first-time depletion. As the plastic deformation does not reverse during re-pressurization, the poro-elastic stress path during re-pressurization differs from the elasto-plastic stress path during first-time depletion (Santarelli et al. 1998). Other causes of differences in stress paths during depletion and injection can be fault slip during the depletion phase and differences in pore pressure loading during the depletion and injection phase, e.g. as shown for mechanism 2 in Chapter 2.

Whether the stress path during depletion or injection moves the stress conditions on the fault towards less stable conditions depends on the stress path gradient and the slope of the Mohr Coulomb failure envelope. Figure 32 presents the relation between Poisson's ratio, total horizontal stress path coefficient, the angle between fault normal and largest principal stress (i.e. vertical stress in extensional stress regime of The Netherlands) and the stress path gradient. In the same graph the position of the fault friction coefficient (μ=0.6) is indicated.

Figure 32 shows that for a fault dip of 75^0, a Poisson's ratio value of 0.2 (γ_h=0.75) and a fault friction coefficient of 0.6 (like in the base case scenario of section 3.2), the stress path during depletion and injection is almost parallel to the Mohr Coulomb failure envelope. This means that in a horizontally extended reservoir with uniform depletion or injection and no fault offset, the changes in SCU are expected to be insignificant. The graph also shows that during *injection* in a horizontal and laterally extended reservoir (no fault offset), assuming a fault friction coefficient μ of 0.6 and a fault dip of 75^0, for low total horizontal stress path coefficients (i.e. γ_h<0.75 in Figure 32) stress conditions on the fault move towards less stable conditions. For high stress path coefficients (γ_h>0.75) the stress path during injection diverges from the Mohr Coulomb failure line, with fault stresses moving towards more stable stress conditions.

Santarelli (1998) shows that during repressurization values of the horizontal stress path coefficients are relatively small compared to depletion, which means a potential increase of the seismicity potential during injection. In the present chapter, the impact of lower stress path coefficient during repressurization on fault stability during injection is investigated. The DIANA model used for analysis is similar to the DIANA model used in section 2 (basecase), but is extended with a different Poisson's ratio v_{inj} during the injection phase, to simulate the effect of stress path irreversibility.

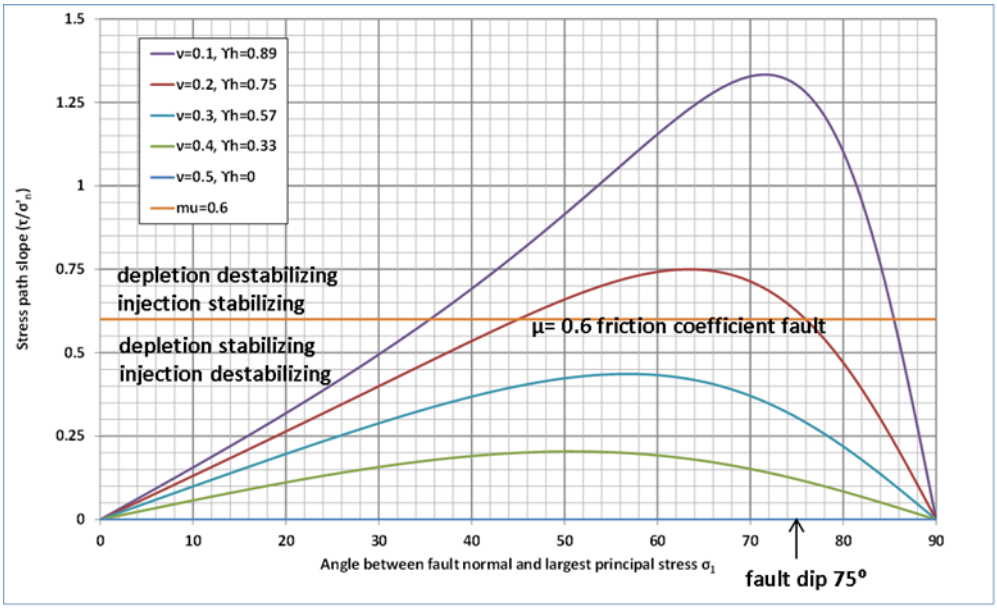

Figure 32: Stress path slope due to pore pressure changes in a horizontal laterally extended reservoir is a function of fault angle and horizontal stress path coefficient. For computation of the total horizontal stress path coefficient, a Biot's coefficient α=1 is assumed. Effective horizontal stress path coefficients can be derived from $\gamma'_h = 1-\gamma_h$.

4.2 Modelling approach

The effects of irreversible stress paths during production and injection are investigated using a 2D plane strain model in DIANA, with identical mesh geometry and properties as those used for the base case in Chapter 3, except for the changes noted below. Irreversibility of the stress paths is implemented by increasing Poisson's ratio values for the Slochteren Sandstone layer (both the gas and water saturated portion) during the injection phase. All other layer properties and loading conditions are unchanged with respect to the base case, which means no pore pressure increase in the Ten Boer clay is modelled during injection. Three DIANA runs are performed, as shown in Table 6.

Table 6: Overview of Poisson's ratio for the Slochteren Sandstone for the different cases studied. Stress path coefficients given are coefficients for total horizontal stress.

Case	**Slochteren Sandstone ν_{depl}**	**Slochteren Sandststone ν_{inj}**
Base case	0.20 ($\gamma_{h,depl}$ = 0.75)	0.20 ($\gamma_{h,inj}$ = 0.75)
Case 1	0.20 ($\gamma_{h,depl}$ = 0.75)	0.30 ($\gamma_{h,inj}$ = 0.57)
Case 2	0.20 ($\gamma_{h,depl}$ = 0.75)	0.40 ($\gamma_{h,inj}$ = 0.33)
Case 3	0.20 ($\gamma_{h,depl}$ = 0.75)	0.48 ($\gamma_{h,inj}$ = 0.08)

4.3 Modelling results

In this section, the results of the three runs described above are presented using the shear capacity utilization of the faults as well as total slipped length and maximum relative shear displacement. Additional figures with stress paths for selected points, the evolution of normal stress, shear stress, changes in shear capacity utilization (dSCU), and relative shear displacement can be found in Appendix C.

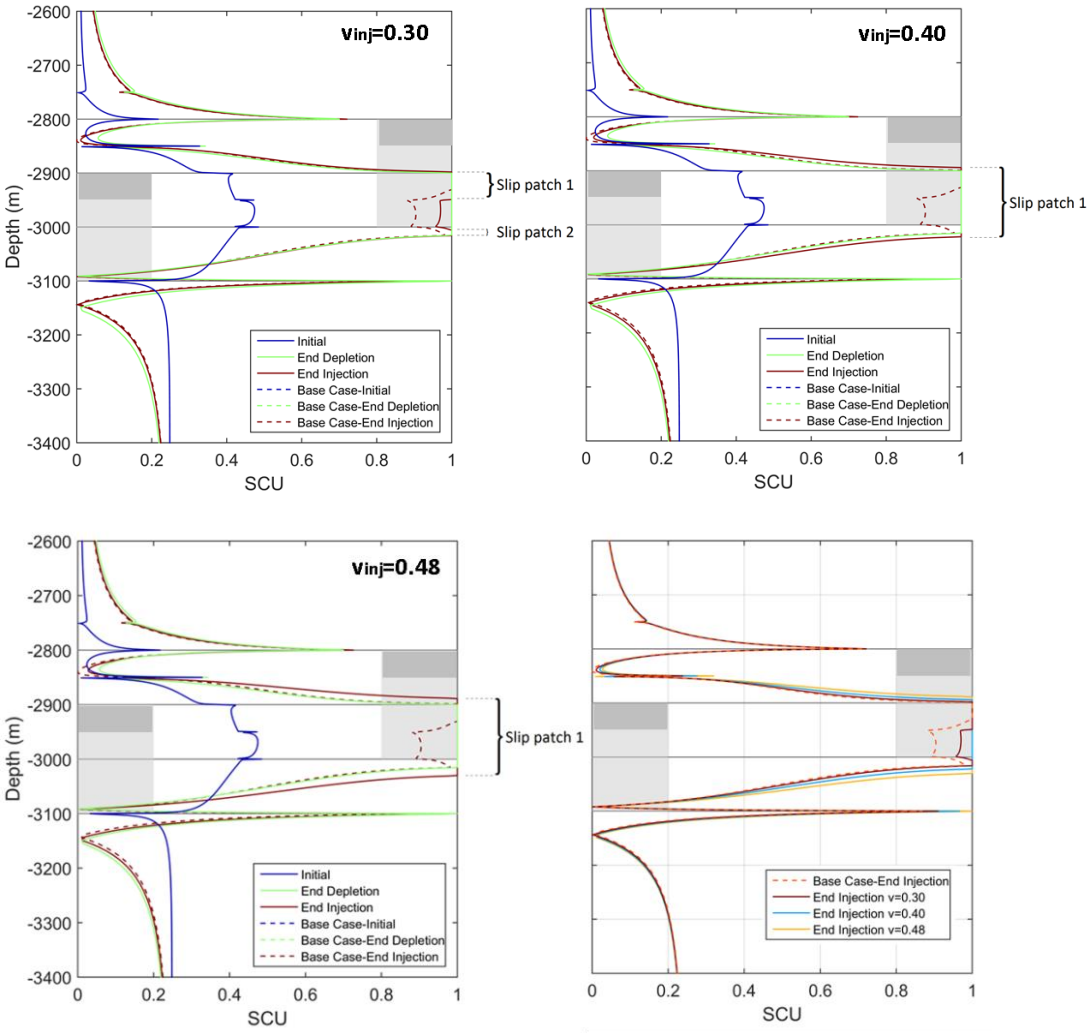

Figure 33: Shear capacity utilization (SCU) for the scenario with a Poisson's ratio v_{inj}=0.3, v_{inj}=0.4 and v_{inj}=0.48 during injection (presented as continuous lines). For comparison, the base case scenario with Poisson's ratio v_{inj}=0.20 is presented as a dashed line. The light-grey blocks on the left and right indicate the position of the reservoir (Slochteren Gas and Water) in the hanging wall and footwall respectively. The dark-grey blocks indicate the position of the low-permeability Ten Boer layer. The lower right plot shows the shear capacity utilization for all 3 scenarios of v_{inj}=0.30, v_{inj}=0.40 and v_{inj}=0.48 in one single plot. All displays have the same legend on the vertical axis.

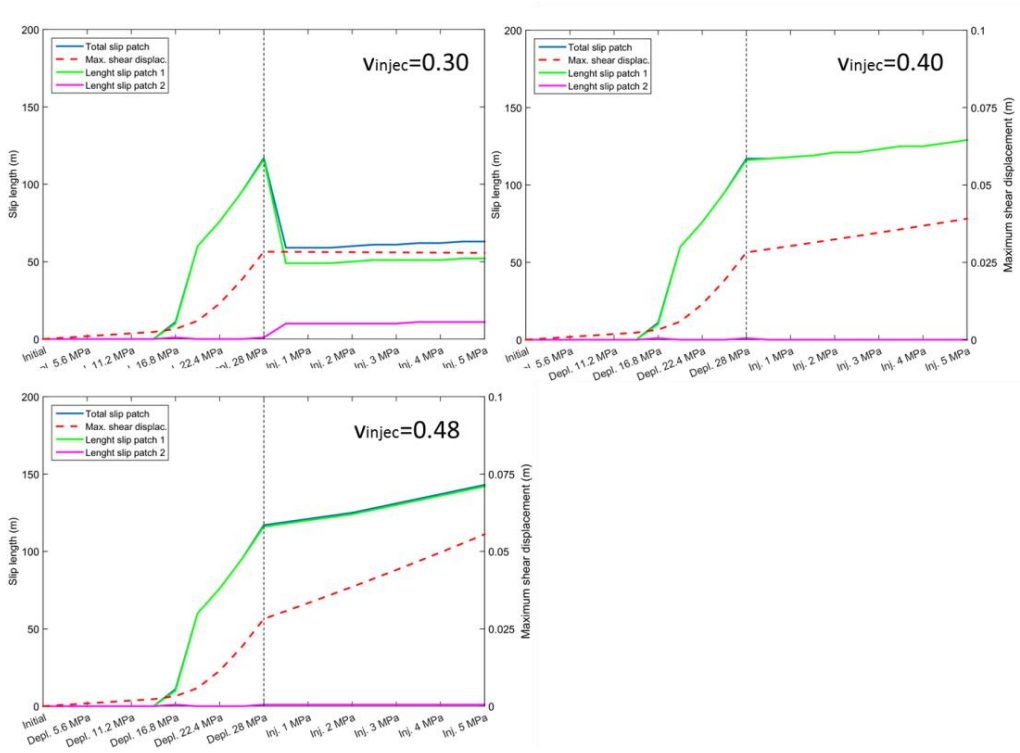

Figure 34: Evolution of maximum relative shear displacement and fault slip length during depletion and injection, for the scenarios with a Poisson's ratio of v_{inj}=0.3, v_{inj}=0.4 and v_{inj}=0.48 during injection. Using higher Poisson's ratios during injection to model the irreversibility of the stress path can lead to the growth of the total slip length and increased relative shear displacement. The increases in slip length and maximum relative shear displacement during injection are of the same order of magnitude as during depletion.

As Poisson's ratio of the reservoir rocks during depletion is similar to the base case (v_{depl} =0.2) for all three cases, lengths of the slipping fault and maximum relative shear displacements for depletion are equal to the base case (Figure 34). In all cases, the fault section at the juxtaposition of the Slochteren Ten Boer (hanging wall block) and the Slochteren Water (footwall) and at the juxtaposition of the Slochteren Water in both hanging- and footwall block is reactivated during depletion (Figure 33). Failure is also reached over a limited fault section at the juxtaposition of Slochteren Water (hanging wall) and underburden (footwall), just below the footwall reservoir block, and at the base of the hanging wall reservoir block.

The change of Poisson's ratio during injection has a marked effect on the slope of the stress path (compare to Figure 35). As mentioned before the slope of the stress path during injection is less steep for higher Poisson's ratio values and converges to failure more rapidly. Additional plots of stress paths are presented in Figure C 1.

For Case 1 (v_{inj} = 0.30), the fault segment at a depth of 2950 m to 3000 m is stabilized at the end of injection (SCU<1, see Figure 33). For Cases 2 and 3 (v_{inj} = 0.40 and v_{inj} = 0.48, respectively) fault segments which are slipping at the end of depletion do not stabilize during the injection phase. For Cases 2 and 3, the size of the slip patch and the maximum shear displacement continue to increase during the injection phase (Figure 34).

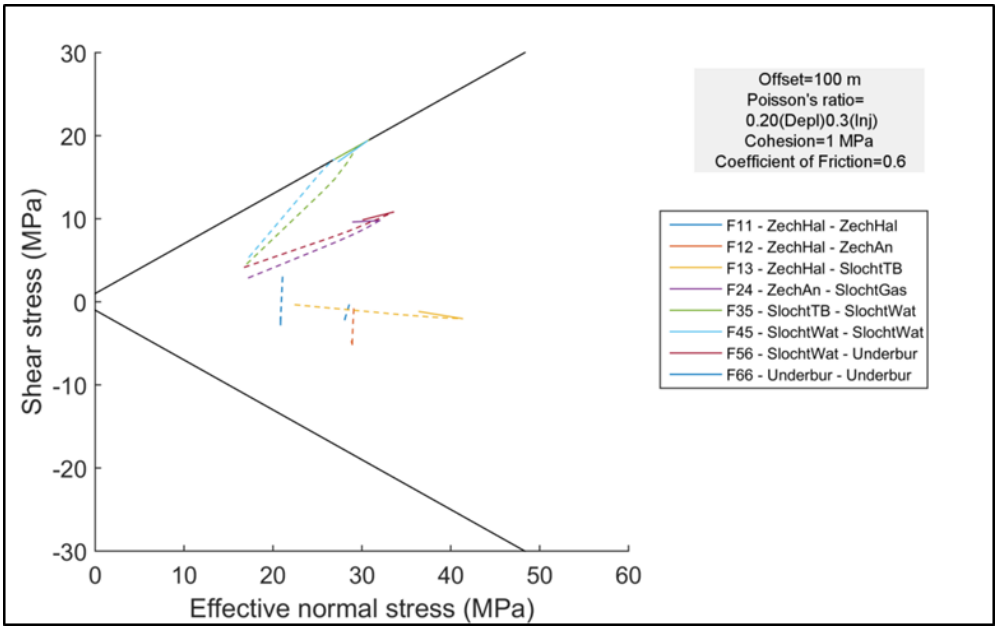

Figure 35: Stress paths for the Poisson's ratio v_{inj}=0.30 during injection scenario of mechanism 3. Dashed lines present the stress paths during depletion, solid lines the stress paths during injection.

Injection versus ongoing depletion

In the latter two scenarios (v_{inj}=0.40 and v_{inj}=0.48) the total slip length during injection increases in comparison to the slip length at the end of 28 MPa depletion. When the assumption is made that slip length is a proxy for the potential of induced seismicity, this means that in these cases the potential of induced seismicity increases, due to the irreversibility of the stress path resulting from plastic deformation during the first-time depletion phase. It is interesting to see how this situation compares to the situation of ongoing depletion. Here, the configuration of the base case model, as introduced in section 3.2, is used to model the effect of ongoing depletion on incremental relative shear displacement and the additional growth of the total fault slip length during ongoing depletion. The loading conditions for the base case model are adapted: Instead of a pore pressure increase of 5 MPa during injection, an additional pore pressure decrease of 5 MPa during ongoing depletion is modelled. In fact the scenario of ongoing depletion is similar to the scenario of increased depletion described in section 3.4.3, but without the injection phase. Maximum relative shear displacements and total slip length at the end of injection are compared with maximum relative shear displacements and total slip length after ongoing depletion.

Results are presented in Figure 36. This figure shows that total slip lengths after 5 MPa of ongoing depletion are similar to total slip lengths after injection for the v_{inj}=0.40 scenario. Maximum relative shear displacements after ongoing depletion are smaller than after injection for the v_{inj}=0.40 scenario. At a higher Poisson's ratio of v_{inj}=0.48, total slip lengths and maximum relative shear displacements are larger than for the case of ongoing depletion.

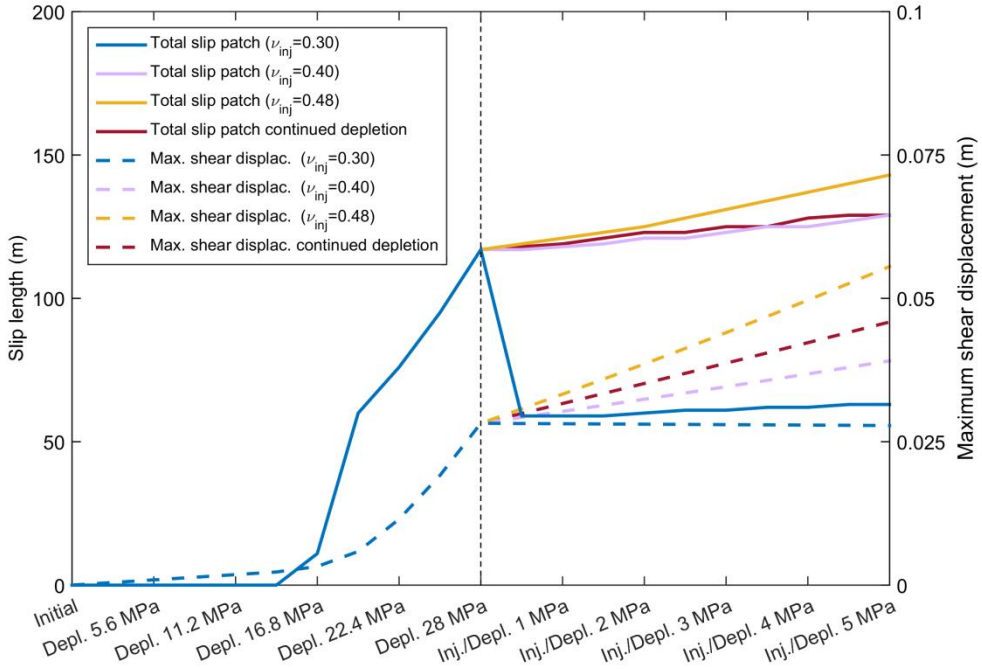

Figure 36: Comparison of maximum relative shear displacement and lengths of total slip patches for the scenario of ongoing depletion and the 3 scenarios of irreversible stress paths with v_{inj}=0.30, v_{inj}=0.40 and v_{inj}=0.48.

4.4 Discussion & conclusions

The effect of stress path irreversibility on fault stability is modelled by extending the DIANA model of section 2 with a different Poisson's ratio (v_{inj} =0.30, 0.40 and 0.48) during the depletion phase. Both the length of the fault segment, which is critically stressed at the end of injection, and the maximum relative shear displacement during injection are summarized in Table 7. Comparing slip lengths and relative shear displacements during injection and depletion shows that relative shear displacements and total slip length are higher for increasing Poisson's ratio values (as applied during injection). For a Poisson's ratio v_{inj}=0.4 and v_{inj}=0.48, total slip lengths are larger than those for the end of 28 MPa depletion case and equal to, respectively larger than, the total slip length when an additional ongoing depletion of 5 MPa is assumed (i.e. 33 MPa depletion). Maximum relative shear displacements for the v_{inj}=0.48 scenario are larger than for the scenario of ongoing depletion and no injection.

Current models show that the irreversibility of the stress path, caused by the elasto-plastic behaviour of the reservoir rocks during reservoir depletion and a limited rebound during repressurization, can lead to the growth of the total slip length and to the same order of magnitude for relative shear displacements as for depletion. Under the assumption that slip length can be used as a proxy (indicative estimate) for the induced seismicity potential, this means stress path irreversibility could potentially lead to an increase of the seismicity potential during injection. For the cases of V_{inj}=0.40 and V_{inj}=0.48, it is concluded that injection is not an efficient strategy to mitigate induced seismicity, and that injection may actually increase the seismicity potential.

Only few field data on the actual stress path coefficients during repressurization have been published in literature. As mentioned in the introduction, Santarelli et al. (1998) estimate a total horizontal stress path coefficient $\gamma_{h,inj}$ of almost zero in a North Sea field. The reservoir rock in the North Sea field described in this publication consists of poorly consolidated sandstones, but few data on other characteristics of the field are given. Nagelhout (1997) describe laboratory test results on Rotliegend reservoir rocks of the Norg underground gas storage field which indicate that 52% of the deformation during first-time loading cannot be recovered during unloading to initial conditions. Both observations indicate that a certain amount of stress path irreversibility is to be expected in the sandstone rocks. The absence of significant seismicity during the re-pressurization of the Bergermeer, Norg and Grijpskerk Rotliegend reservoirs on the other hand can be interpreted as a first indication that at a field scale for Rotliegend sandstone reservoirs the effect of differences in stress path coefficients during production and injection on fault stability is limited (TNO-report 2015 R10906). The availability of better material models for plastic deformation of the reservoir rocks during compaction, based on experimental work, field observations and field experiments, would facilitate further analyses of the effect of plasticity on stress paths and the effect of stress path irreversibility on seismicity potential during injection.

Table 7: Overview of maximum slip lengths and maximum relative shear displacements (rsd) along the fault during depletion and injection.

Scenario	**Maximum rsd depletion**	**Maximum rsd injection**	**Maximum slip length during depletion**	**Maximum total slip length during injection**
Base case: v_{depl}=0.20, v_{inj}=0.20	28.2 mm	0.8 mm	117 m	32 m
Poisson's ratio:v_{depl}=0.20, v_{inj}=0.30	28.2 mm	2.6 mm	117 m	63 m
Poisson's ratio:v_{depl}=0.20, v_{inj}=0.40	28.2 mm	11.2 mm	117 m	129 m
Poisson's ratio: v_{depl}=0.20, v_{inj}=0.48	28.2 mm	27.5 mm	117 m	143 m
Ongoing depletion scenario, v_{depl}=0.20	45.9 mm (28.2 mm+17.7 mm)	n.a.	129 m	n.a.

In summary:

- The irreversibility of the stress path, caused by the elasto-plastic behaviour of the reservoir rocks during reservoir depletion and a limited rebound during repressurization, can cause an increase in the slip lengths during injection. Hence, injection could potentially lead to an increase of the seismicity potential of the faults.
- In the scenario of v_{inj}=0.20 and v_{inj}=0.30 total slip lengths on a fault with 75º dip and 100 m offset decrease during the injection phase.
- In the scenario of v_{inj}=0.40 and v_{inj}=0.48 total slip lengths on a fault with 75º dip and 100 m offset increase during the injection phase. Total slip lengths at the end of the injection phase are larger than the total slip lengths in the scenario of ongoing depletion without injection. For the case of v_{inj}=0.40 and v_{inj}=0.48

injection is not an efficient strategy to mitigate induced seismicity, but may actually increase the seismicity potential.

- Little data is available on stress paths during re-pressurization. More experimental and field data on material and reservoir-scale behavior during re-pressurization is needed to assess the potential of injection-induced seismicity due to stress-path irreversibility.

5 Mechanism 4: Cooling and thermal stresses due to injection of cold N2

5.1 Introduction/description of mechanism

Injection of nitrogen at injection temperatures lower than ambient reservoir temperatures causes a gradual cooling of the reservoir rocks in the vicinity of the injection wells. Cooling of the reservoir rocks leads to a contraction of the reservoir rocks in the area where the temperature change occurs and induces additional thermal stresses. Thermal stresses caused by the cooling of the reservoir rocks can reach beyond the cooling-affected area. These thermal stresses introduce additional loading to the system and can have an adverse effect on the stability of the faults (see e.g. Ghassemi et al., 2007).

In a horizontal, laterally extended reservoir with uniform temperature changes, the change in horizontal and vertical total and effective stresses per unit temperature change can be computed by the following equation:

$$\frac{d\sigma_h}{dT} = \frac{d\sigma'_h}{dT} = \frac{E\alpha_T}{1-v} \tag{11}$$

and

$$\frac{d\sigma_v}{dT} = \frac{d\sigma'_v}{dT} = 0 \tag{12}$$

In which dT is temperature change, E is Young's modulus of the reservoir rocks and α_T is the linear thermal contraction coefficient of the rocks. Based on $\alpha_T = 10^{-5}$/ºC, E = 15 GPa and Poisson's ratio v = 0.2 as used in the base case scenarios in this study, a decrease of 0.19 MPa per 1 ^{0}C temperature drop is computed, which gives a total and effective horizontal stress path coefficient for temperature change of $\gamma_{h,T} = \gamma'_{h,T}$ = -0.19 MPa/ºC. In a horizontal laterally extended reservoir (with no fault offset) and a uniform temperature decrease, no change in either total or effective vertical stress is expected, hence $\gamma_{v,T} = \gamma_v$ = 0 MPa/ºC. The effect of a temperature decrease of 10 ºC on the stress path on a fault with a fault dip of 75 ºC (no fault offset) in a horizontal and laterally extended reservoir is shown in Figure 37. The slope of the stress path is negative, resulting in a stress path which converges rapidly onto the Mohr Coulomb failure line for a decrease in temperature.

For comparison, Figure 37 also presents the stress path on a fault with a fault dip of 75ºC (no fault offset) in a laterally extended reservoir caused by a uniform pressure increase of 10 MPa during injection (no cooling). As described in section 4.1, total and effective horizontal stress path coefficient for pressure changes caused by depletion or injection are respectively γ_h = 0.75 and γ'_h = 0.25. Vertical total and effective stress path coefficient are γ_v = 0 and γ'_v = 1. The stress path for a Poisson's ratio of v = 0.2 is almost parallel to the slope of the failure line, resulting in very small changes in fault shear capacity utilization during injection. In contrast, the stress path resulting from the temperature decrease has a large effect on the shear capacity utilization of the fault.

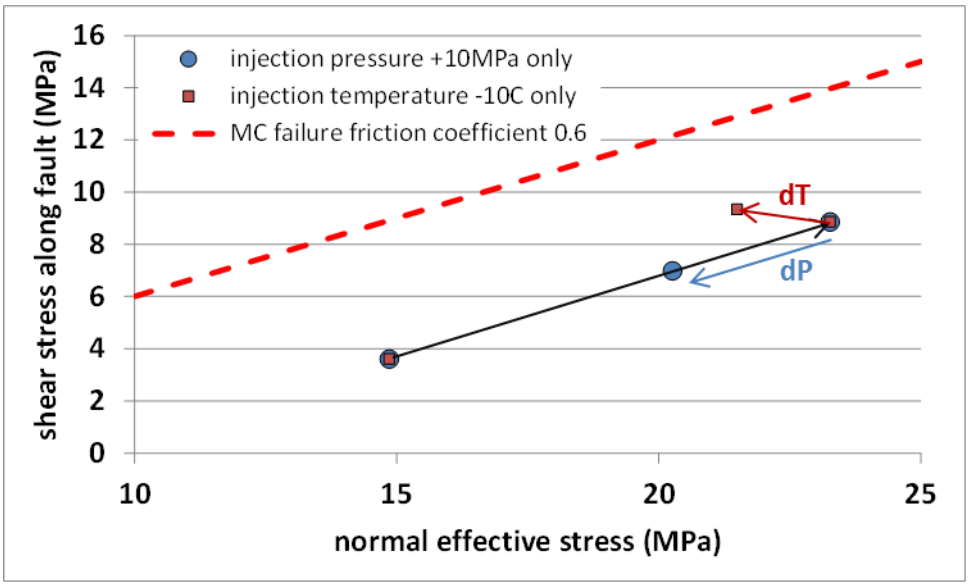

Figure 37: Example of temperature effect and pressure effect on stress paths followed in a horizontal, laterally extended reservoir with no fault offset. In dark-red effect of temperature change dT=-10^{0}C. In blue effect of pressure increase dP=+10bar.

The objective of this chapter is to analyse the effect of the additional thermal loading due to the injection of nitrogen at injection temperatures below ambient reservoir temperatures on fault reactivation and the potential of induced seismicity. The effect of nitrogen injection on the temperatures of the reservoir rocks is analysed with the ECLIPSE reservoir simulator. The effect of reservoir cooling and related thermal contraction of the reservoir rocks around the injection wells on fault stability is analysed in DIANA. Both cases of injection at temperatures lower than reservoir rocks and an injection case without temperature changes are modelled, to obtain more insight in the contribution of the thermal effects relative to the pressure effects.

5.2 Modelling approach

The modelling approach which is chosen differs from the modelling approach used for mechanism 2 and 3. A single-well model in ECLIPSE and a radial symmetrical single-well model in DIANA are used to quantify the temperature-, pore pressure gradients and poro-elastic and thermal stresses around a single injection well. The lithologies, depths of lithologies and basic properties used for modelling in DIANA are similar to those used for the base case scenario of mechanism 2 (presented in Table 3). As planar fault structures cannot be included into a radial symmetrical model, the faults are not explicitly modelled in DIANA. Additional parameters used in ECLIPSE are described in section 5.2.1 below. Reservoir properties (thermal, transport and mechanical) of individual layers are assumed to be homogeneous.

5.2.1 Modelling of temperature changes

Single-well calculations are conducted in ECLIPSE to determine the temperature and pore pressure gradients around a single injection well and the extent of the

area affected by cooling and pore pressure changes. A 3D temperature field around a single injector well is modelled in the black oil reservoir simulator ECLIPSE100 (Schlumberger 2014). In accordance with the base case for mechanisms 2 and 3, nitrogen injection is modelled over the entire reservoir section of 150 m thick Slochteren Sandstone at a depth of 2850 m to 3000 m. Reservoir pore pressures are assumed to be 70 bar at the start of the injection phase. This value is equal to the pressure at the top of the Slochteren Sandstone in the base case model for mechanisms 2 and 3. Initial temperature of the reservoir rocks is 94 ºC. Nitrogen is injected at a temperature of 10 ºC for a period of 20 years.

Temperature changes caused by the injection of nitrogen can be simulated in compositional mode (e.g. with ECLIPSE300), however, for this analysis it is assumed that the reservoir is initially filled with nitrogen and therefore no compositional modelling is required. Main properties and assumptions for modelling in ECLIPSE are summarized in Table 8. Nitrogen properties used for modelling are presented in Table D 1.

Table 8: Main properties and assumptions for single well reservoir model in ECLIPSE.

Single well reservoir model	
Reservoir depth	2800 m
Reservoir thickness	150 m
Reservoir permeability	500 mD / 50 mD (horizontal/vertical)
Porosity	0.2
Net to Gross ratio	0.8
Pressure at start of injection	70 bar
Ambient temperature of reservoir rocks	94 °C (10 + 30 °C/km)
Permeability of top seal (Ten Boer)	0.1 mD/0.001 mD (horizontal/vertical)
Boundary conditions side	Constant pressure for pressure maintenance
Bottom seal	No flow
Gas Water Contact (GWC)	<3000 m
Capillary Pressure (Pc)	Not taken into account (reservoir at Swr=0.2, where Swr is the irreducible water saturation)
Relative permeability	Standard Petrel sandstone
Water salinity	200.000 ppm (1150 kg/ m^3)
Well properties	
Injection rate	3.500.000 sm^3/d
Injection temperature	10°C
Injection period	20 years
Well bore diameter	0.1905 m
Well perforation length	200 m (fully perforated)
Skin factor	0
Operating constraint	Gas rate
Maximum bottom hole pressure (BHP)	250 bar
Thermal properties of the rock	
Thermal conductivity of the rock	304 kJ/m/d/°C
Heat capacity rock	@ 25°C: 1988 kJ/rm^3/°C @ 90°C: 2200 kJ/rm^3/°C
Heat capacity fluids (N2/water)	@ 10°C: 2.40 / 4.2 kJ/kg/°C @ 94°C: 5.36 / 4.2 kJ/kg/°C

Temperatures are calculated in ECLIPSE for a number of selected time steps ranging from 6 months to 20 years after the start of injection. The temperature results are used to define the spatially variable, time-dependent thermal loads in DIANA. The modelled temperatures are shown in Figure 38.

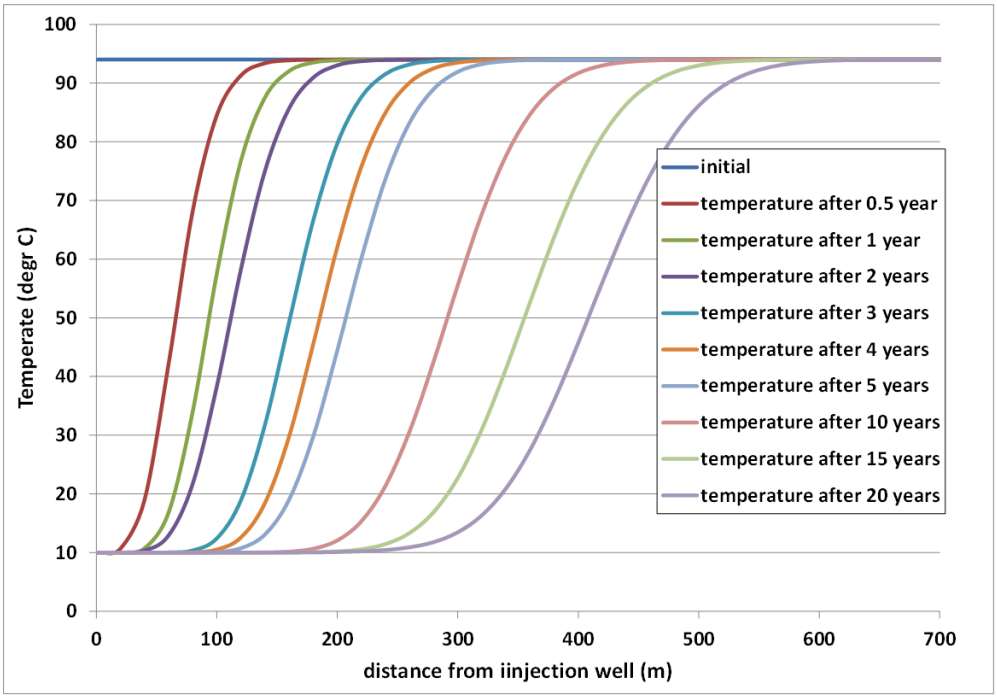

Figure 38: Temperatures around injection well modelled in ECLIPSE.

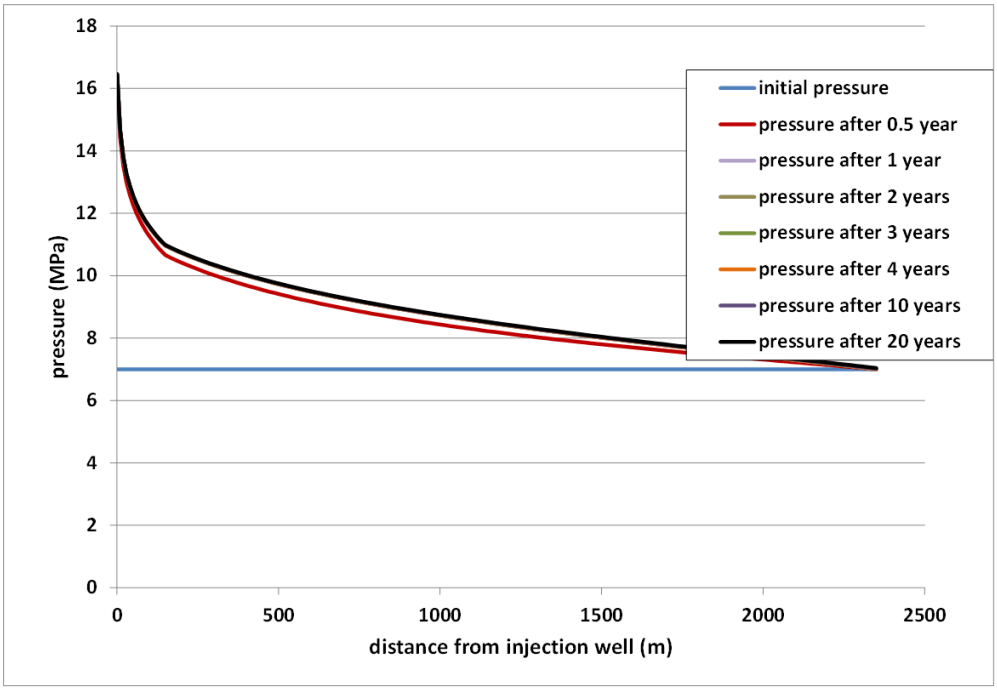

Figure 39: Pore pressure evolution around injector well modelled in ECLIPSE.

Figure 38 shows that for an injection period of 20 years, the extent of the temperature changes around the injection well is limited to a radial distance of approximately 600 m. After 20 years of injection, the reservoir temperatures within a radius of 250 m from the injection well fall as low as 10ºC. The extent of the pore pressure changes due to injection reaches much further from the well, i.e. up to a distance of more than 2.5 km (Figure 39). Reservoir pore pressures at the point of injection increase up to 160 bar.

5.2.2 Modelling of poro-elastic- and thermal stresses and stresses on faults

The effect of temperature changes on thermal stresses which occur during injection is investigated using an radial symmetric model in DIANA[3]. The reservoir rocks, caprock and under and overburden are modelled with 8-node quadrilateral axisymmetric elements. The elements represent linearly elastic material behaviour and do not have an associated failure criterion. Lithologies, depths of layers and properties are identical to those used for the base case described in section 3.2. To model the thermal response of the reservoir rocks, a linear thermal coefficient α_T of 10^{-5}/ºC is assigned to the reservoir rocks. Temperature loads and pore pressures from ECLIPSE are mapped onto the DIANA radial symmetric finite element mesh, see Figure 40. Temperature loads are only imposed on the Slochteren reservoir rocks and no temperature changes are modelled in the caprock, under- and overburden. ECLIPSE modelling shows that the cooling of the Ten Boer caprock is limited.

Finite element analysis in DIANA is used to investigate the effects of reservoir depletion, nitrogen injection and cooling on fault stability. The model is initialized with stresses based on the weight of the overburden and the effective stress ratio (K'_0) values from Table 3. Initial pore pressure in the reservoir is assumed to be 350 bar. Depletion is simulated by a pore pressure decrease of 280 bar in the Slochteren Gas and Slochteren Water. The injection of nitrogen is modelled using the pore pressure and temperature gradient around the well obtained from ECLIPSE.

[3] As a quality check of the numerical results, numerical solutions for a model with a uniform temperature change were compared to the analytical solution and were found to be equal.

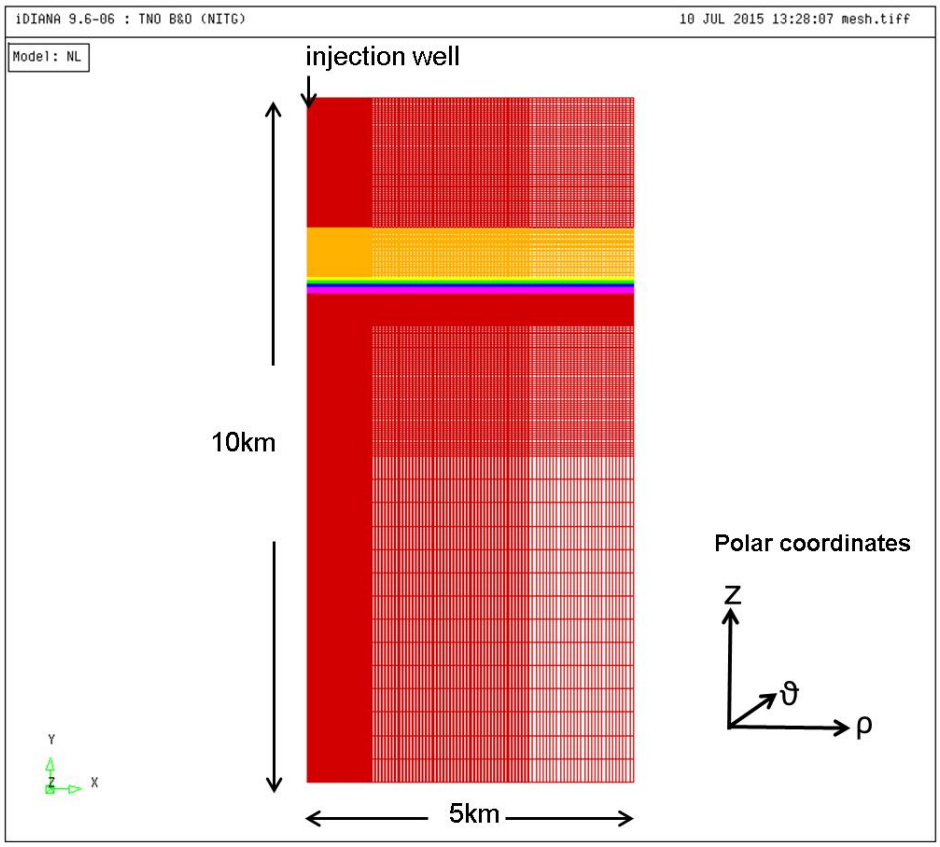

Figure 40: Geometry of the radial symmetric finite element mesh in DIANA: Orange: Zechstein halite, yellow: Zechstein anhydrite, green: Ten Boer, blue: Slochteren gas, magenta: Slochteren Water and red: Over-and underburden.

A stability assessment of the faults is performed by analyzing the changes in shear capacity utilization on virtual faults located at different distances from the injector well. For the analysis, a set of fault planes is defined at distances of 100 m, 300 m and 400 m of the injection well. Fault planes have varying dip and dip direction, i.e. faults dip towards and away from the injection well. The faults itself are not included in the DIANA mesh and stresses from DIANA are projected onto the virtual faults (see Figure 41).

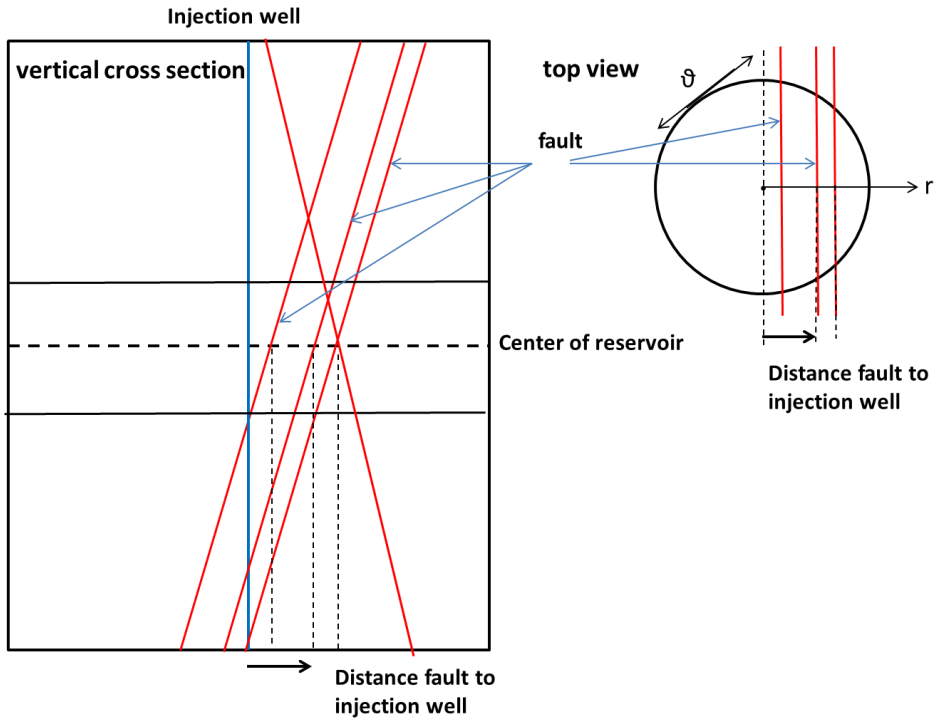

Figure 41: Schematic presentation of fault stability analysis. Left schematic vertical cross section. Right: Top view of intersection of fault planes and radial symmetric mesh. Virtual fault planes are defined at different distances from the injection well. Stresses in DIANA are mapped onto these virtual fault planes and shear and normal effective stresses on the fault planes are computed, defining shear capacity utilization of the faults.

In the approach for modelling the pore pressure and temperature field in ECLIPSE and the poro-elastic and thermal stresses in DIANA, a number of simplifications and assumptions have been made, which are summarized below:

- Dependency of N_2 density on temperature is not accounted for;
- The reservoir is initially filled with N_2 (no compositional model);
- No well modelling is performed;
- Homogeneous reservoir properties are used, which will have an impact on propagation of the pore pressure and temperature front, and on poro-elastic and thermal stress changes;
- Temperature changes caused by the Joule - Thomson effect are not accounted for;
- Possible fracturing due to injection at temperatures lower than ambient reservoir temperatures is not accounted for;
- Possible fault slip and stress transfer is not accounted for;
- Faults have 0 m offset.

5.3 Modelling results

Figure 42 shows the displacements field in the reservoir and surrounding rocks after 20 years of nitrogen injection (see Figure 38 and Figure 39 for temperature, respectively pore pressure gradients). The displacements in Figure 42 show that the entire reservoir section that experiences cooling contracts over its full thickness.

Displacements are not limited to the reservoir rocks, but also occur in the neighboring rocks, i.e. part of the caprock above and the underburden below. Figure 42 shows that the top of the reservoir moves downward by 3 cm, while the reservoir base moves upward by 3 cm. Displacements also occur in the part of the reservoir which is not affected by the change in temperature itself.

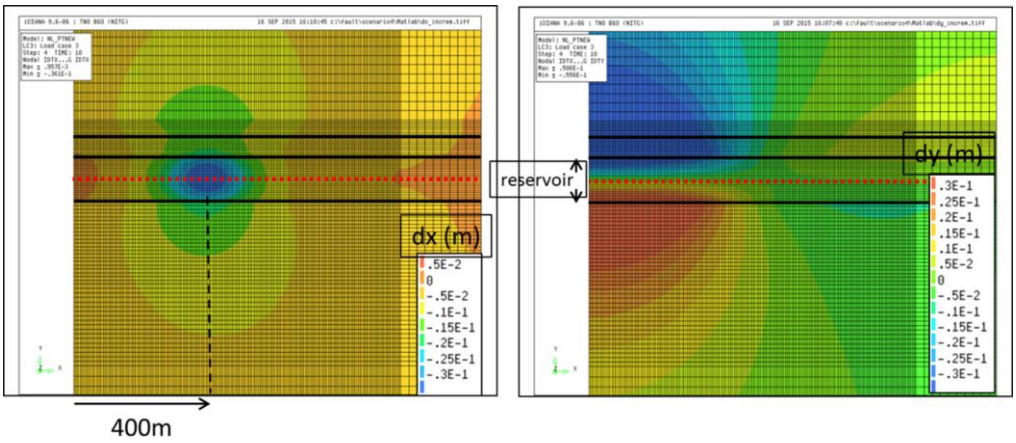

Figure 42: Horizontal (left) and vertical (right) displacement caused by thermal contraction of the reservoir rocks after 20 years of nitrogen injection. Red dashed lines indicate the depth on which Figure 43 is based.

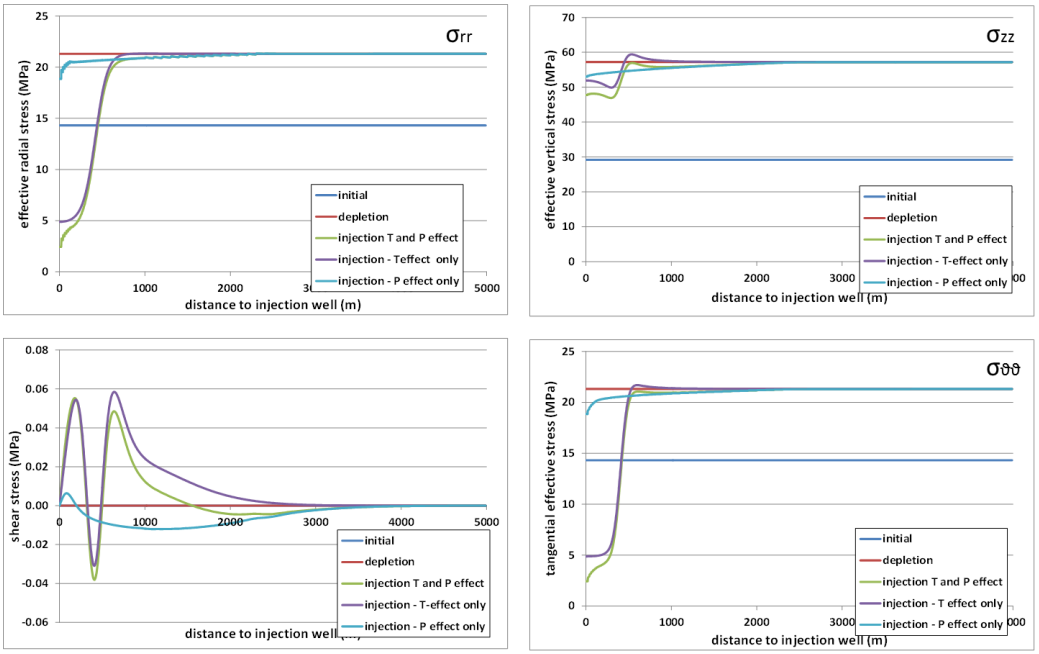

Figure 43: Element stresses: Radial effective stress σ'_{rr} (top left), vertical effective stress σ'_{zz} (top right), shear stress σ_{rz} (bottom left) and tangential effective stress $\sigma'_{\vartheta\vartheta}$ (bottom right) computed for the radial symmetric mesh in DIANA, for initial stress conditions, at the end of depletion (red line) and after 20 years of injection. Injector is located at 0 m distance. Stresses are presented for centre of reservoir at a depth of 2925 m below surface level. Model results for combined temperature and pressure effects (green line) and model results for temperature only (purple line) and pressure only (blue line) effects during injection are also shown.

Figure 43 presents initial reservoir stresses, stresses at the end of uniform depletion and the stresses computed in the radial symmetric DIANA model due to the simultaneous increase in pore pressure and thermal loading, modelled for 20 years of nitrogen injection. Stresses are shown at the centre of the reservoir, at a depth of 2925 m, with increasing distance from the injection well. Due to the contraction of the reservoir rocks in the region affected by cooling, the radial effective, tangential effective and vertical effective stresses become less compressive compared to the stresses at the end of depletion. When compared to the stresses at the end of depletion, changes of almost 19 MPa are observed near the injection well for both horizontal radial effective and tangential effective stresses, when both the poro-elastic and thermal effects of nitrogen injection are accounted for. These stress changes rapidly decrease with increasing distance from the injector. To distinguish between the contributions of poro-elasticity and thermal effects, stress results are also presented for a model in which only temperature changes/only pore pressure changes during injection are accounted for. Figure 43 clearly shows that poro-elastic and thermal stresses during injection add up and may locally counteract one another. Comparison of green lines (pressure and thermal effects), purple lines (thermal effects only) and blue lines (pressure effects only) shows that the thermal effects are much larger than the poro-elastic effects related to the imposed pore pressure increase. This difference between the thermal and poro-elastic effects is most pronounced for the horizontal stresses σ_{rr} and $\sigma_{\theta\theta}$. Contraction of the reservoir rocks in the area of cooling has a very large effect on the horizontal stresses, causing a reduction of the horizontal effective stresses.

Fault planes of 60º and 75º dip, with dip orientations both in the direction of the injection well and away from the injection well are defined at distances of 100 m, 300 m and 400 m of the injection wells (see Figure 41). On these faults a regular grid is defined with grid point distances of 10 m in both directions. Cartesian grid point coordinates of the grid are converted to polar coordinates for every fault plane. DIANA stress results are interpolated and mapped onto the polar grid point coordinates of the fault planes and both effective normal and shear stresses on the faults are computed for every grid point. Effective normal stress and shear stress on the faults are then used to compute shear capacity utilization on the fault, assuming a friction coefficient value of 0.6 and a cohesionless fault.

In Figure 44 the change in SCU is shown for a fault with 75º dip and dip direction towards the injection well. Shear capacity utilization is computed for initial conditions, the end of depletion and after an injection period of 20 years. Both the effect of the pore pressure and the effect of temperature changes is taken into account. Computed shear capacity utilization can exceed the value of 1 as only elastic material behavior is included in the DIANA model. Additional figures for changes in shear capacity utilization for different combinations of fault distance and dip are presented in Appendix D. The changes in SCU for these faults, which are shown on the vertical sections, are maximum changes as values are plotted at minimum distance from the injection well (see Figure 44, lower right plot). Figure 44 (and Figure D 3) show that the changes in shear capacity utilization are negligible at radial distances larger than 500 m from the injection well.

Figure 45 gives the change in normal effective stress, shear stress and shear capacity utilization after 20 years of injection, projected on the fault plane itself.

Values are plotted for a fault dipping 75º away from the injection well and located at a distance of 300 m from the injection well. Both the effect of the pore pressure and temperature changes is taken into account. The fault section at reservoir level undergoes a reduction of the normal effective stress and local increase in total shear stress, which increases the tendency for fault slip. Fault sections in the under- and overburden also experience an increase in SCU. Just above the reservoir the fault section in the Ten Boer clay locally moves towards more stable conditions.

As illustrated by Figure 45, changes in SCU are localized around the injection well and rapidly diminish with increasing lateral distance from the injection well. Figure D 1 and Figure D 2 give fault shear capacity utilization after 20 years of injection for different fault distances and fault dip of 75º and a more critical dip of 60º, taking into account both thermal and poro-elastic effects. Shear capacity utilization of the faults at radial distances of 100 m, 300 m, and 400 m locally exceeds the value of 1, which means that these faults can slip due to the thermal stresses. Shear capacity utilization at the fault plane at a radial distance of 500 m after 20 years of injection is below 1 (see also Figure D 1 and Figure D 2).

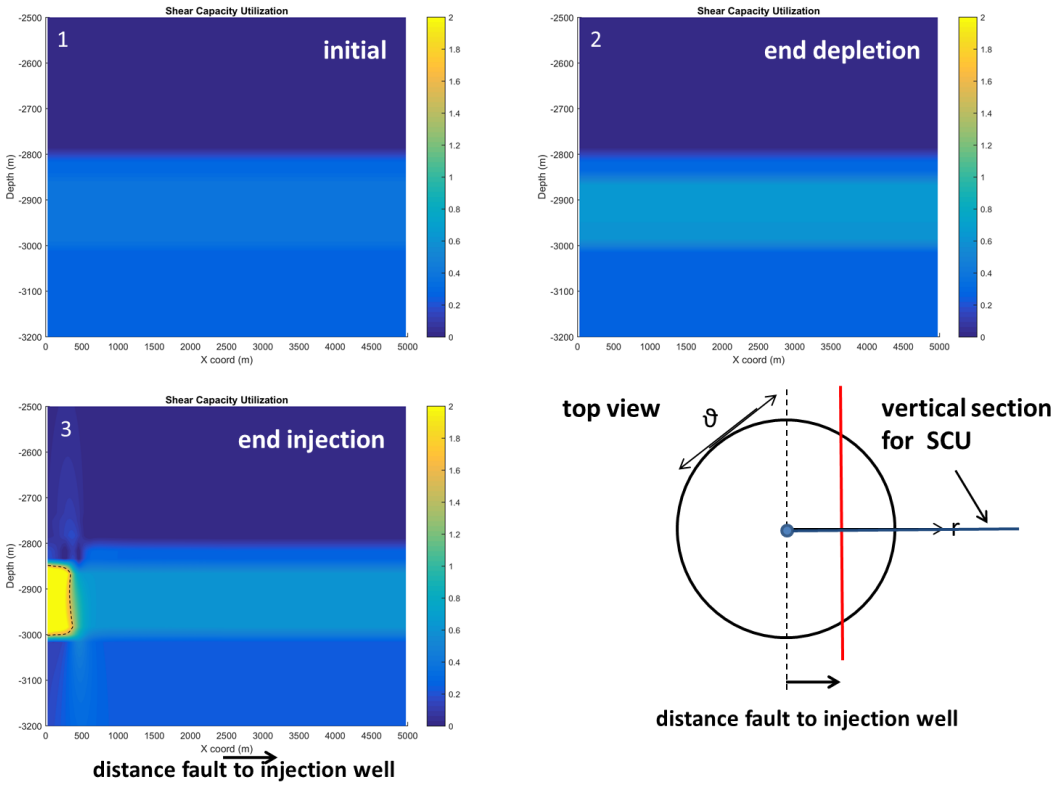

Figure 44: Shear capacity utilization (SCU) along a vertical section perpendicular to the strike of the faults: 1) SCU for initial stress conditions, 2) SCU at end depletion, 3) SCU after 20 years of injection. Lower right graph presents location of vertical cross section perpendicular to the faults. Fault is presented in red. Both poro-elastic and thermal effects are taken into account.

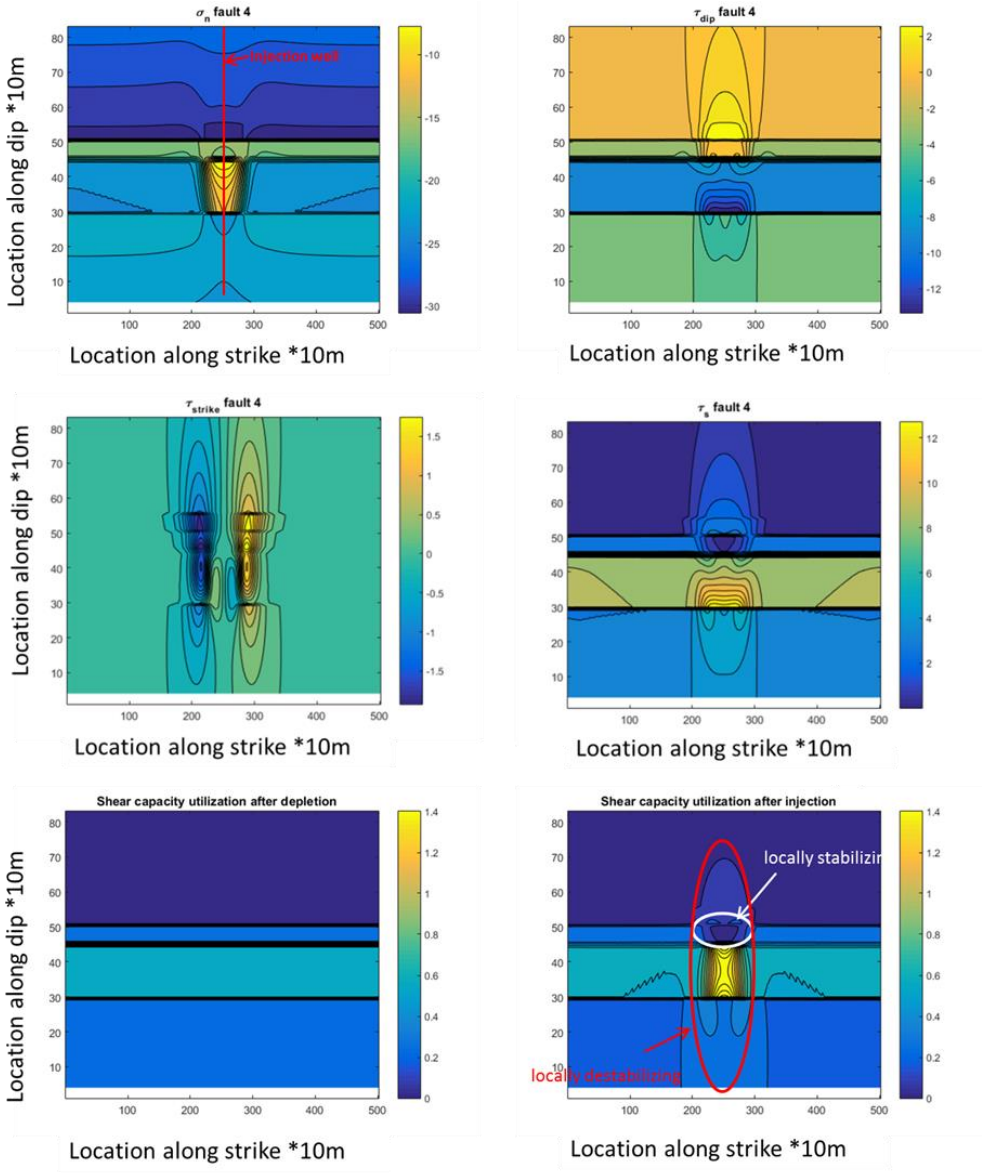

Figure 45: Upper two rows, clockwise: Effective normal stress, shear stress component in along dip direction, total shear stress along the fault and shear stress component in strike direction after 20 years of injection. Bottom row: shear capacity utilization at the end of depletion (left) and shear capacity utilization at the end of injection (right). Values are computed for a fault dipping 75^0 away, and located at a distance of 300 m, from the injector. Both poro-elastic and thermal effects are taken into account.

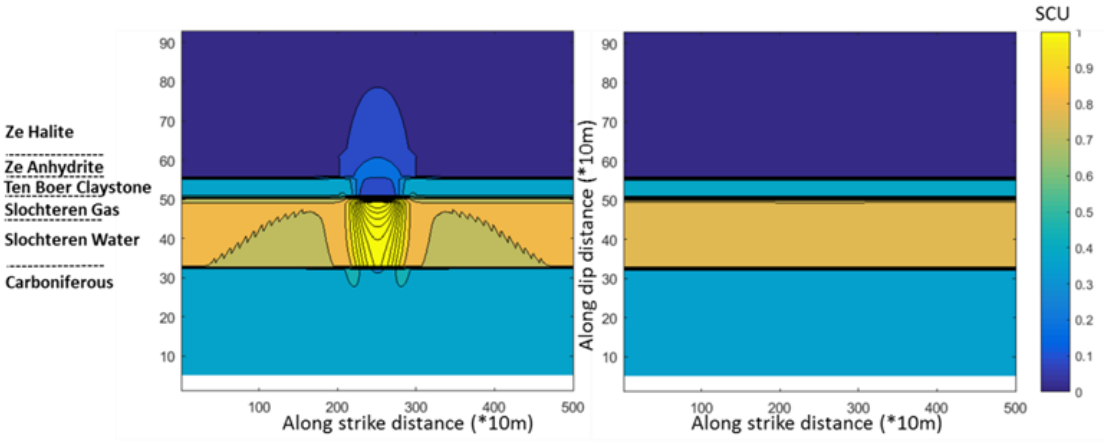

Figure 46: Shear capacity utilization (SCU) after 20 years of nitrogen injection. Left: Shear capacity utilization taking into account poro-elastic and thermal effects. Right: Shear capacity utilization taking into account the poro-elastic effects due to pore pressure increase only. Values are computed for a fault dipping 75^0 away, and located at a distance of 300 m, from the injector. Dashed lines on the left-hand side of the figure presents the position of the formations. Note that scale of colorbar for SCU in this plot differs from scale used for SCU in Figure 45.

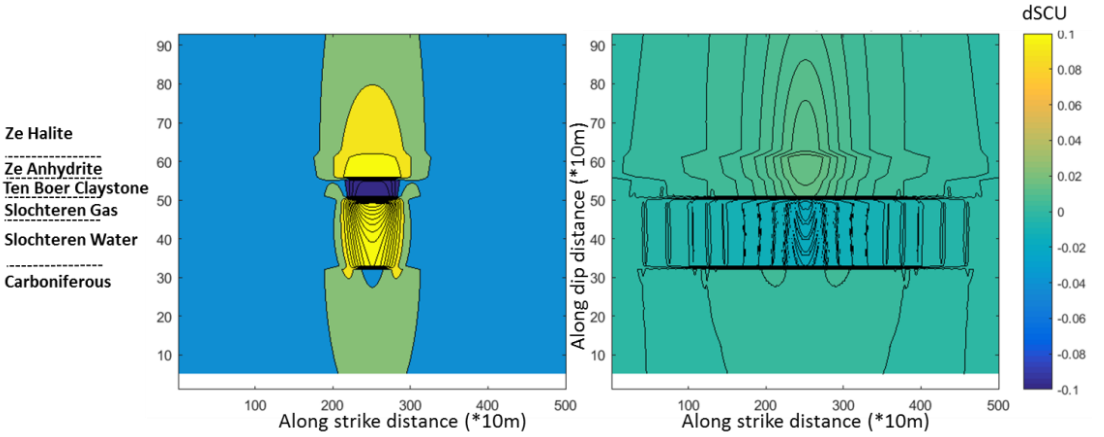

Figure 47: *Changes* in Shear capacity utilization (dSCU) after 20 years of nitrogen injection. Left: Shear capacity utilization taking into account poro-elastic and thermal effects. Right: Shear capacity utilization taking into account the poro-elastic effects due to pore pressure increase only. Values are computed for a fault dipping 75^0 away, and located at a distance of 300 m, from the injector. Dashed lines on the left-hand side of the figure presents the position of the formations.

Figure 46 compares the shear capacity utilization on a fault when thermal and poro-elastic effects occur simultaneously (right-hand side) with the SCU on the same fault which only feels the poro-elastic effects during injection (left-hand side). Figure 47 shows the change in shear capacity utilization (dSCU), due to thermal and poro-elastic effects (right-hand side) and poro-elastic effects only (left-hand side). Both figures demonstrate that the effect of pore pressure changes and poro-elasticity on the shear capacity utilization and fault stability is small. An explanation for the negligible impact of pore pressure changes on SCU is the absence of fault offset. The value of Poisson's ratio for the reservoir (ν=0.2) translates into a horizontal stress path coefficients (uniform depletion) of γ_h = 0.75 (γ'_h = 0.25), which for a fault

with friction coefficient value of 0.6 produces very small changes of SCU during depletion and injection (see Figure 32). Even though pore pressure gradients are present around the injection well (Figure 39), these pore pressure gradient have an almost negligible effect on SCU and fault stability.

5.4 Discussion & conclusions

Injection of nitrogen at injection temperature tens of degrees centigrade lower than ambient reservoir temperatures causes cooling of the reservoir rocks around the injection well. Single well simulations in ECLIPSE show that for the modelled geometry, reservoir and geomechanical parameters, and operational injection parameters, cooling of the reservoir rock due to the injection of nitrogen is largely confined to a distance of 600 m from the injection well for an injection time period of 20 years. Due to the contraction of the rocks in the area where cooling occurs, and in addition to poro-elastic stress changes, thermal stresses are induced. Whilst for the chosen scenario the effects of increasing pore pressures and increasing gradients in pore pressures around the injection well is almost negligible, the effect of temperature changes and thermal stresses is significant. The local decrease in normal effective stresses and increase in shear stresses due to the contraction of the reservoir rocks causes a local increase of shear capacity utilization of the faults. Model results show that the largest thermal effects are expected on faults which are located close to the cooling-affected zone, i.e. within a radial distance of approximately 500 m from the injection well (for the modelled time period of 20 years). Though changes in normal effective stress and shear stress on the fault are localized, they are significant and may lead to the onset or the continuation of fault slip during the injection phase.

The model described above is based on input parameters for reservoir rocks and injection rates, which are thought to be realistic and representative for nitrogen injection into a typical depleted Rotliegend reservoir. No sensitivity analysis on the impact of the variation of reservoir, well and injection parameters on the temperature and pressure gradients and thermal stresses has been performed. Both temperature and pressure gradients and the propagation of the temperature front around the injection well will depend on chosen model parameters, such as reservoir properties (e.g. thickness, permeability, thermal properties, elastic parameters), well and injection parameters (rates, volumes and temperatures). It is worth noting here that an increase in injection temperature is to be expected due to the pressure increase over time. Therefore, the assumption of a constant injection temperature of 10ºC during the entire injection period is at the more conservative end of the spectrum.

In summary:

- Changes in normal effective stress and shear stress on the fault are localized, but significant and can lead to the onset or the continuation of fault slip during the injection phase.
- The effect of a temperature drop of 1ºC on the shear capacity utilization (SCU) is much larger than the effect of 1 MPa pressure increase on SCU, as stress paths due to temperature changes have a negative slope and converge onto the Mohr Coulomb failure envelope much faster than stress paths for pressure changes (positive slope).

- When nitrogen is injected at temperatures of 10ºC for a period of 20 years, faults within a radial distance of 500 m of the injection well can be brought to failure.

6 Conclusions and recommendations

Pressure maintenance by injection of nitrogen is considered to be one of the options to mitigate induced seismicity during gas production. Injection itself can however also be a cause of induced seismicity. In this study, the geomechanical effects of injection of nitrogen for pressure maintenance in a producing reservoir and the potential consequences for fault stability and injection-induced seismicity were analyzed. At the start of the study, four mechanisms were identified which can potentially lead to injection-induced fault reactivation and induced seismicity:

1. Differential pressure evolution and stress arching;
2. Pressure diffusion into faults with higher permeability than reservoir rocks;
3. Irreversibility of stress paths during production and injection, e.g. due to irreversible plastic deformation;
4. Cooling and thermal stresses due to the injection of gas at injection temperatures lower than ambient reservoir temperatures.

Geomechanical models were used to assess the importance of the above mechanisms. Geometry of the reservoir and burden, initial stresses and pore pressures and geomechanical parameters were chosen in such a way as to be representative for a typical Rotliegend reservoir in the northern part of the Netherlands. A number of pressure scenarios for depletion and injection were defined for this study, which are thought to be realistic simulations of the pressure evolution in a producing reservoir, in which injection of nitrogen occurs with the aim of pressure maintenance. Main findings for the four mechanisms are given below.

Mechanism 1: Differential pressure evolution and effects of stress arching.
Model results show that differential pore pressures and related stress arching has a very limited effect on the fault stability during injection. Though differences in pore pressures can evolve in a producing reservoir in which pore pressures are maintained by local injection, pressure gradients are generally small and stress arching effects are very small. Models have shown that differences between stress path coefficients for the scenario of a uniform reservoir depletion without lateral gradients in pore pressure and 3 dispersed injection/production scenarios of 4 km, 8 km and 16 km wavelength and amplitudes of 2 MPa are less than 3%. The effect of differential pore pressures caused by dispersed injection/production on fault stability is therefore expected to be negligible.

Mechanism 2 (pressure diffusion into faults):
Analysis of mechanism 2 shows that locally high pore pressures, which result from the diffusion of pore pressures into faults in low-permeability rocks such as the Ten Boer clay, can locally have a negative effect on the stability of the faults. As a consequence of locally high pore pressures in the faults and the absence of a poro-elastic response in the adjacent low-permeability rocks, faults segments in the low-permeability rocks which are already critically stressed during depletion can remain critically stressed during the injection phase. However, at the same time, the injection causes a poro-elastic rebound of the high-permeability reservoir rocks which results in a stabilization of the fault segments within the reservoir, which were critically stressed at the end of depletion. All scenarios modelled with faults critically stressed at the end of depletion, show a decrease of the total slip lengths during the

injection phase (see Figure 48). Hence, under the assumption that total slip lengths can be used as a proxy for induced seismicity, it can be concluded that in a reservoir with faults already critically stressed during the depletion phase, the mechanism of pore pressure diffusion during injection does not cause an increase of induced seismicity potential. On the other hand, model results for a non-critically stressed fault during depletion show a significant increase in the shear capacity utilization of the faults in the low permeability rocks. Though in the modelled scenario of a fault dip of 75º failure was not reached during injection, faults with more critical orientations could potentially be reactivated. In these cases injection could possibly initiate a first reactivation of the faults and result in injection-related seismicity. The last scenario has not been investigated in this study and needs a further analysis.

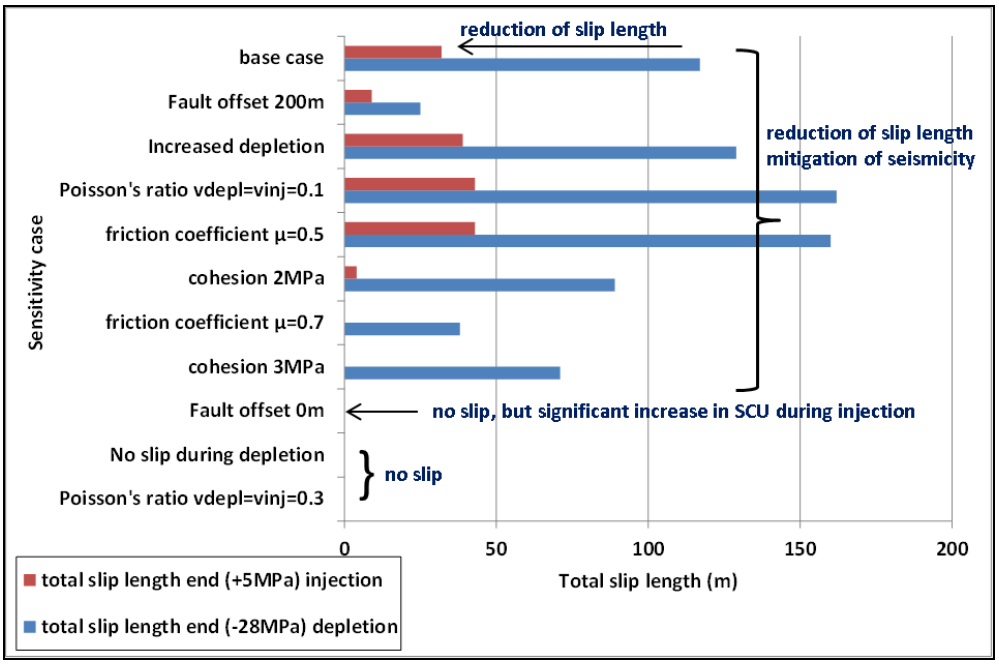

Figure 48: Total slip lengths at the end of 28 MPa deletion compared to total slip lengths at the end of 5 MPa injection. A decrease in total slip length is assumed indicative for a decrease of the seismicity potential of a fault, whereas an increase in total slip length is assumed indicative for an increase of the seismicity potential of a fault. Results are summarized for the scenarios of mechanism 2. Where no bars are presented, no slip occurred during depletion and/or injection.

Mechanism 3 (irreversibility of stress paths):
The gradients of the stress paths during injection and re-pressurization can be significantly smaller than during first-time depletion. Small stress path gradients during injection (which are related to small stress path coefficients for total horizontal stresses $\gamma_{h,inj}$) can have an adverse effect on the fault stability during injection. Different stress paths during depletion and injection can be a result of the elasto-plastic behaviour of the reservoir rocks during reservoir depletion (resulting in stress paths with large gradients) and a limited rebound during repressurization (resulting in stress paths with low gradients). The DIANA model used for analysis of this mechanism is similar to the DIANA model used for mechanism 2, but is extended with a different Poisson's ratio v_{inj} during the injection phase, to simulate

the effect of stress path irreversibility. The effect of small stress path gradients during injection on fault stability was modelled by increasing values for Poisson's ratio v_{inj} of the reservoir rocks. For the scenario of a fault with 75^0 dip and 100 m offset, modelling results show that during injection stress paths for v_{inj}=0.30 ($\gamma_{h,inj}$=0.57) result in a decrease of the total slip length during injection. Stress paths for v_{inj}=0.40 ($\gamma_{h,inj}$=0.33) and v_{inj}=0.48 ($\gamma_{h,inj}$=0.08) cause a continuation of fault slip and lead to a further growth of the total slip length (see Figure 49). For the scenario of v_{inj}=0.40 and v_{inj}=0.48, the increase in the slip length caused by a pressure increase of 5 MPa during injection is equal to, respectively larger than the increase in slip length that would occur during an ongoing depletion of 5 MPa without injection. Under the assumption that slip length can be used as a proxy for the induced seismicity potential during injection, it can be concluded that injection in case of stress path gradients related to v_{inj}=0.20 and v_{inj}=0.30 reduces the seismicity potential of the faults. Low stress path gradients related to v_{inj}=0.40 do not reduce the seismicity potential of the faults, and injection for v_{inj}=0.48 results in an increase of the seismicity potential compared to the scenario of ongoing depletion without injection.

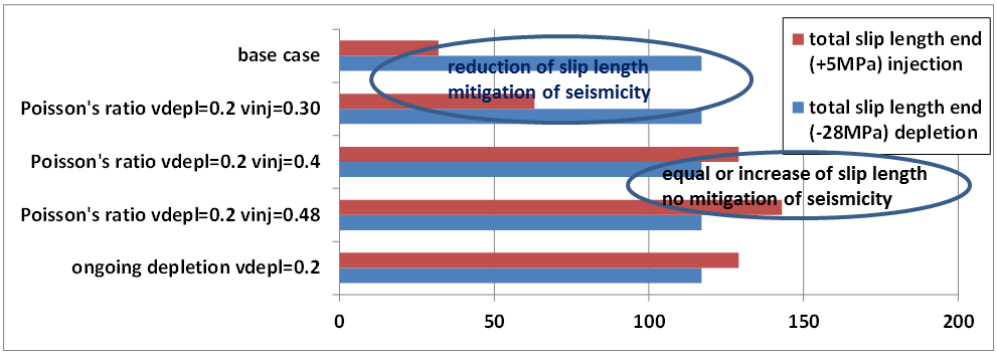

Figure 49: Four upper bars present the total slip lengths at the end of 28 MPa deletion compared to total slip lengths at the end of 5 MPa injection. Lowest bar presents the total slip length at the end of 28 MPa depletion and the total slip length at the end of ongoing depletion (33 MPa depletion). A decrease in total slip length is indicative for a decrease of the seismicity potential of a fault, whereas an increase in total slip length is indicative for an increase of the seismicity potential of a fault. Results are summarized for the scenarios of mechanism 2.

Mechanism 4 (cooling and thermal stresses):

The injection of nitrogen at injection temperatures lower than ambient reservoir temperatures causes a gradual cooling of the reservoir rocks in the vicinity of the injection wells. Cooling causes contraction of the reservoir rocks, which results in thermal stresses that can reach beyond the cooling-affected area. Model results show that for a single-well injection at a constant injection temperature of 10^0C, after an injection period of 20 years the cooling-affected area extends over a radial distance of 600 m from the injection well. Changes in normal effective stress and shear stress on the fault are localized, but large and can lead to the onset or the continuation of fault slip during the injection phase up to a radial distance of 500 m from the injection well. Comparison of the effects of pressure changes and temperature changes shows that the effect of a temperature drop of 1^0C on the shear capacity utilization (SCU) is much larger than the effect of 1 MPa pressure

increase on SCU, as stress paths due to temperature changes have a negative gradient and converge onto the Mohr Coulomb failure envelope much faster than stress paths for pressure changes (positive gradients). It is worth noting here that the assumption of a constant injection temperature of 10^0C during the entire injection period is at the more conservative end of the spectrum, since the temperature is expected to increase with time due to pressurization.

In summary, in most scenarios modelled injection has a positive effect on fault stability, as the total slip lengths decrease during injection. Of the four mechanisms identified, mechanism 3 (irreversible stress paths) and mechanism 4 (thermal effects) have the largest adverse effect on the stability of the faults during injection and the seismicity potential of a field. In addition, pore pressure diffusion into faults in low-permeability rocks, which are not yet critically stressed during depletion, can have a negative effect on the fault stability during injection. This latter scenario is recommended to be subject of further analysis.

Thermal effects on fault stability can be reduced by injecting nitrogen at temperatures close to ambient reservoir temperatures. The effect of stress path irreversibility (mechanism 3) strongly depends on the gradient of the stress path during re-pressurization and injection. Unfortunately, data on stress path coefficients during re-pressurization for Rotliegend reservoirs are limited. Stress path coefficients for unconsolidated sandstones as low as $\gamma_{h,inj}$=0 have been reported by Santarelli et al (1998). Nagelhout (1997) describe laboratory test results on Rotliegend reservoir rocks of the Norg underground gas storage field which indicate that 52% of the deformation during first-time loading cannot be recovered during unloading to initial conditions. Both observations indicate that a certain amount of stress path irreversibility is to be expected in the sandstone rocks. The absence of significant seismicity during the re-pressurization of the Bergermeer, Norg and Grijpskerk Rotliegend reservoirs on the other hand can be interpreted as an indication that at a field scale for Rotliegend sandstone reservoirs the effect of differences in stress path coefficients during production and injection on fault stability is limited (TNO-report 2015 R10906).

The following recommendations are given for follow-up studies:

- Little data is available on stress paths during re-pressurization. More data on material and reservoir-scale behavior during re-pressurization from experimental work and data from field observations and field tests is needed to assess the potential of injection-induced seismicity due to stress-path irreversibility.
- Slip lengths and slip displacements in this study are based on static models, using ideal plastic failure laws for the fault frictional behaviour. Dynamic rupture models which include both inertia forces and frictional weakening can be used to further quantify slip lengths, displacements and analyse the seismicity potential of the faults during injection. Dynamic models can be calibrated to observed seismicity, using data from downhole geophone arrays.
- A conservative scenario for injection at temperatures of 10 ºC has been used for modelling thermal effects. To further analyse the effect of thermal stresses on fault stability, additional models can be used which are based on temperature and pressure input from dynamic reservoir models, which take into account the effects of compression and expansion (Joule -Thomson effect) of

the gas on the spatial and temporal evolution of temperatures and pressures around the injection well.

- Further analysis of the effect of pressure diffusion into faults in low-permeability rocks, which are not yet critically stressed during depletion is needed.

7 References

DIANA User Manual. (2014). Release 9.6

Dake L.P. (1978). Fundamentals of reservoir engineering. Elsevier Science B.V., Amsterdam.

Ellsworth W.L. (2013). Injection-Induced Earthquakes. Science 341(6142).

Ghassemi A., Tarasovs S., Cheng A.H. (2007). A 3-D study of the effects of thermomechanical loads on fracture slip in enhanced geothermal reservoirs. International Journal of Rock Mechanics and Mining Sciences 44:1132.

Schlumberger (2014). ECLIPSE Reference Manual, version 2014.1, ECLIPSE Technical Description, version 2014.1.

Mulders F.M.M. (2003). Modelling of stress development and fault slip in and around a producing gas reservoir. Technical University of Delft.

Nagelhout A.C.G., Roest, J.P.A. (1997). Geomechanical modelling of the Norg gasfield.

Orlic B. Wassing B.B.T., Geel CR. (2013). Field Scale Geomechanical Modeling for Prediction of Fault Stability During Underground Gas Storage Operations in a Depleted Gas Field in the Netherlands.

Roest J.P.A. and Kuilman W. (1994). Geomechanical analysis of small earthquakes at the Eleveld gas reservoir.

TNO-report 2014 R11761 Literature review on Injection-Related Induced Seismicity and its relevance to Nitrogen Injection.

TNO-report 2015 R10906. Injection-Related Induced Seismicity and its relevance to Nitrogen Injection: Description of Dutch field cases.

TNO-report 2015 R10844 Modeling of dynamic fault rupture in a depleting gas field.

Santarelli F.J., Tronvoll J.T., Svennekjaer M., Skeie H., Henriksen R., Bratli R.K. (1998). Reservoir stress path: The depletion and the rebound. SPE/ISRM publication 47350.

Uenishi, K., & Rice, J.,R. (2003). Universal nucleation length for slip-weakening rupture instability under nonuniform fault loading. Journal of Geophysical Research, 108 (B1), 2042

Van den Bogert, P.A.J. (2015). Impact of various modelling options on the onset of fault slip and fault slip response using 2-dimensional Finite-Element modelling. Restricted Report No. SR.15.11455 Rijswijk: Shell Global Solutions International B.V.

A Appendix – Differential pressure evolution and effects of stress arching.

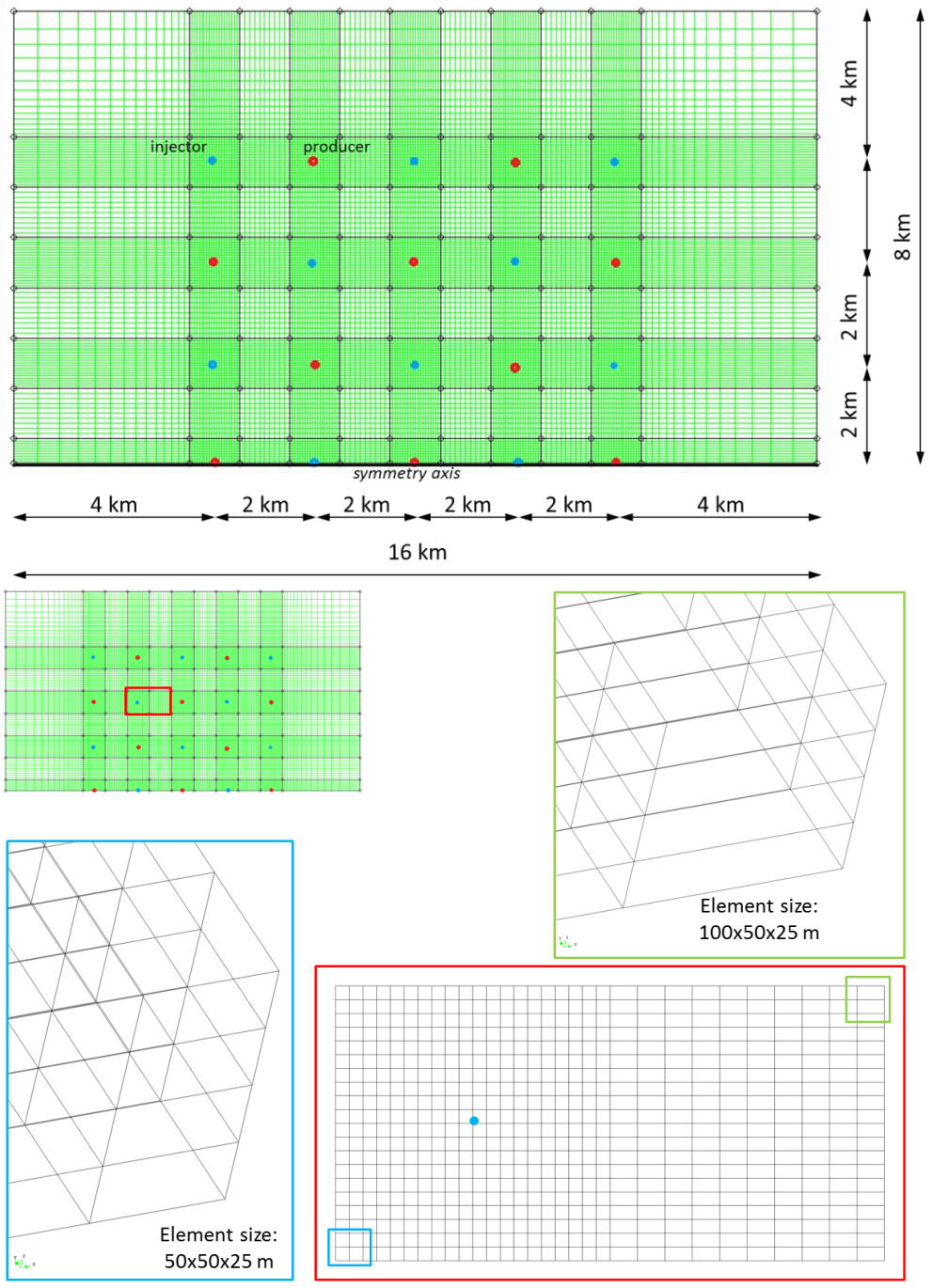

Figure A 1: Dimensions and mesh size for the 3D model, 4 km wavelength scenario.

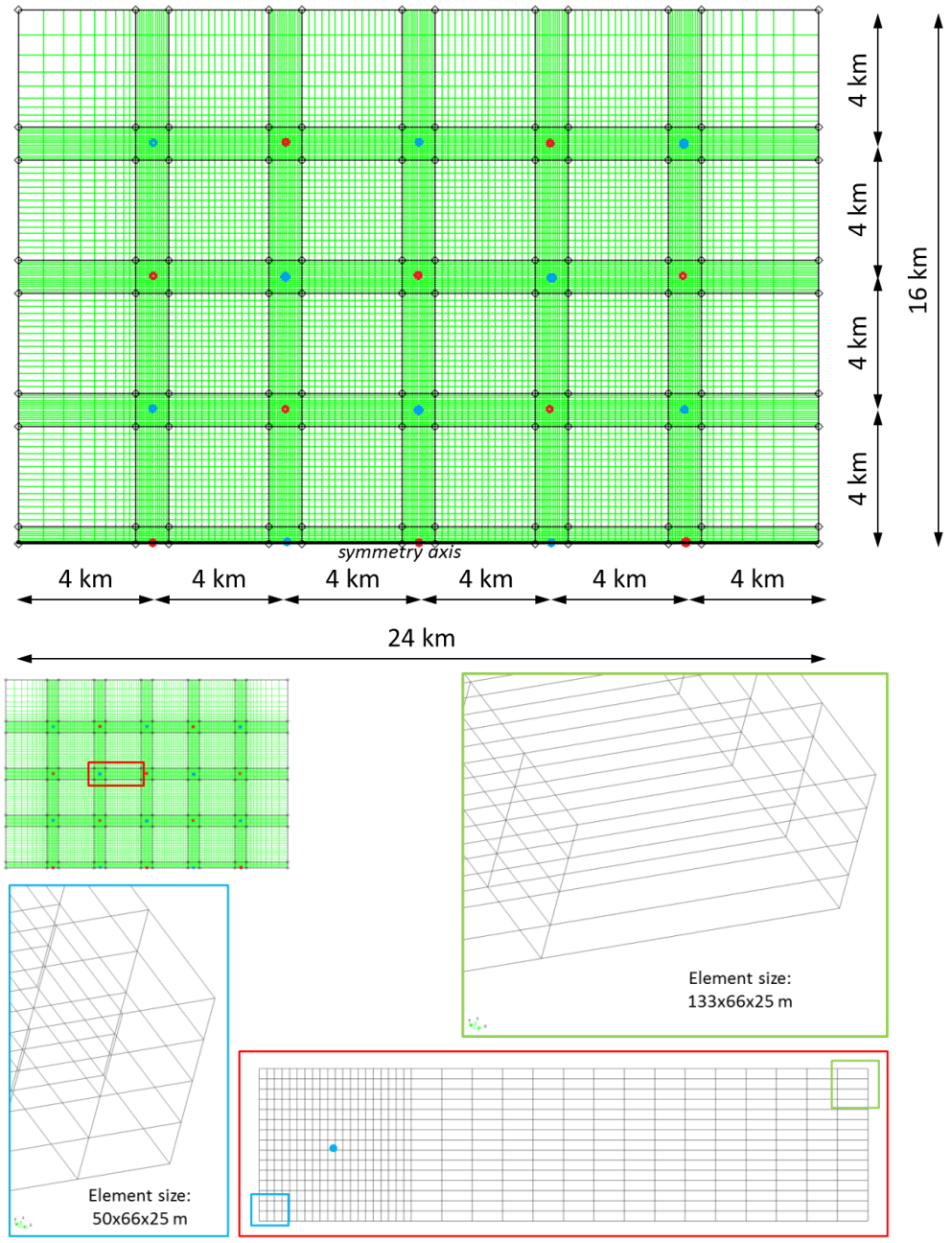

Figure A 2: Dimensions and mesh size for the 3D model, 8 km wavelength scenario.

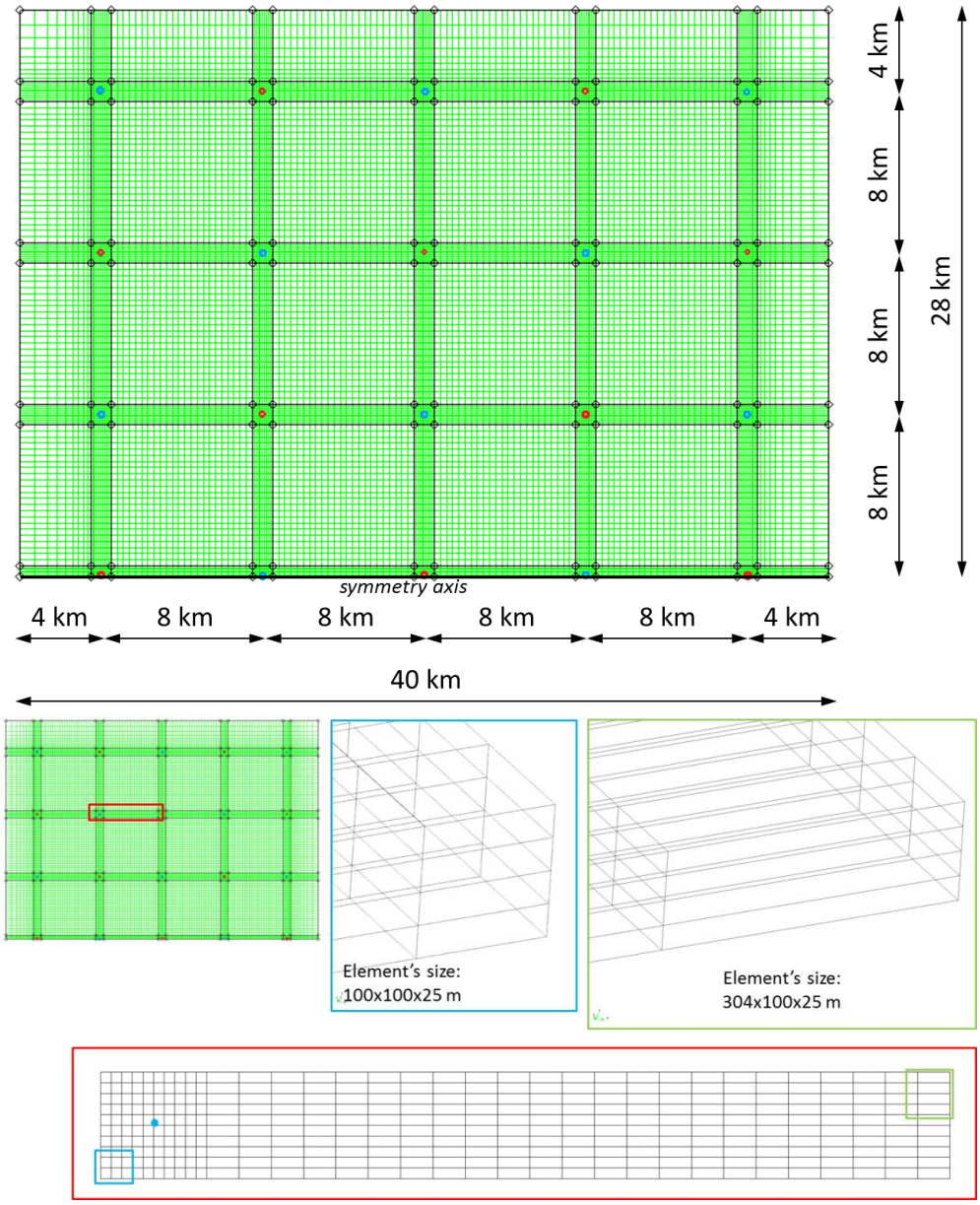

Figure A 3: Dimensions and mesh size for the 3D model, 8 km wavelength scenario.

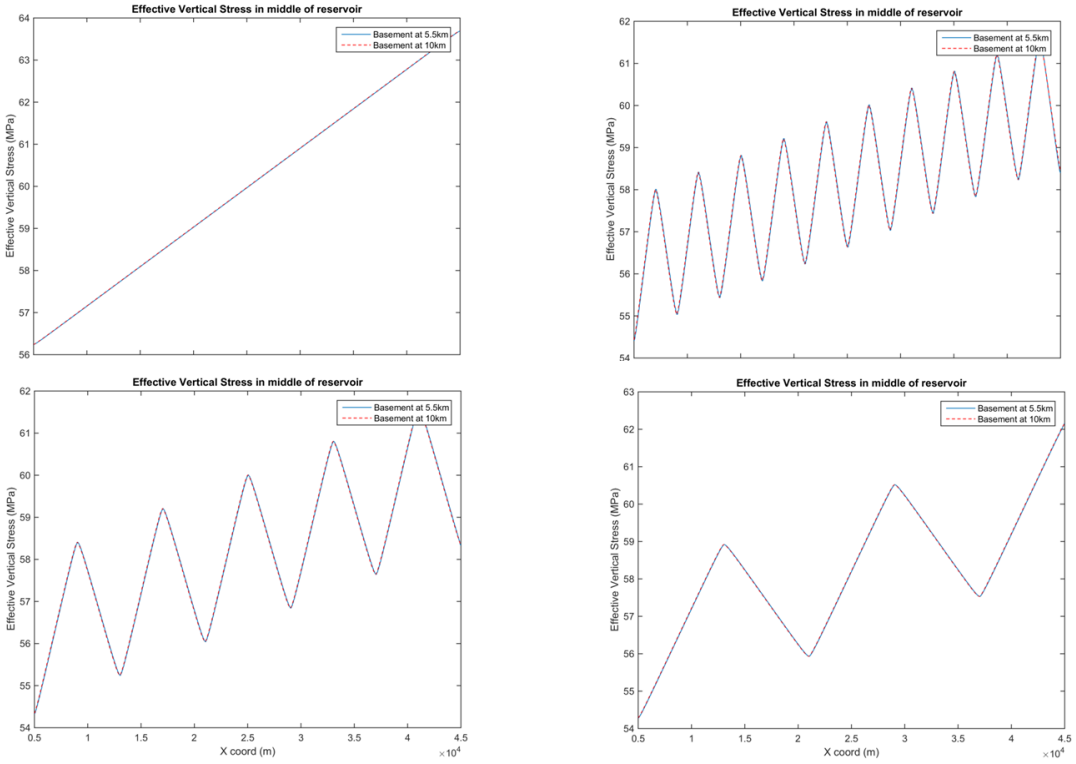

Figure A 4: Comparison of results computed with a 2D plane strain mesh with vertical dimensions of 5.5 and 10 km shows vertical mesh dimension has no effect on stresses calculated at reservoir level.

Results 2D plane strain model – changes in stress arching coefficients

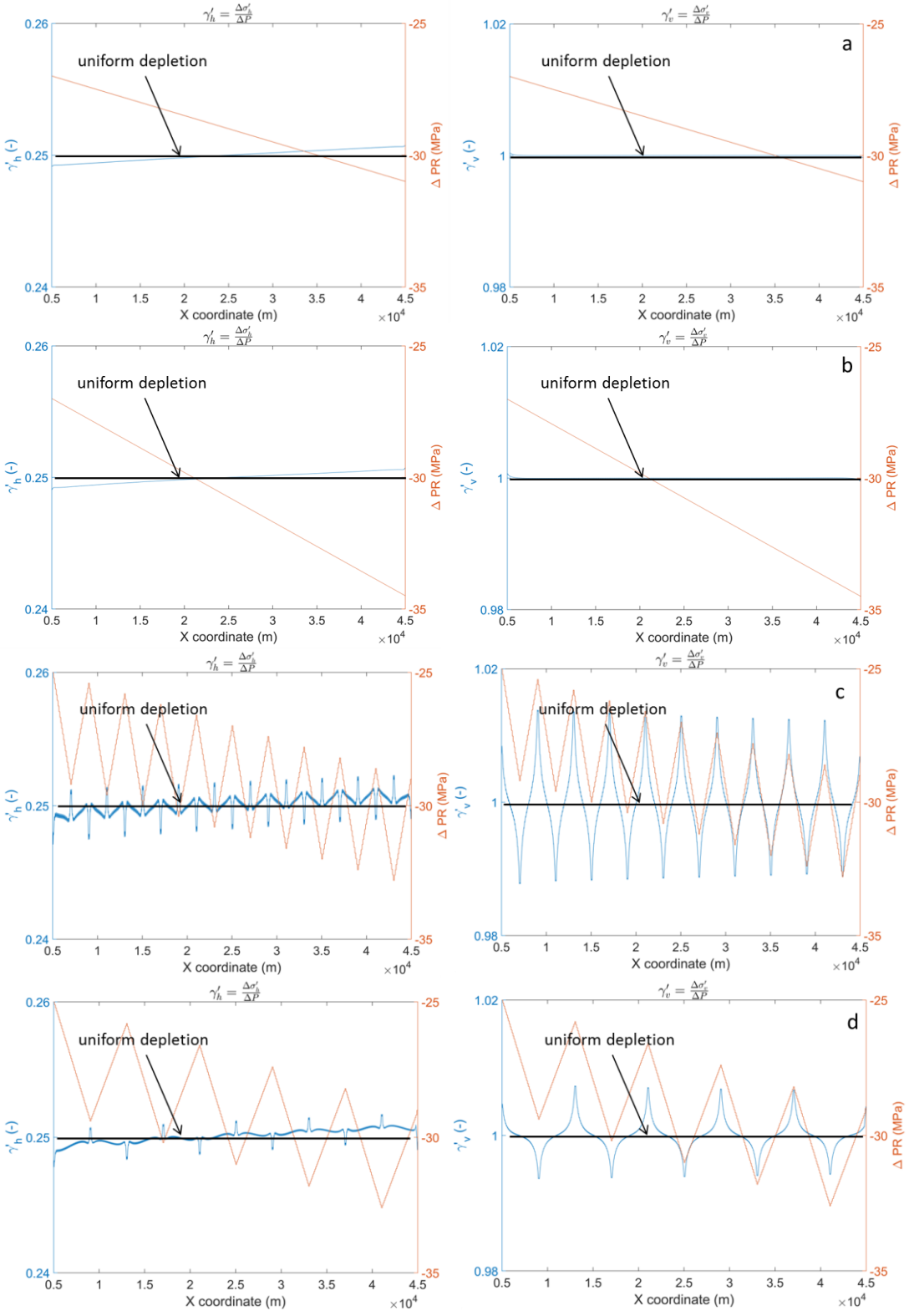

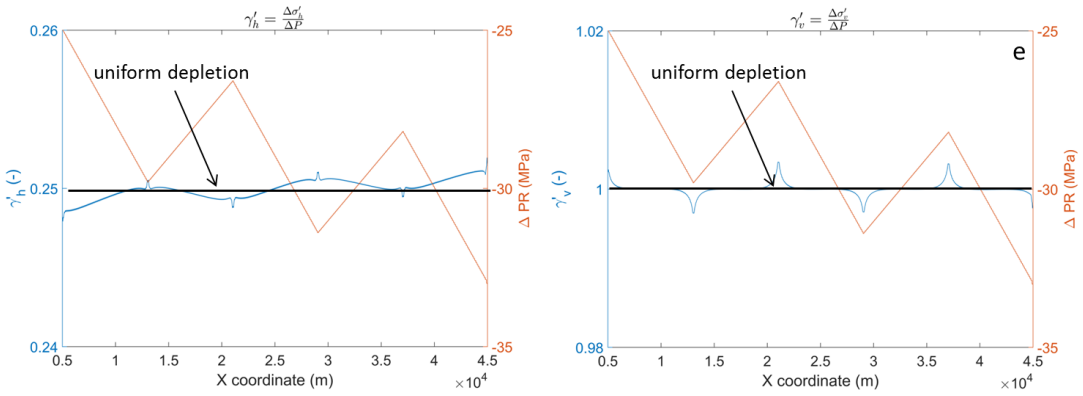

Figure A 5: Horizontal and vertical effective stress coefficients and pore pressures for a) linear depletion in scenario 1, b) linear depletion in scenario 2, c) zig-zag depletion, wavelength 4 km in scenario 3, d) zig-zag depletion, wavelength 8 km in scenario 4, e) zig-zag depletion, wavelength 16 km in scenario 5. Stress arching coefficients are presented as the blue line, pore pressures are presented as an orange line.

Results 3D model – changes in stress arching coefficients

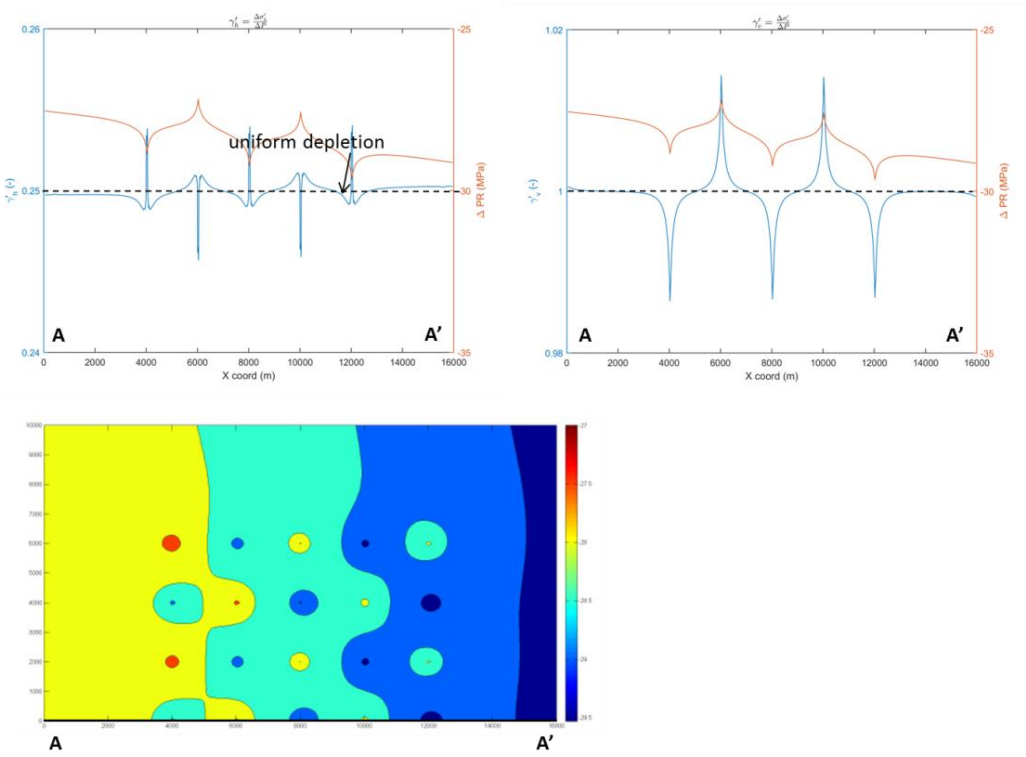

Figure A 6: Horizontal (upper left) and vertical effective stress (upper right) coefficients and pore pressures for zig-zag depletion, wavelength 4 km (scenario 3, 3D model). Stress arching coefficients are presented as the blue line, pore pressures are presented as an orange line. Contour plot at the bottom shows lateral spatial distribution of the pressures in the reservoir.

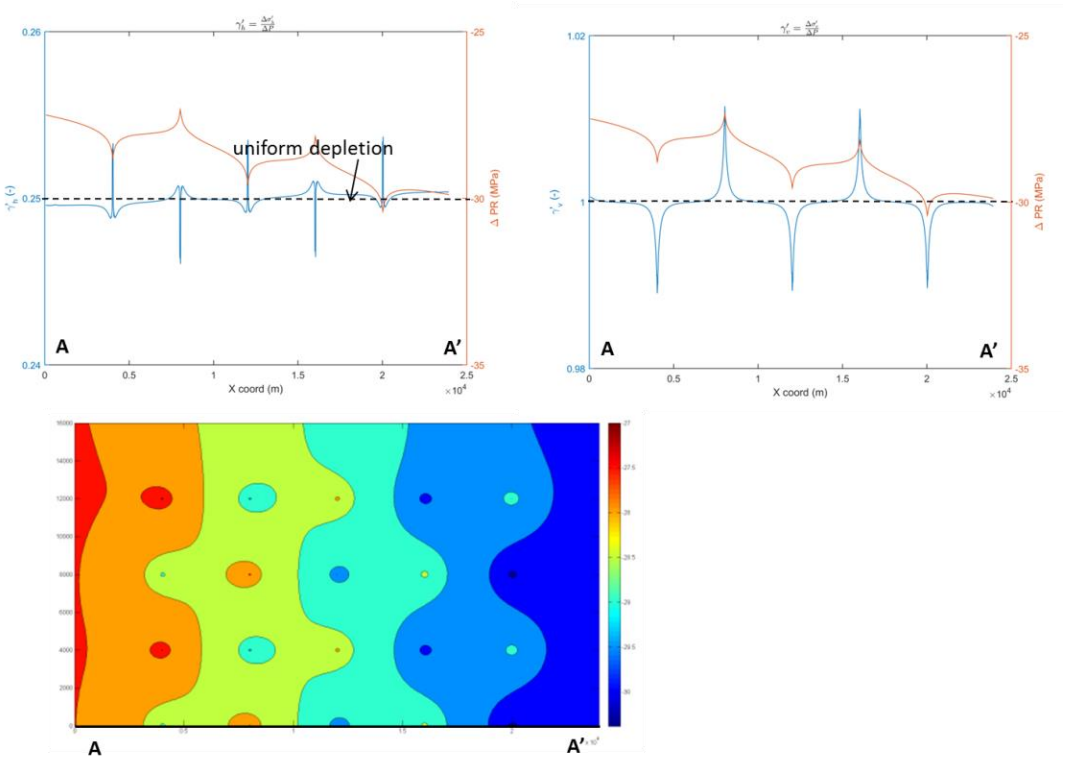

Figure A 7: Horizontal (upper left) and vertical effective stress (upper right) coefficients and pore pressures for zig-zag depletion, wavelength 8 km (scenario 4, 3D model). Stress arching coefficients are presented as the blue line, pore pressures are presented as an orange line. Contour plot at the bottom shows lateral spatial distribution of the pressures in the reservoir.

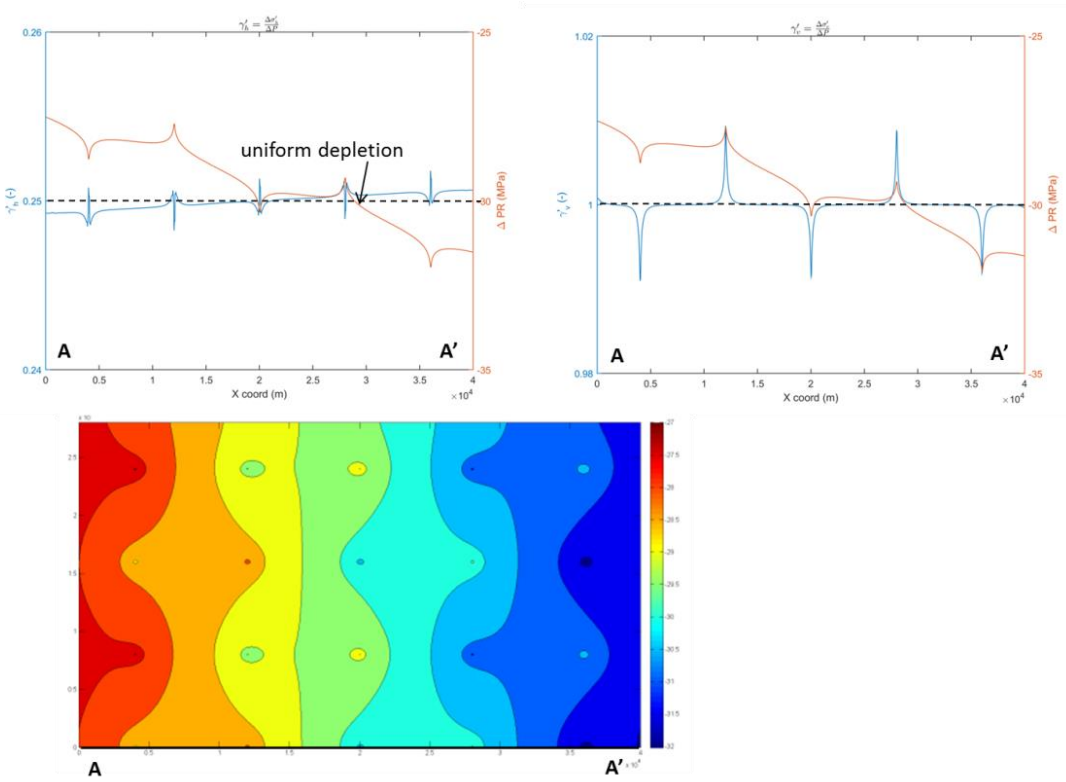

Figure A 8: Horizontal (upper left) and vertical effective stress (upper right) coefficients and pore pressures for zig-zag depletion, wavelength 16 km (scenario 5, 3D model). Stress arching coefficients are presented as the blue line, pore pressures are presented as an orange line. Contour plot at the bottom shows lateral spatial distribution of the pressures in the reservoir.

Results 2D plane strain model – changes in Shear capacity utilization

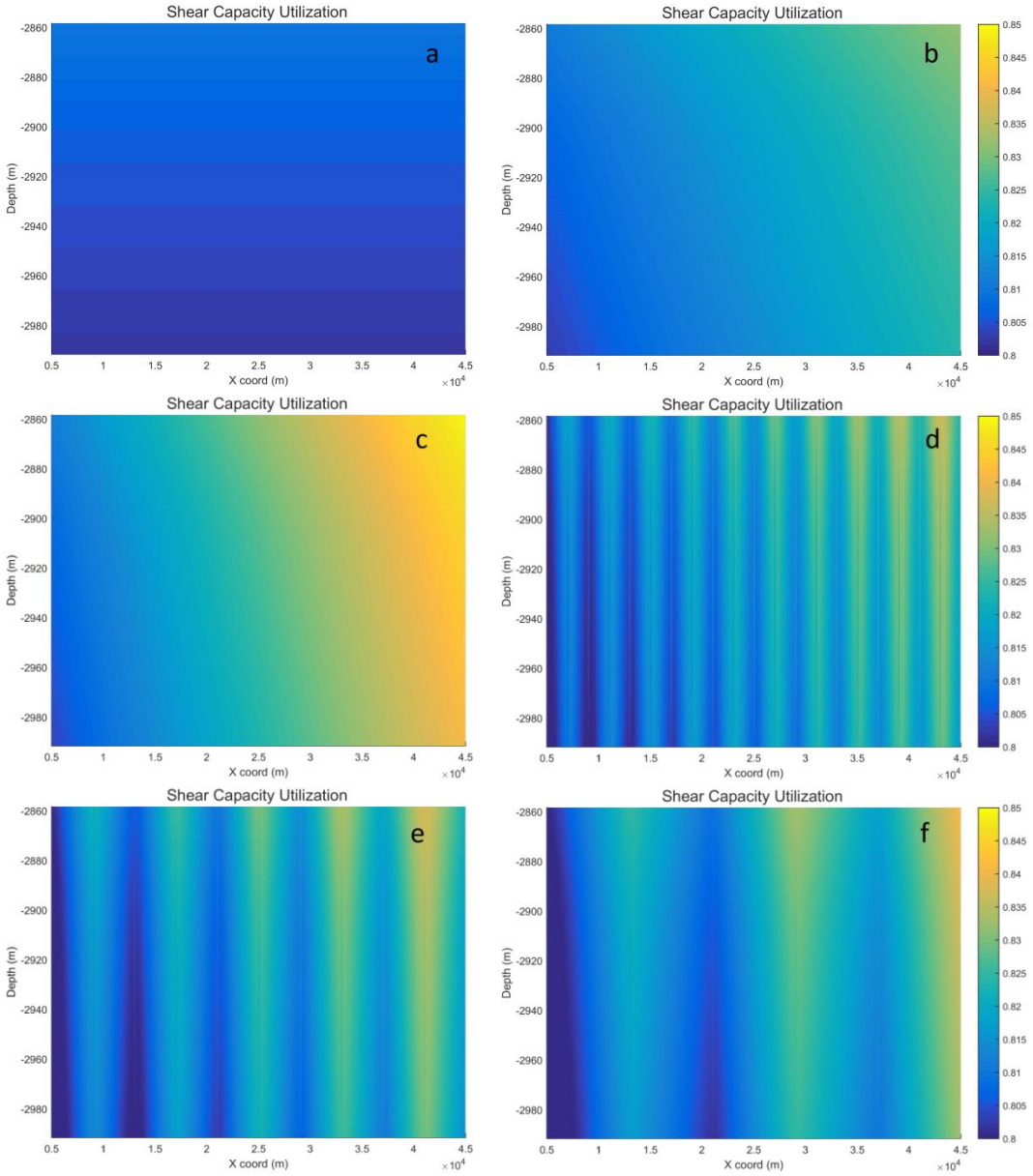

Figure A 9: Shear capacity utilization (SCU) computed for pressure a) uniform depletion from 35 MPa to 8 MPa, b) linear depletion in scenario 1, c) linear depletion in scenario 2, d) zig-zag depletion, wavelength 4 km in scenario 3, e) zig-zag depletion, wavelength 8 km in scenario 4, f) zig-zag depletion, wavelength 16 km in scenario 5.

B Appendix – Pore pressure diffusion into faults

Mechanisms 2 and 3: Base case

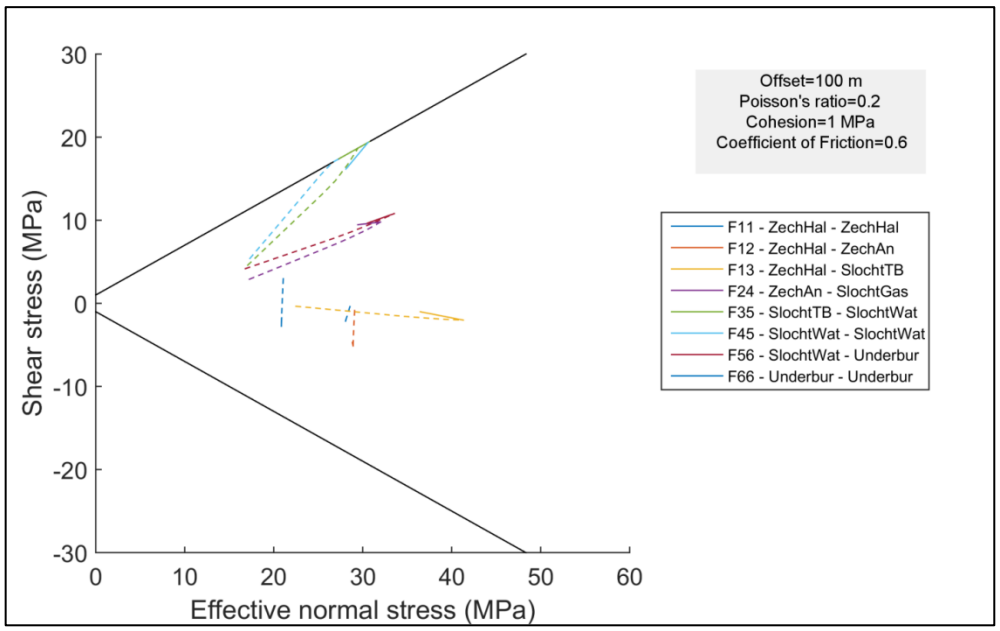

Figure B 1: Stress paths for the base case scenario of mechanism 2 and 3. Dashed lines present the stress paths during depletion, solid lines the stress paths during injection.

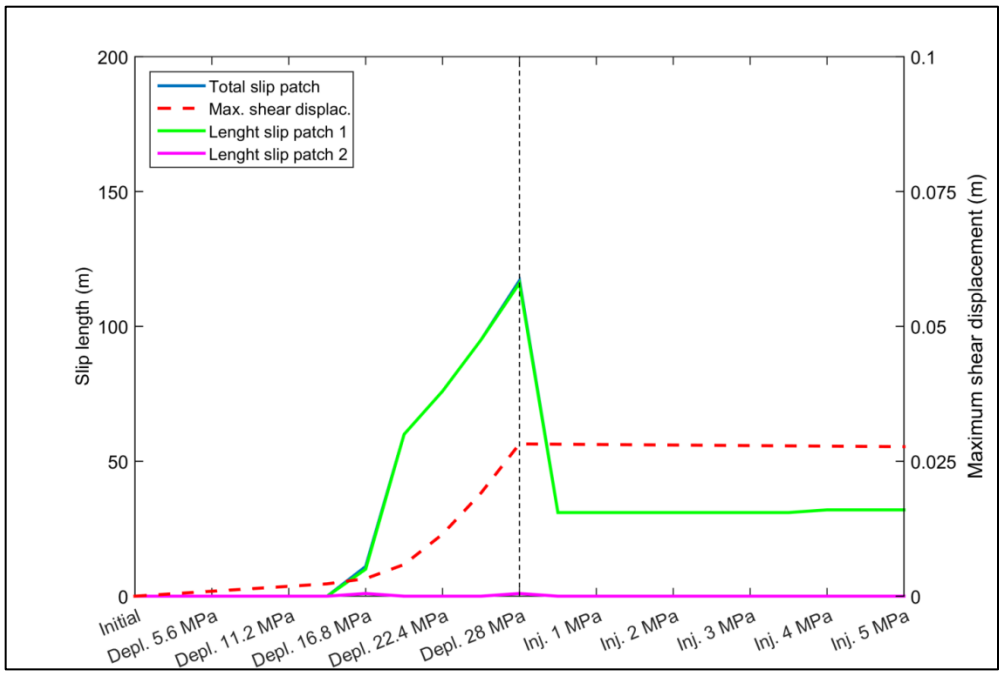

Figure B 2: Evolution of slip length and maximum relative shear displacement for the base case scenario.

Mechanisms 2 and 3: Base case

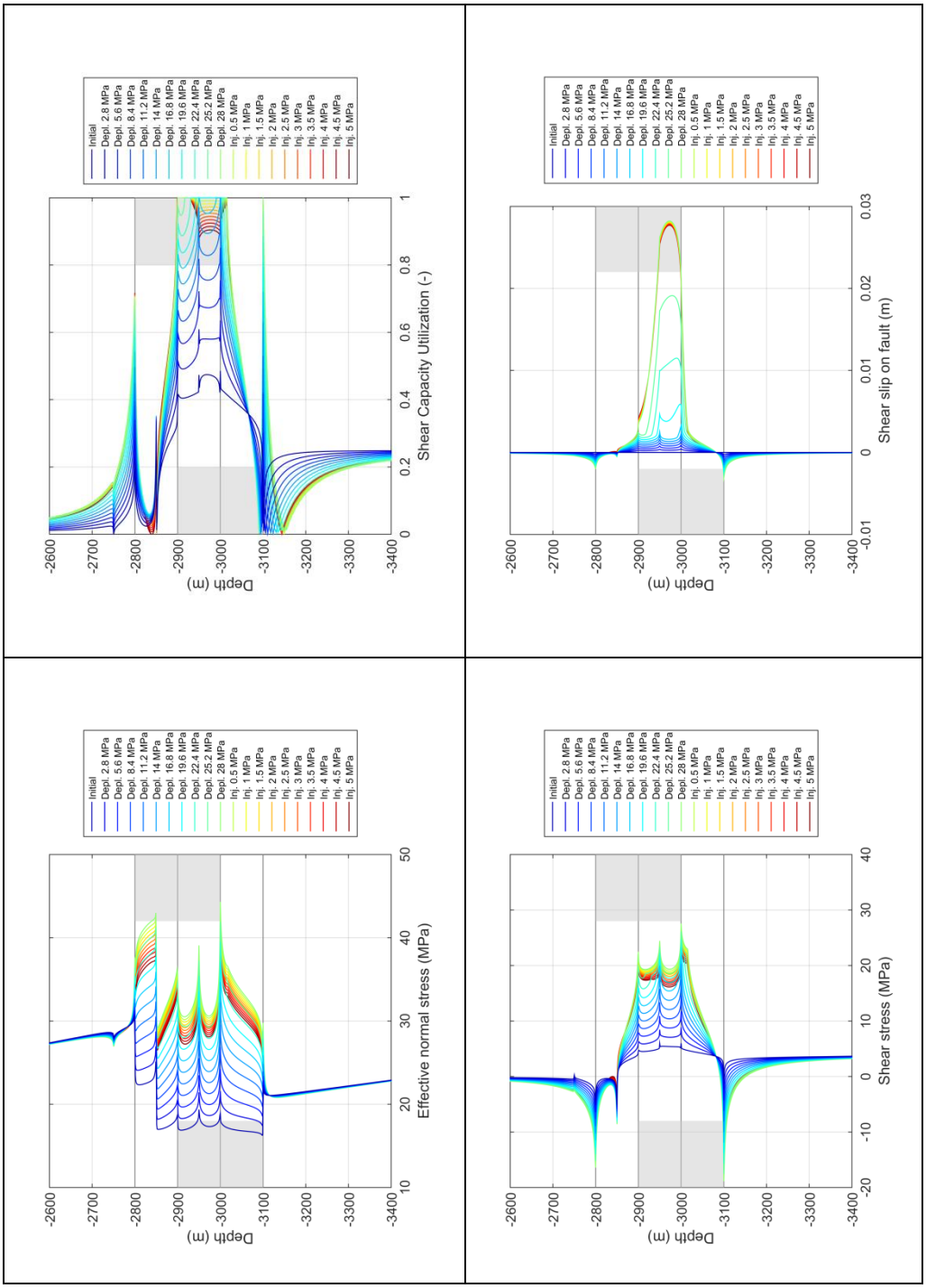

Figure B 3: Evolution of normal effective stress, shear capacity utilization (SCU), shear stress and fault slip (both elastic and plastic) during depletion and injection for the base case scenario.

Mechanisms 2 and 3: Base case

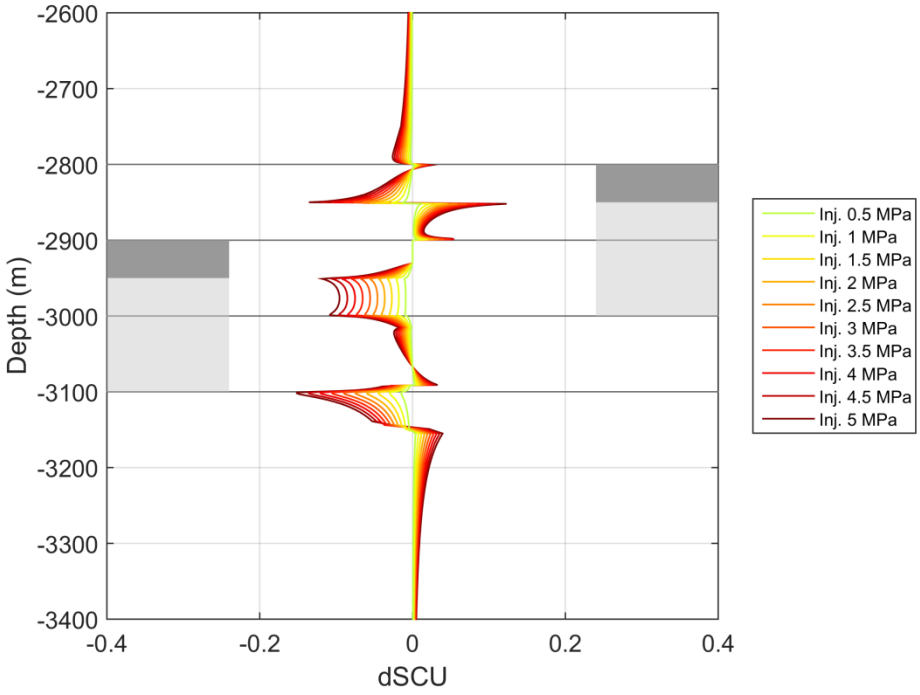

Figure B 4: Change in fault shear capacity utilization (dSCU) for the base case scenario.

Mechanism 2: Cohesion = 2 MPa

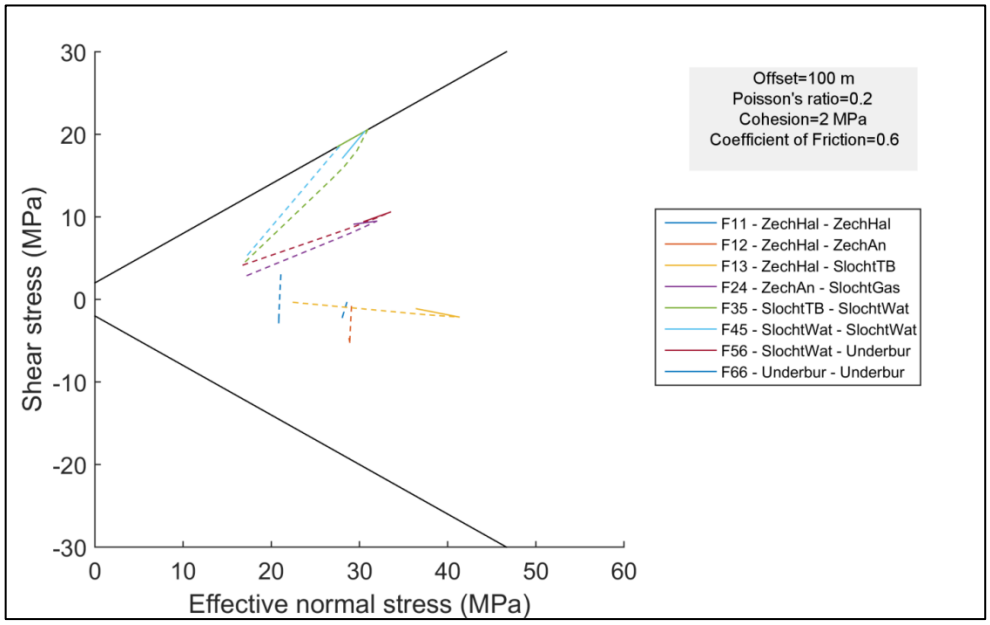

Figure B 5: Stress paths for the 2 MPa cohesion scenario of mechanism 2. Dashed lines present the stress paths during depletion, solid lines the stress paths during injection.

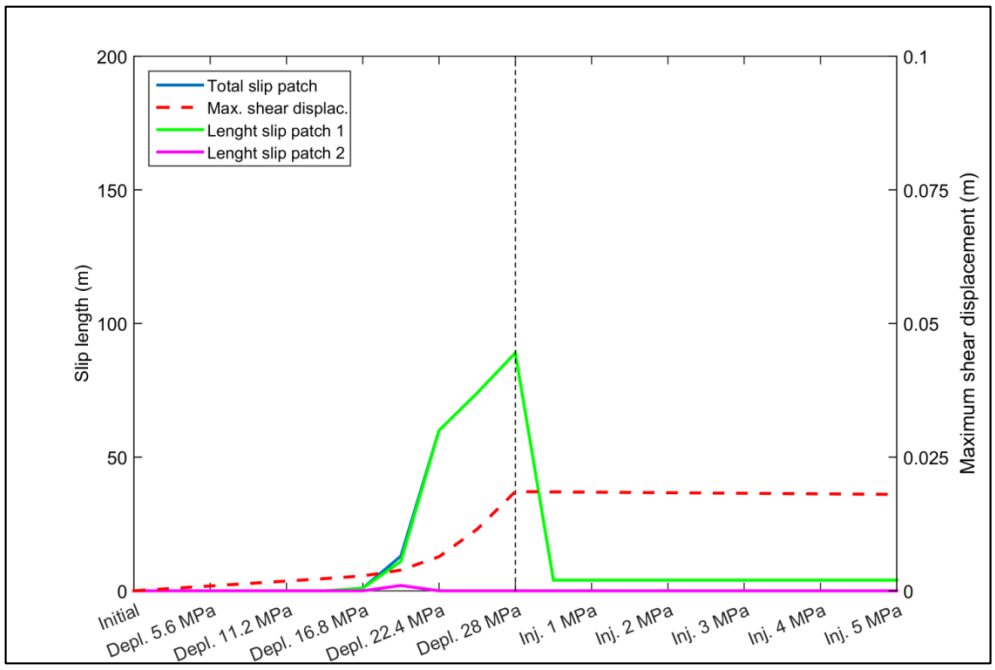

Figure B 6: Evolution of slip length and maximum relative shear displacement for the 2 MPa cohesion scenario.

Mechanism 2: Cohesion = 2 MPa

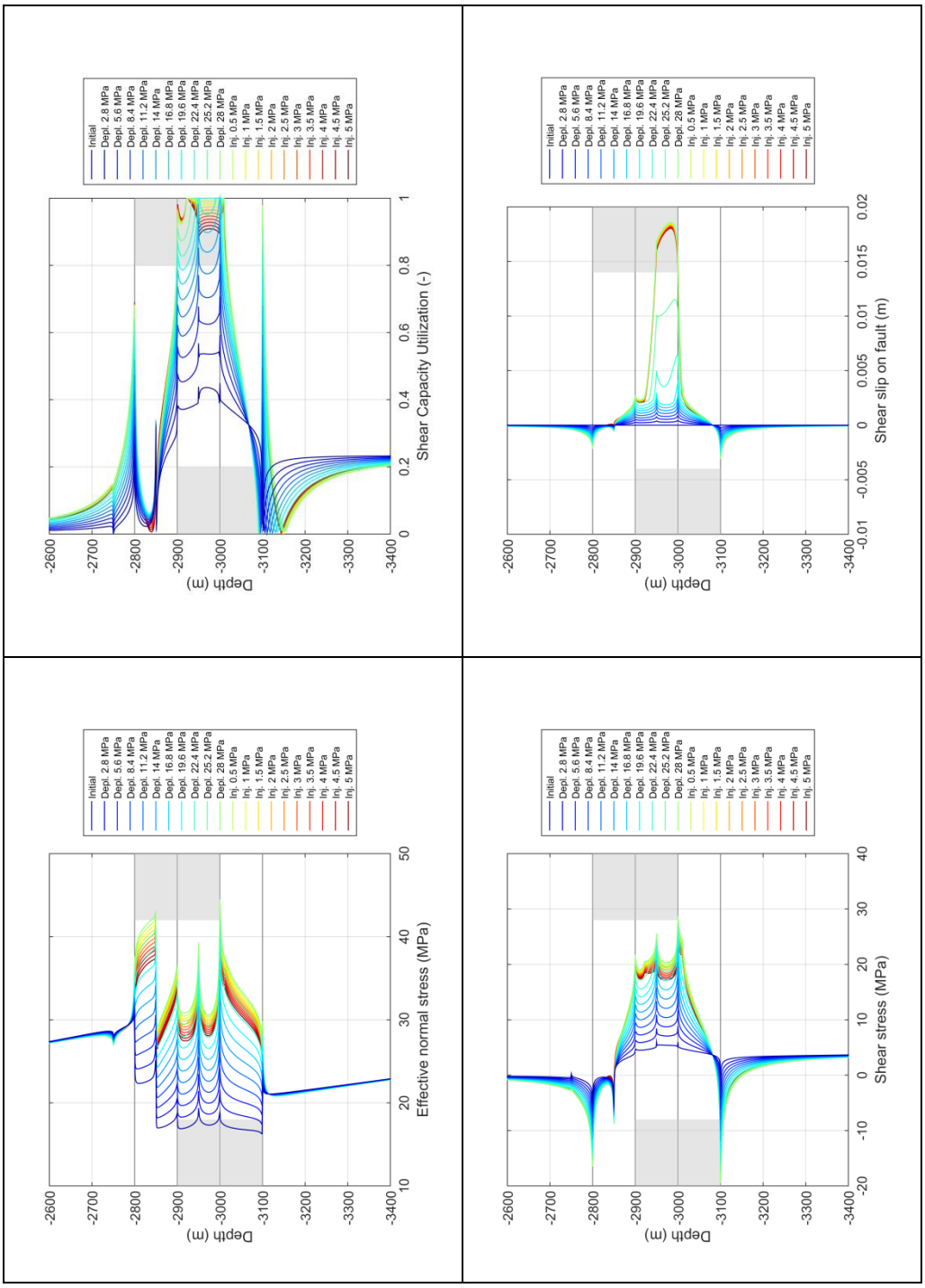

Figure B 7: Evolution of normal effective stress, shear capacity utilization (SCU), shear stress and fault slip (both elastic and plastic) during depletion and injection for the 2 MPa cohesion scenario.

Mechanism 2: Cohesion = 3 MPa

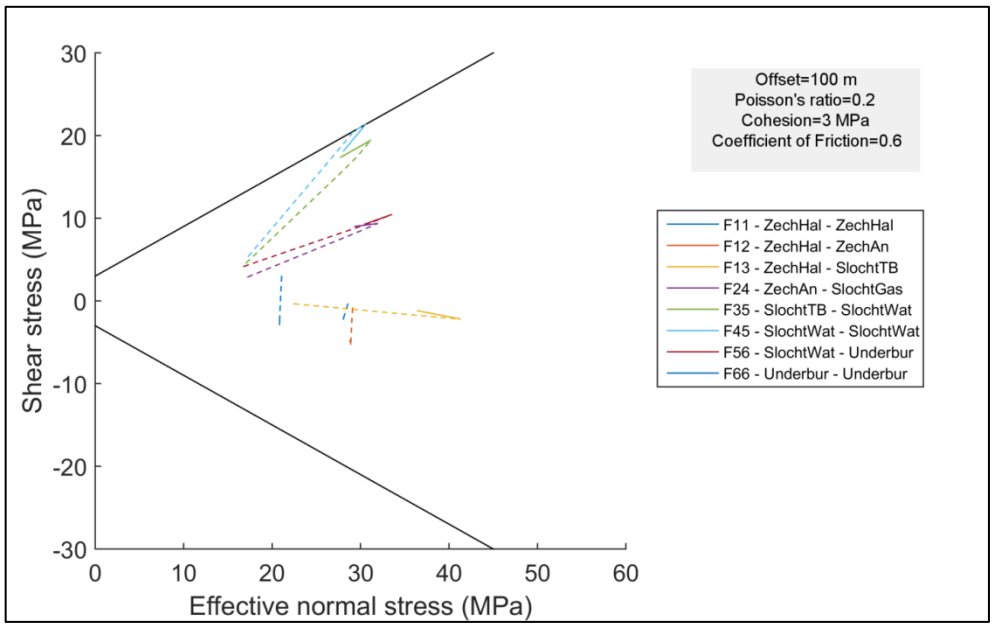

Figure B 8: Stress paths for the 3 MPa cohesion scenario of mechanism 2. Dashed lines present the stress paths during depletion, solid lines the stress paths during injection.

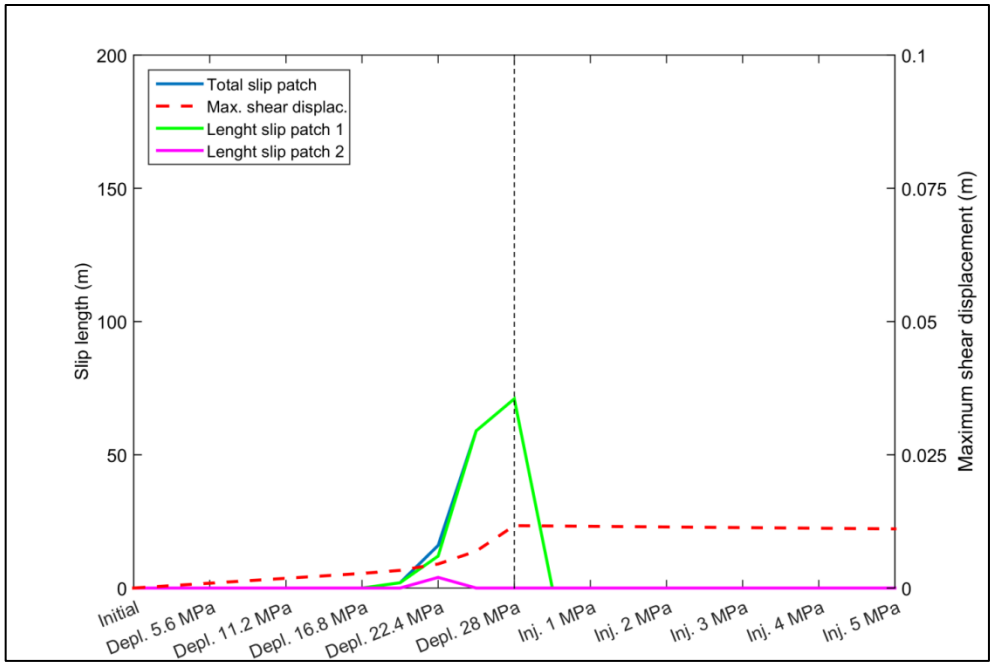

Figure B 9: Evolution of slip length and maximum relative shear displacement for the 3 MPa cohesion scenario.

Mechanism 2: Cohesion = 3 MPa

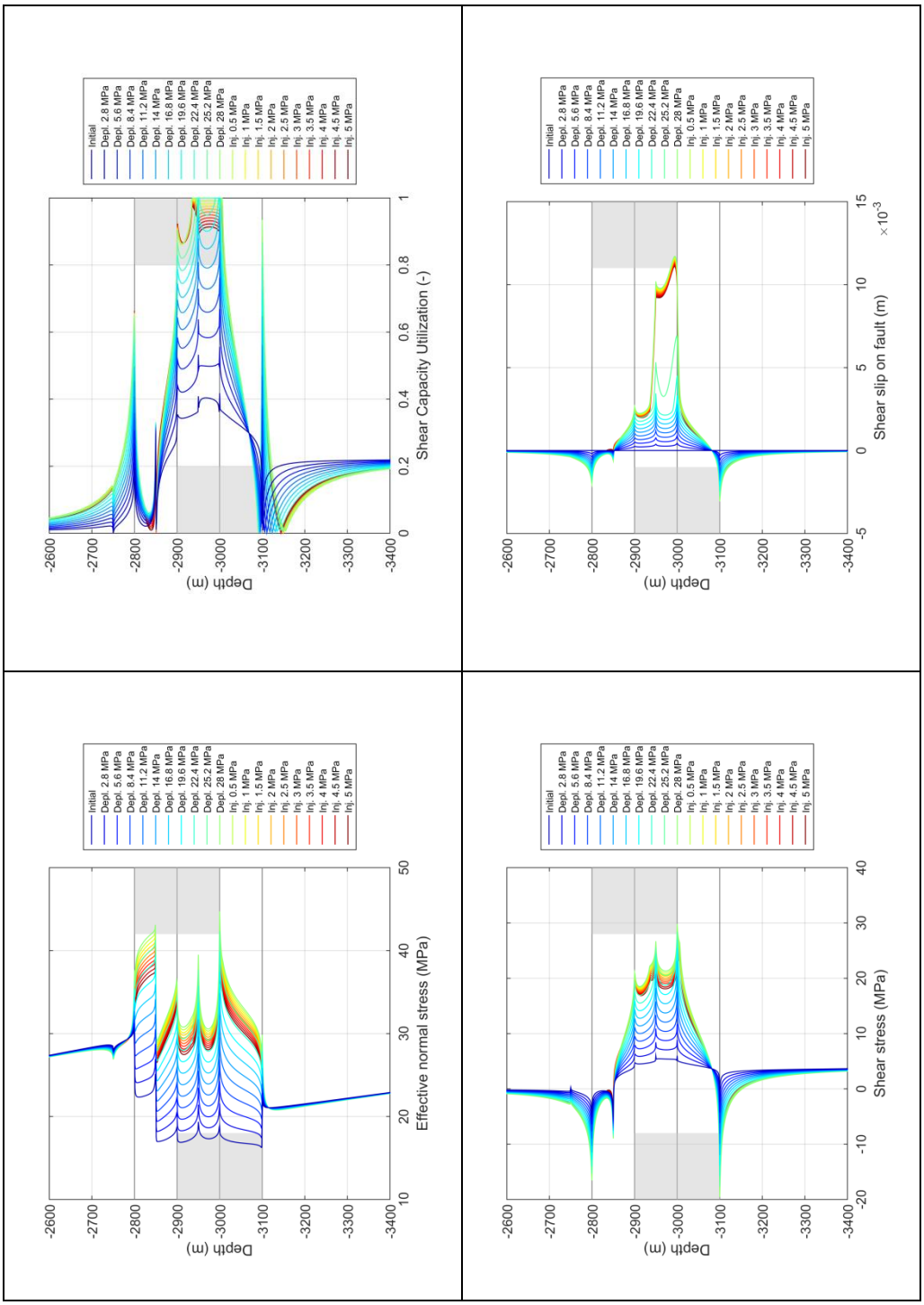

Figure B 10: Evolution of normal effective stress, shear capacity utilization (SCU), shear stress and fault slip (both elastic and plastic) during depletion and injection for the 3 MPa cohesion scenario.

Mechanism 2: μ = 0.5

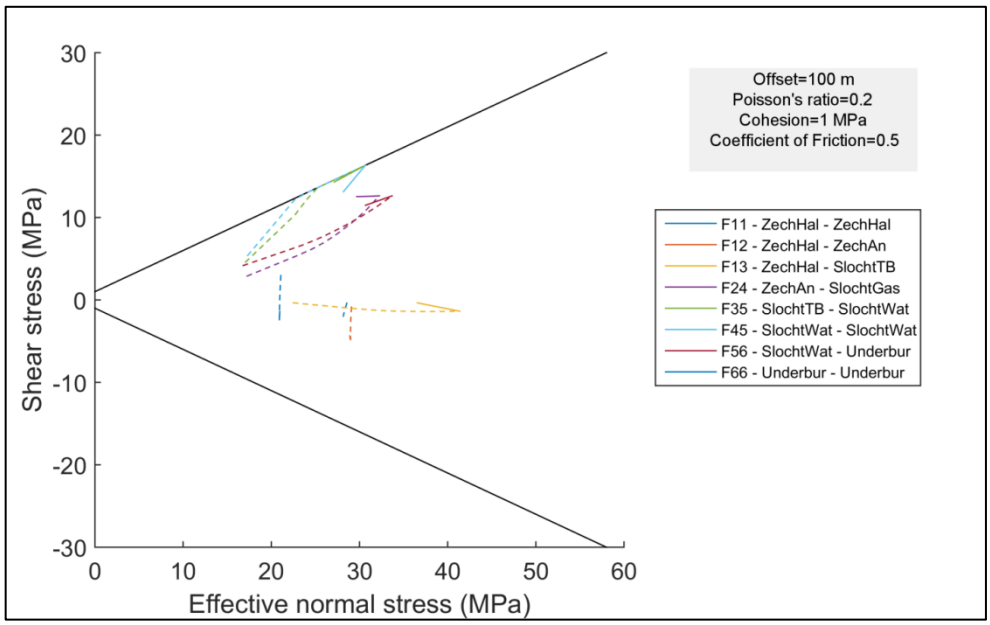

Figure B 11: Stress paths for the scenario of mechanism 2 with friction coefficient 0.5. Dashed lines present the stress paths during depletion, solid lines the stress paths during injection.

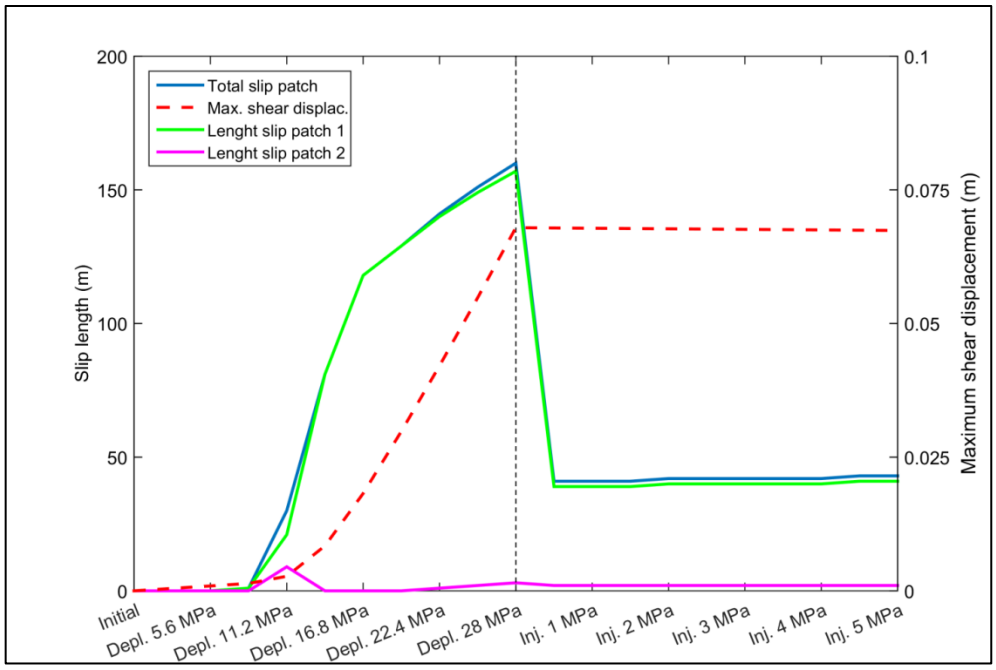

Figure B 12: Evolution of slip length and maximum shear displacement for the scenario of mechanism 2 with μ=0.5.

Mechanism 2: μ = 0.5

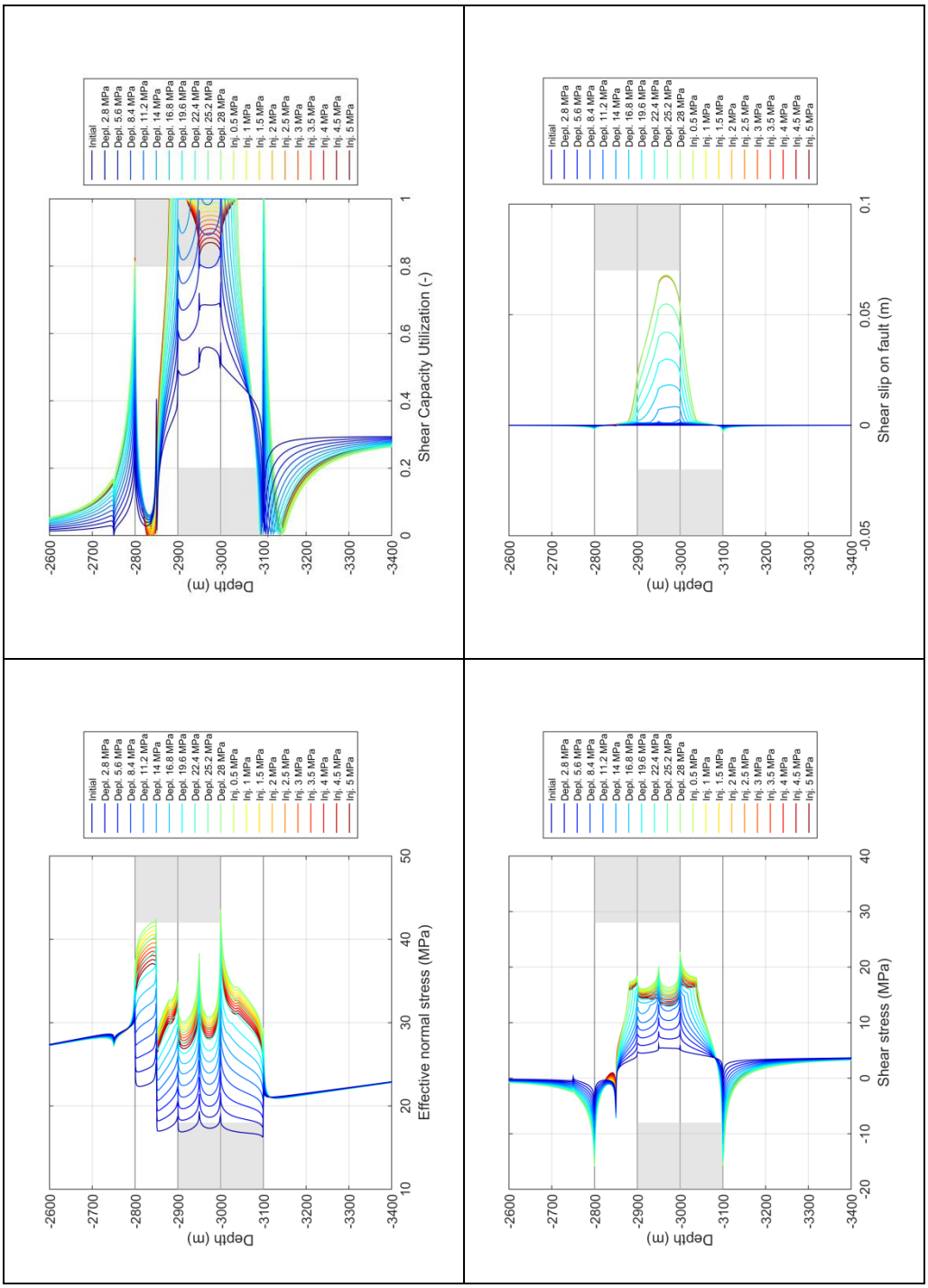

Figure B 13: Evolution of normal effective stress, shear capacity utilization (SCU), shear stress and fault slip (both elastic and plastic) during depletion and injection for the scenario of mechanism 2 with μ=0.5.

Mechanism 2: μ = 0.7

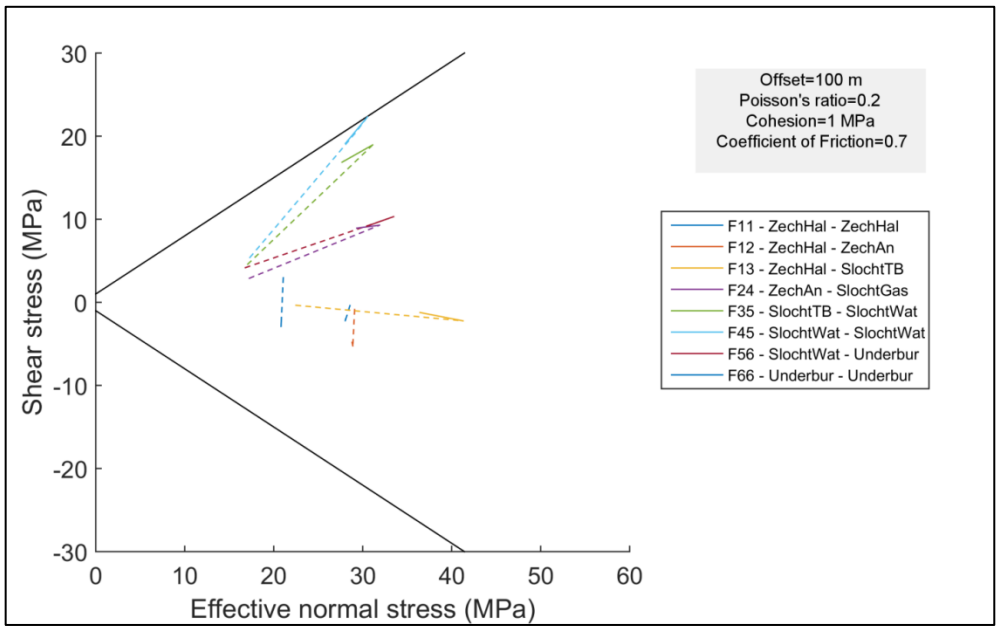

Figure B 14: Stress paths for the scenario of mechanism 2 with μ=0.7. Dashed lines present the stress paths during depletion, solid lines the stress paths during injection.

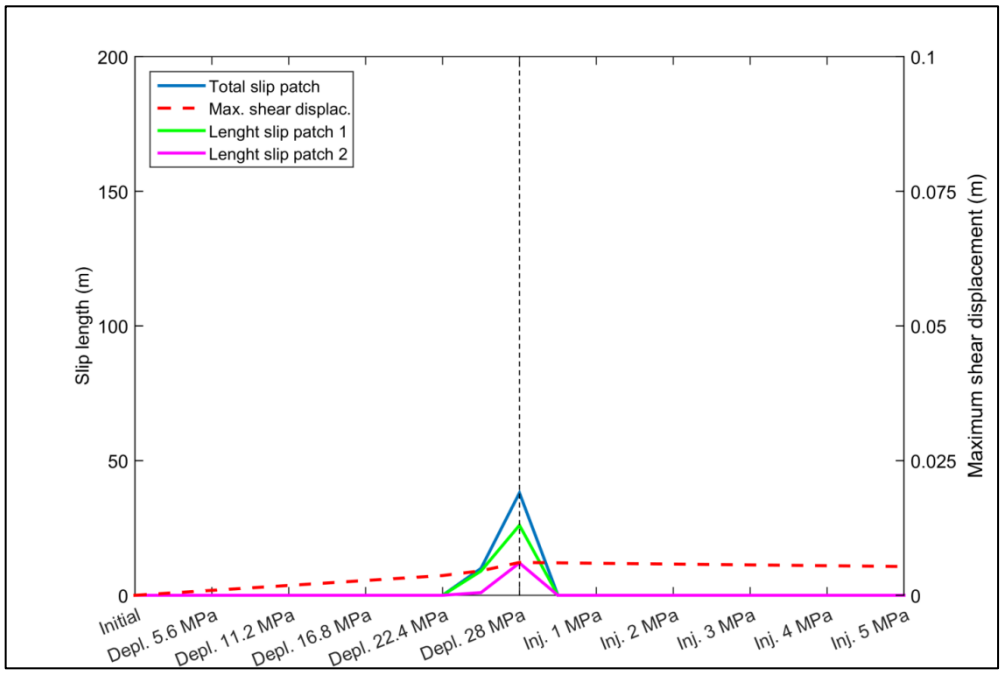

Figure B 15: Evolution of slip length and maximum relative shear displacement for the scenario of mechanism 2 with μ=0.7.

Mechanism 2: μ = 0.7

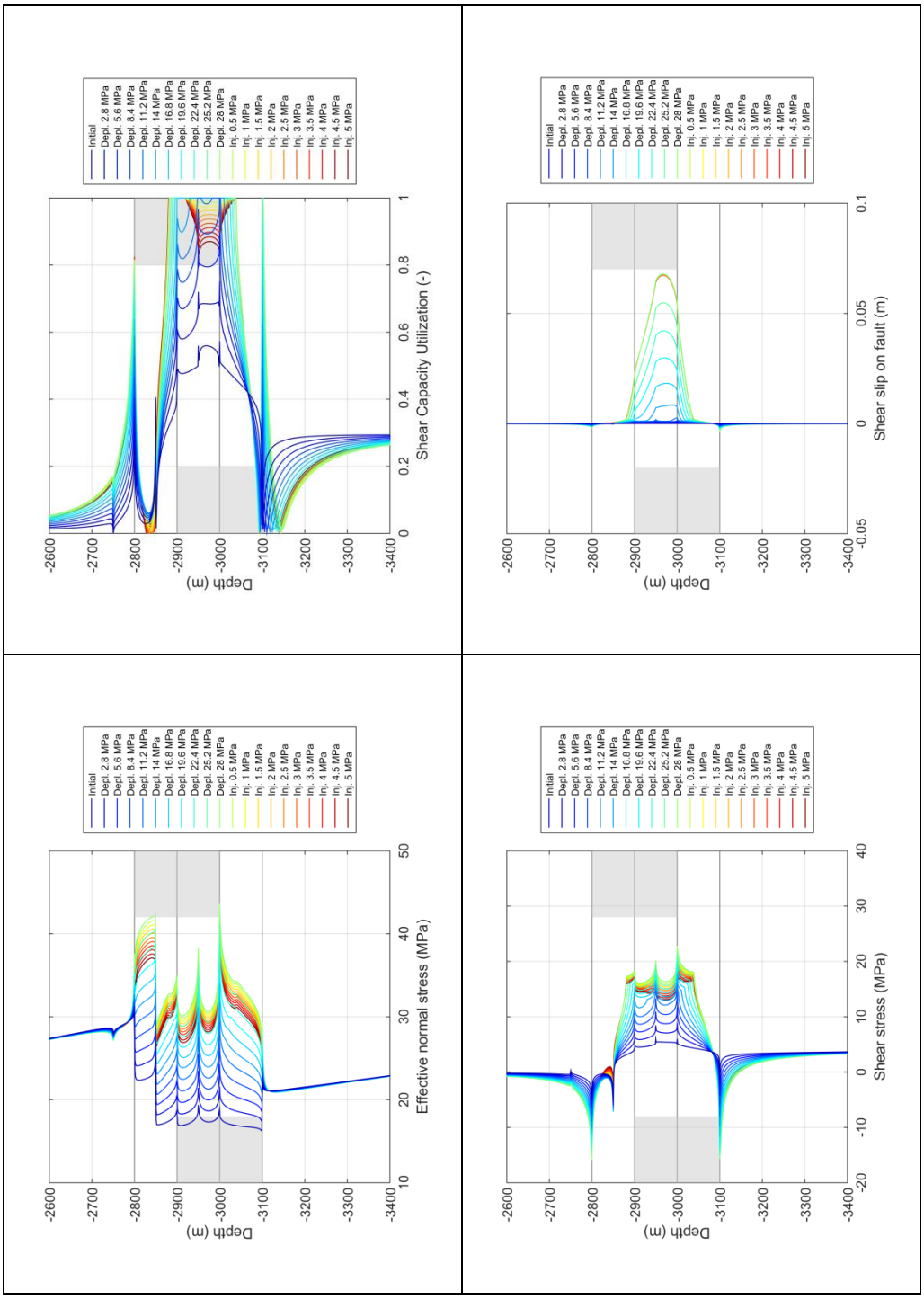

Figure B 16: Evolution of normal effective stress, shear capacity utilization (SCU), shear stress and fault slip (both elastic and plastic) during depletion and injection for the scenario of mechanism 2 with μ=0.

Mechanism 2: Change in shear capacity for cohesion 2 MPa and 3 MPa and friction coefficient μ = 0.5 and μ = 0.7

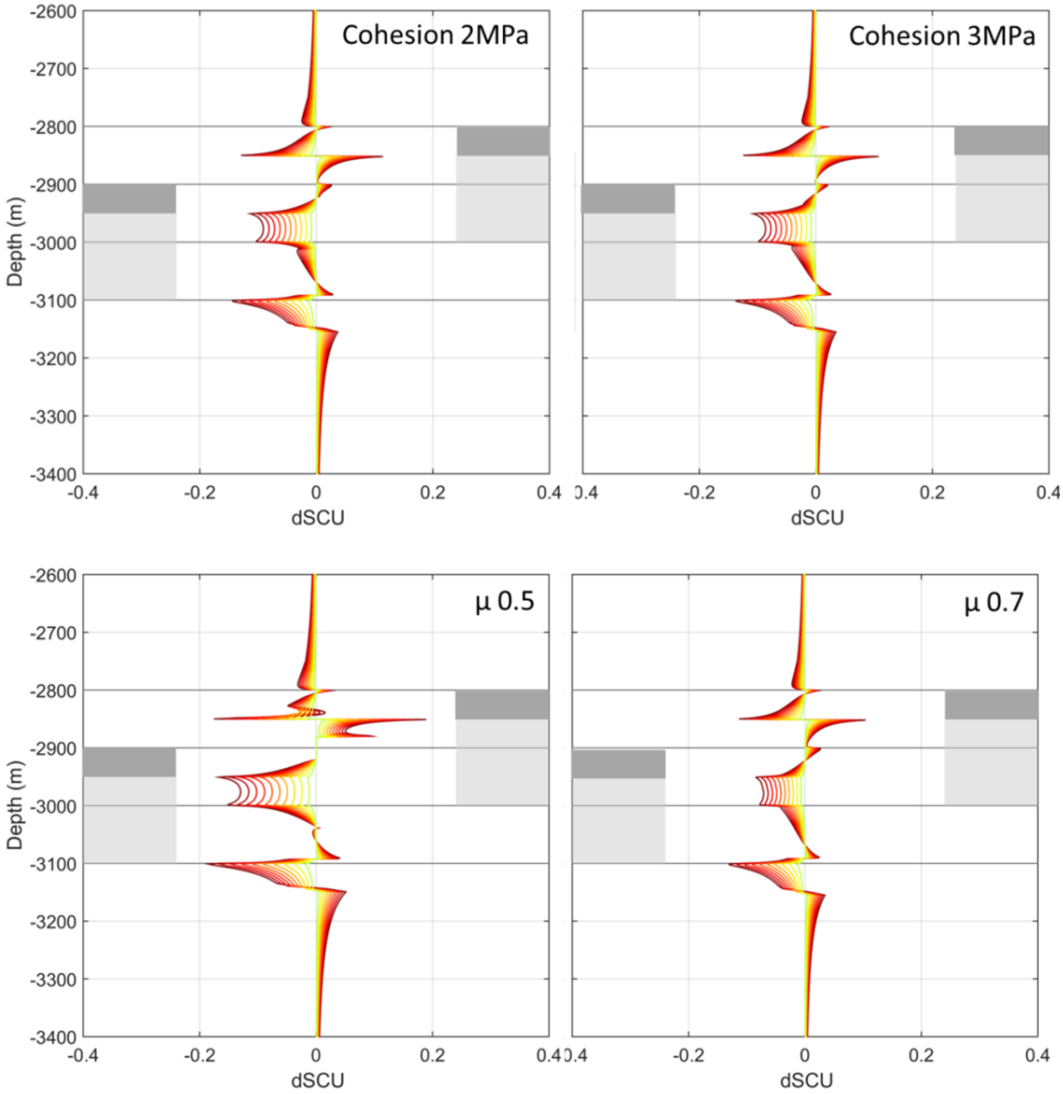

Figure B 17: Change in fault shear capacity utilization (dSCU) for different cohesion and friction coefficient values for the fault. Change in shear capacity utilization for cohesion 2 MPa and 3 MPa and μ=0.7 are very similar to dSCU for the base case (Figure B4), whereas dSCU for μ=0.5 is different due to the large amount of fault slip and redistribution of stresses around the area of fault slip.

Mechanism 2: Poisson's ratio *v* = 0.1

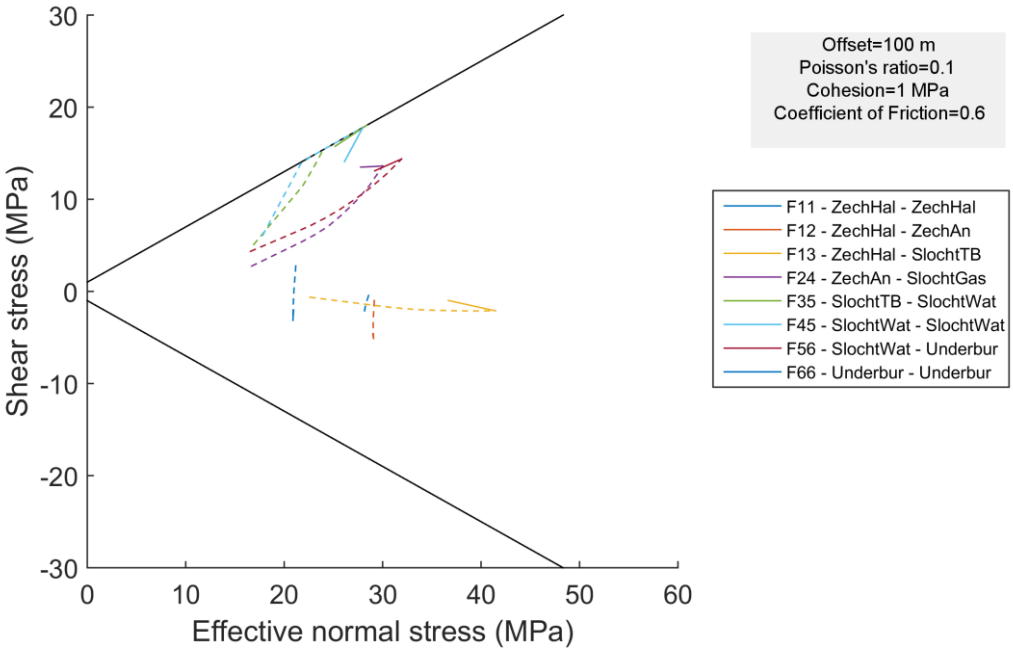

Figure B 18: Stress paths for scenario of mechanism 2 with Poisson's ratio value of 0.1. Dashed lines present the stress paths during depletion, solid lines the stress paths during injection.

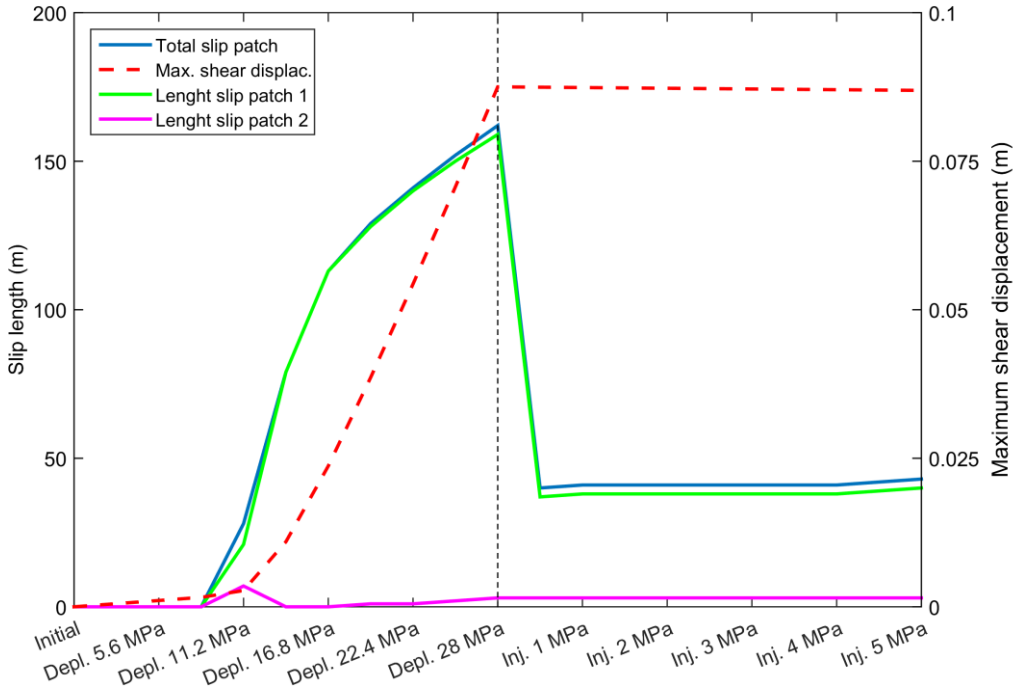

Figure B 19: Evolution of slip length and maximum relative shear displacement for scenario of mechanism 2 with Poisson's ratio value of 0.1.

Mechanism 2: v = 0.1

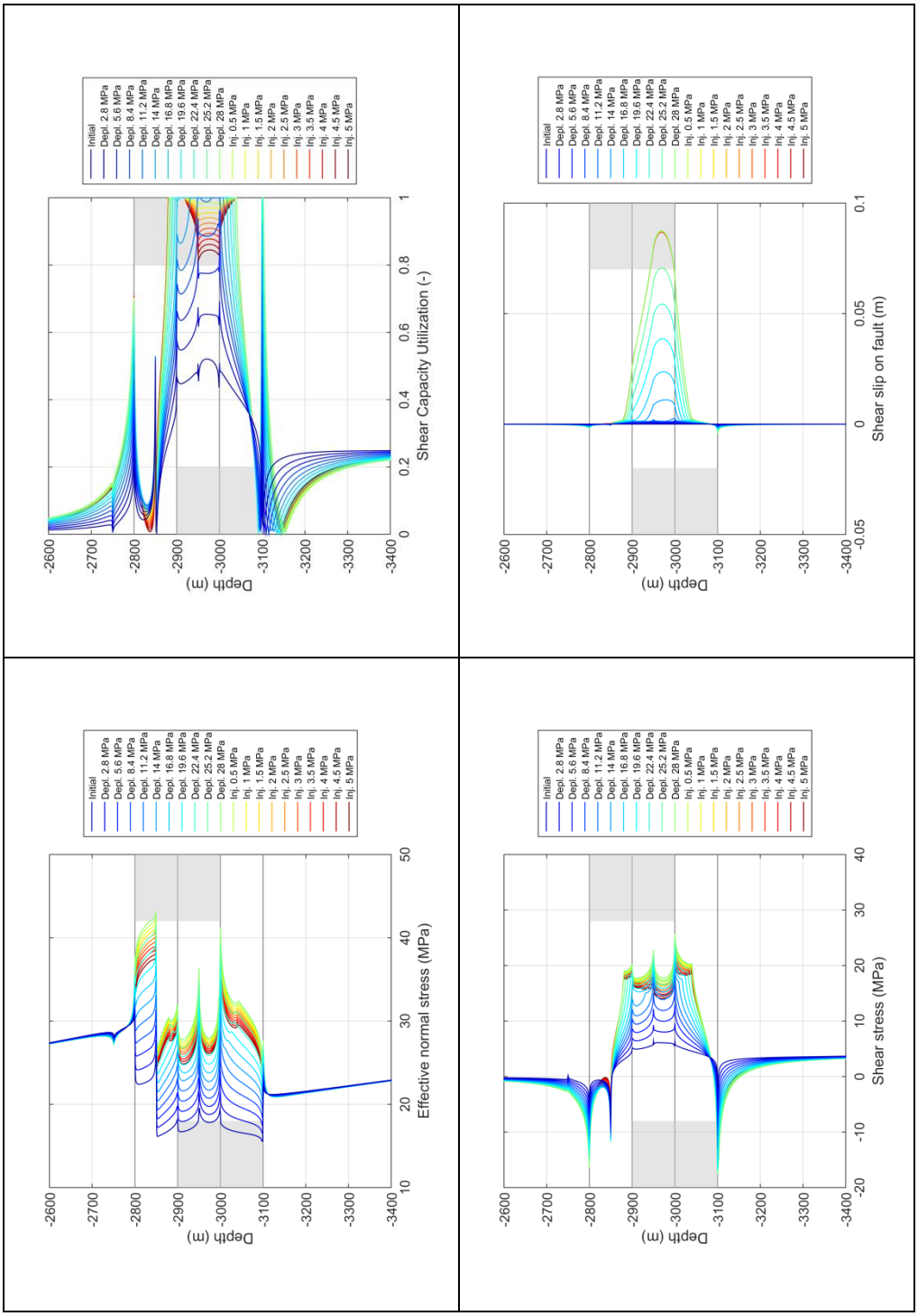

Figure B 20: Evolution of normal effective stress, shear capacity utilization (SCU), shear stress and fault slip (both elastic and plastic) during depletion and injection for the scenario of mechanism with v=0.1.

Mechanism 2: *v* = 0.3

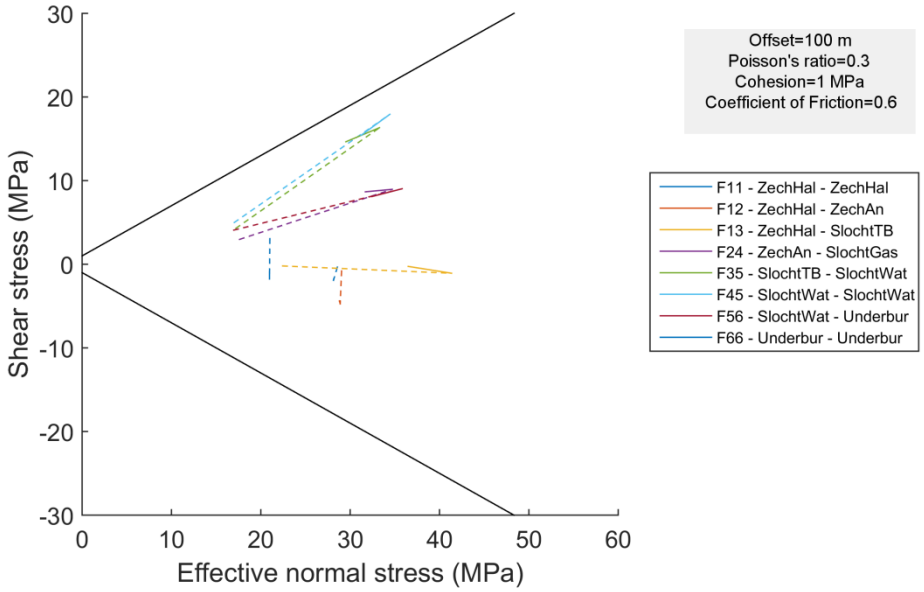

Figure B 21: Stress paths for scenario of mechanism 2 with Poisson's ratio value of 0.3. Dashed lines present the stress paths during depletion, solid lines the stress paths during injection.

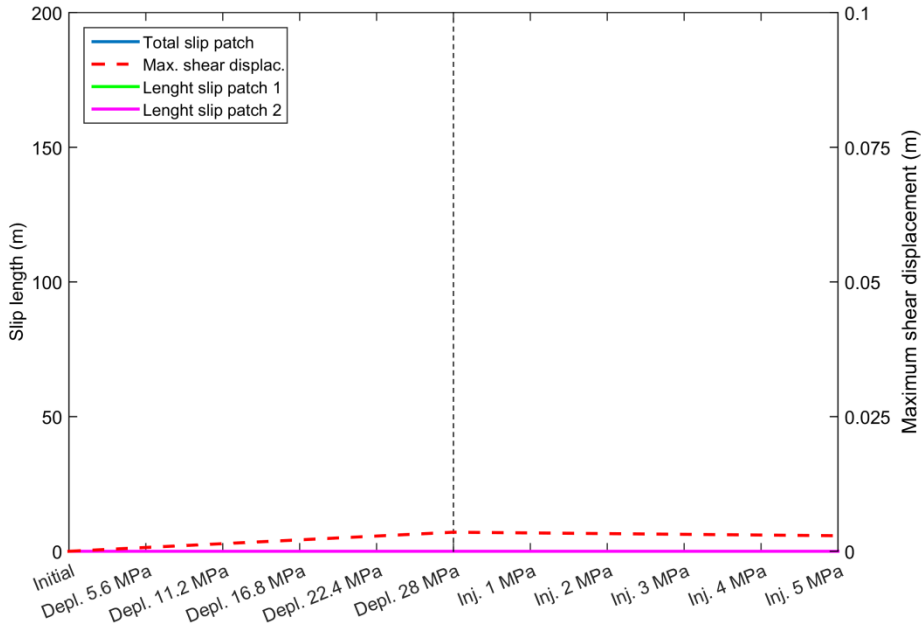

Figure B 22: Evolution of slip length and maximum relative shear displacement for scenario of mechanism 2 with Poisson's ratio value of 0.3.

Mechanism 2: v = 0.3

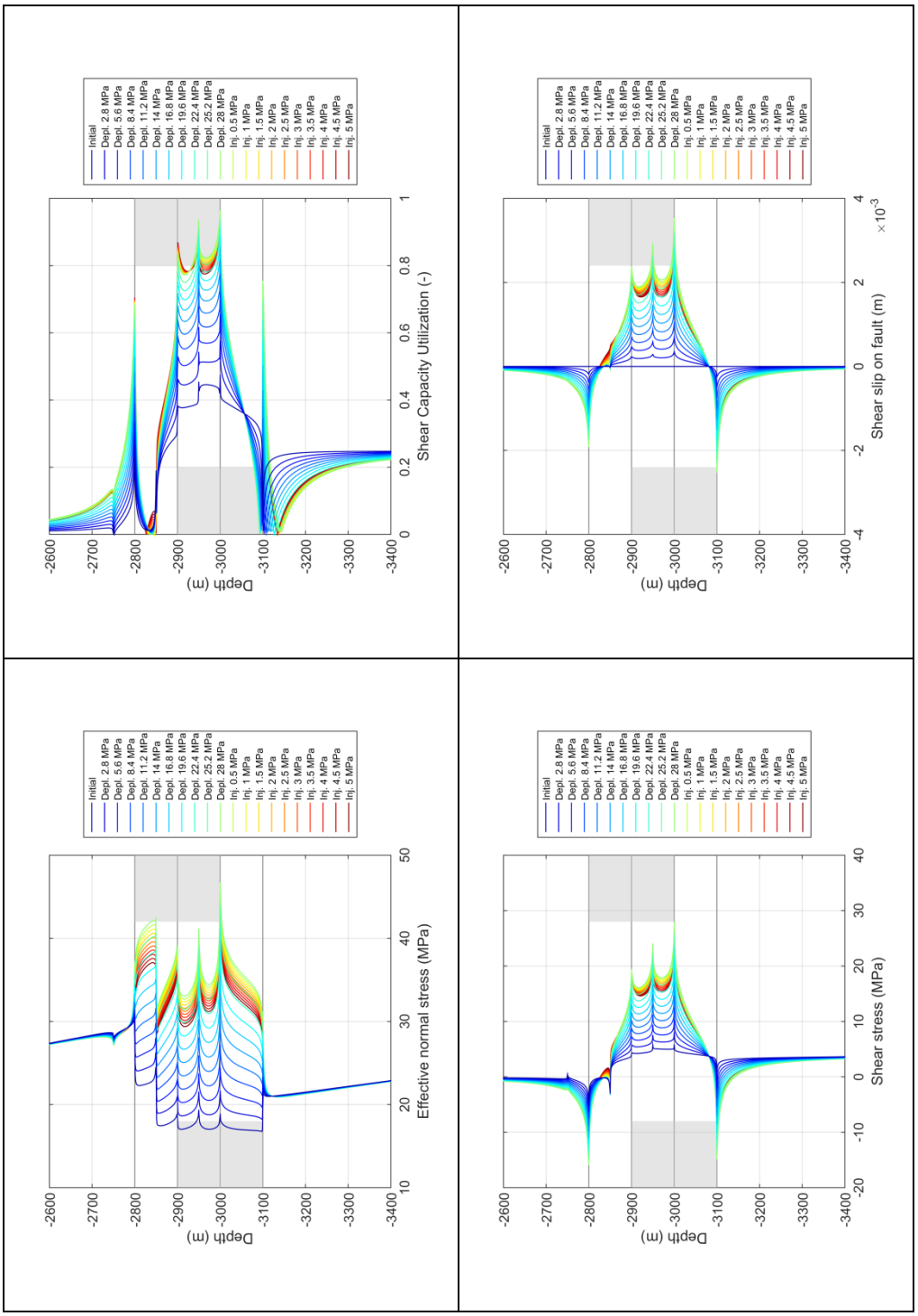

Figure B 23: Evolution of normal effective stress, shear capacity utilization (SCU), shear stress and fault slip (both elastic and plastic) during depletion and injection for the scenario of mechanism 2 with v=0.3.

Mechanism 2: *v* = 0.1 and *v* = 0.3

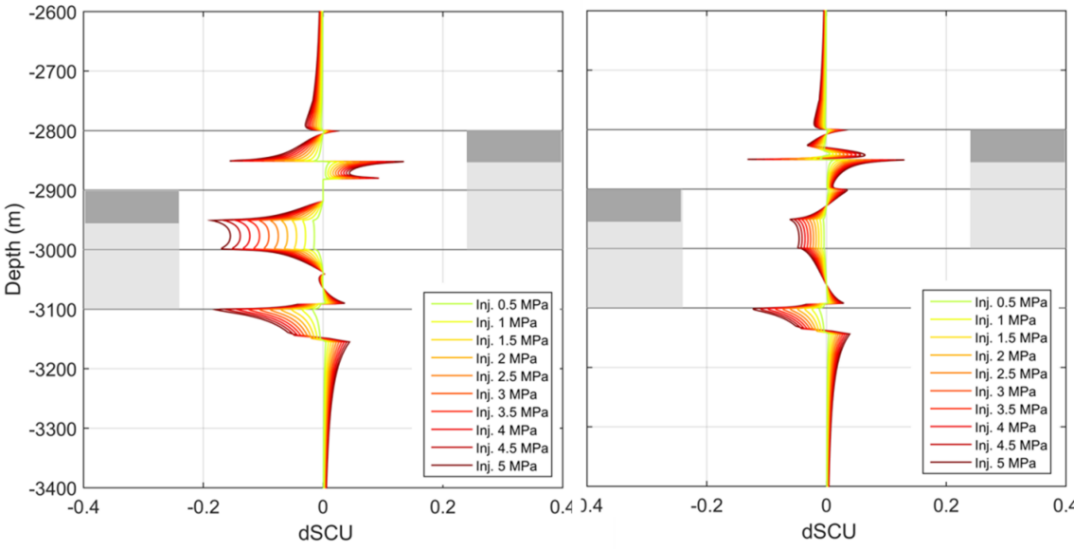

Figure B 24: Change in shear capacity utilization for the scenario of Poisson's ratio values *v*=0.1 (left) and *v*=0.3 (right).

Mechanism 2: No slip during depletion

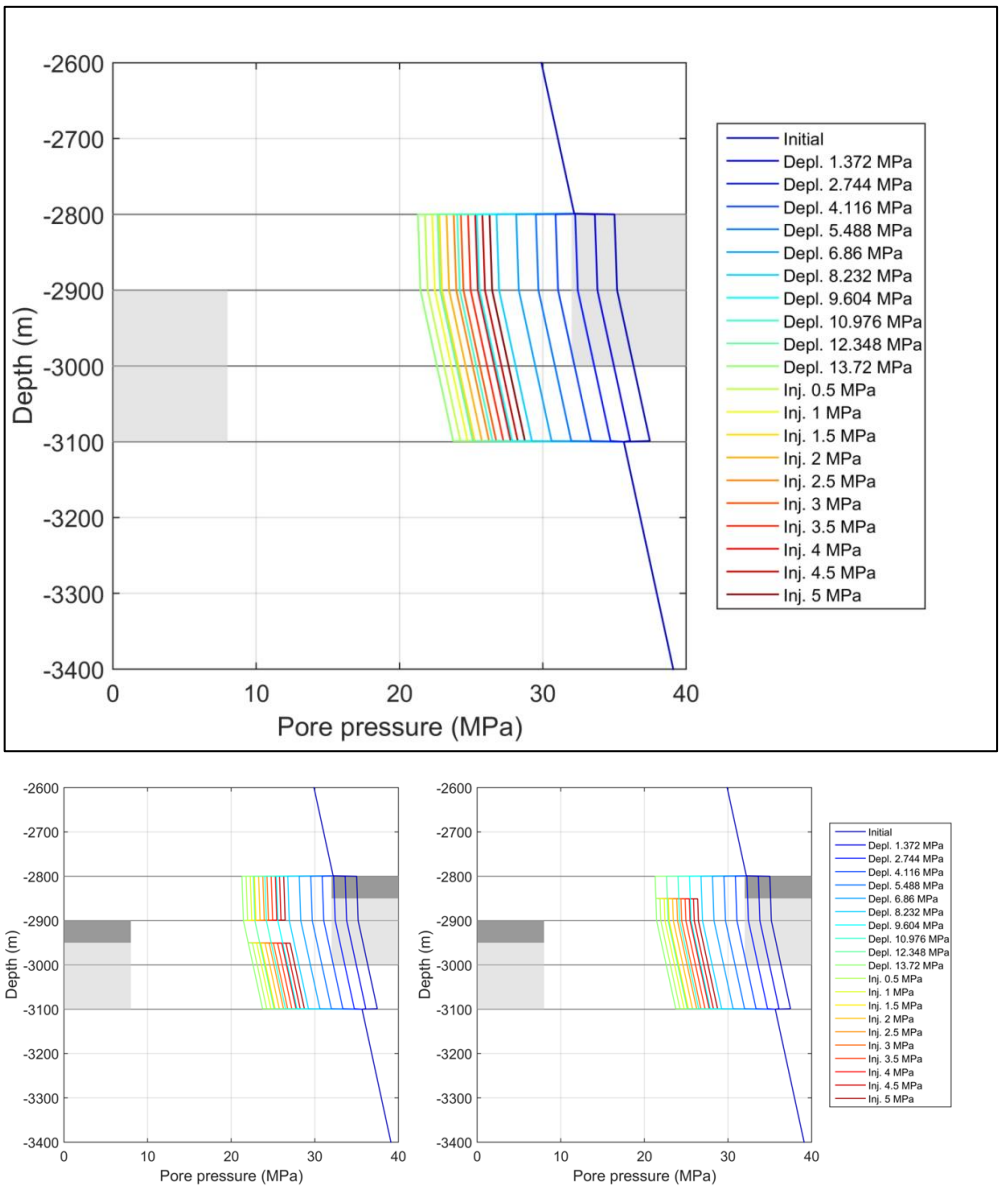

Figure B 25: Upper graph: Pore pressure loading *within the fault* for the scenario of no slip during depletion. Lower left plot: Pore pressure loading outside the fault, *hanging wall* block, lower right plot: Pore pressure loading outside the fault, *footwall block*.

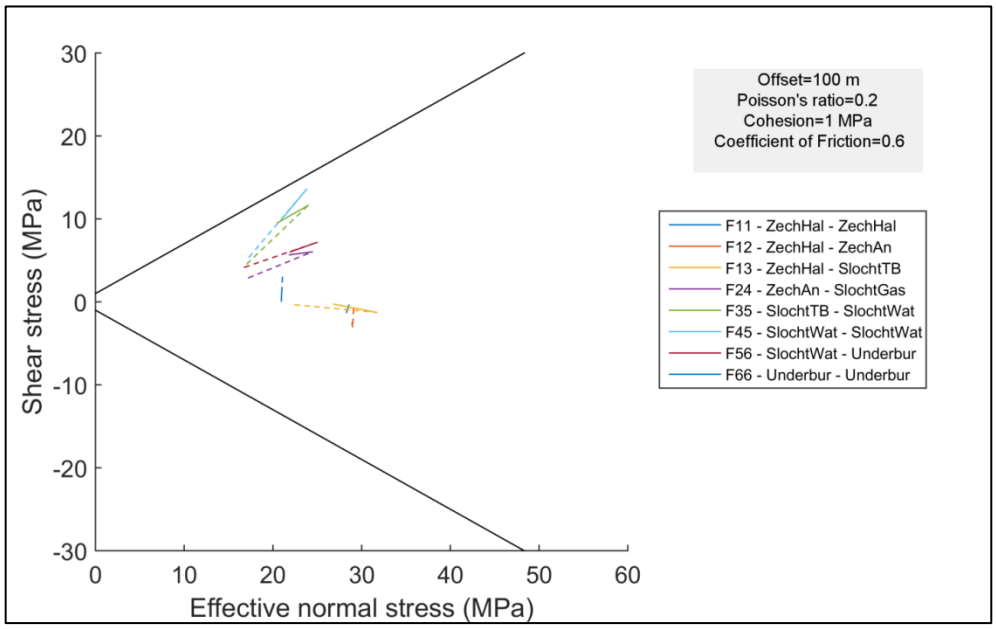

Figure B 26: Stress paths for scenario of mechanism 2 with no slip during depletion. Dashed lines present the stress paths during depletion, solid lines the stress paths during injection.

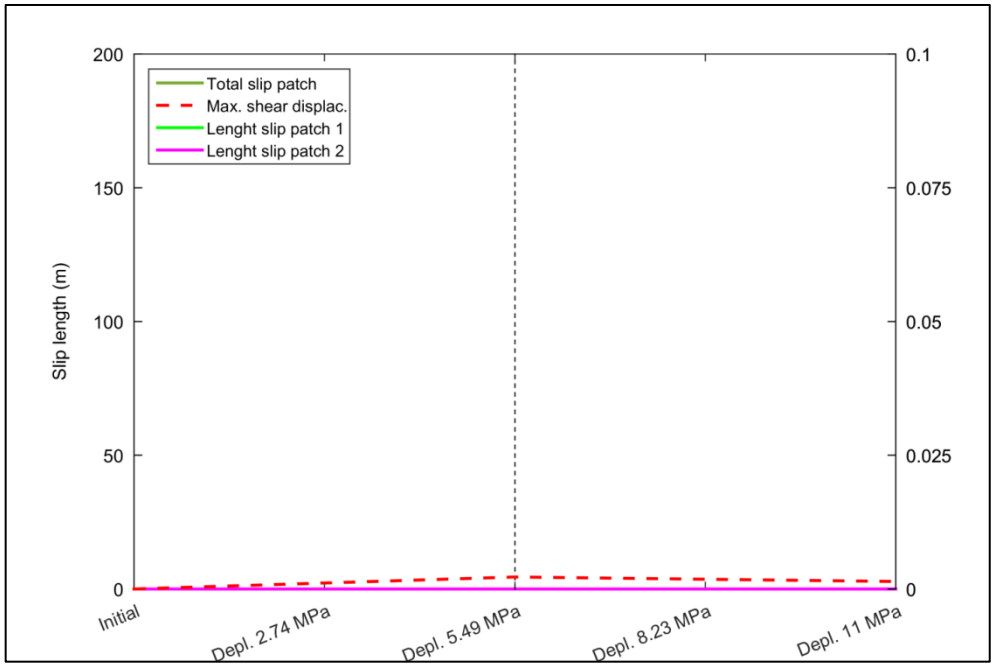

Figure B 27: Evolution of slip length and maximum relative shear displacement for scenario of no slip during depletion.

Mechanism 2: No slip during depletion

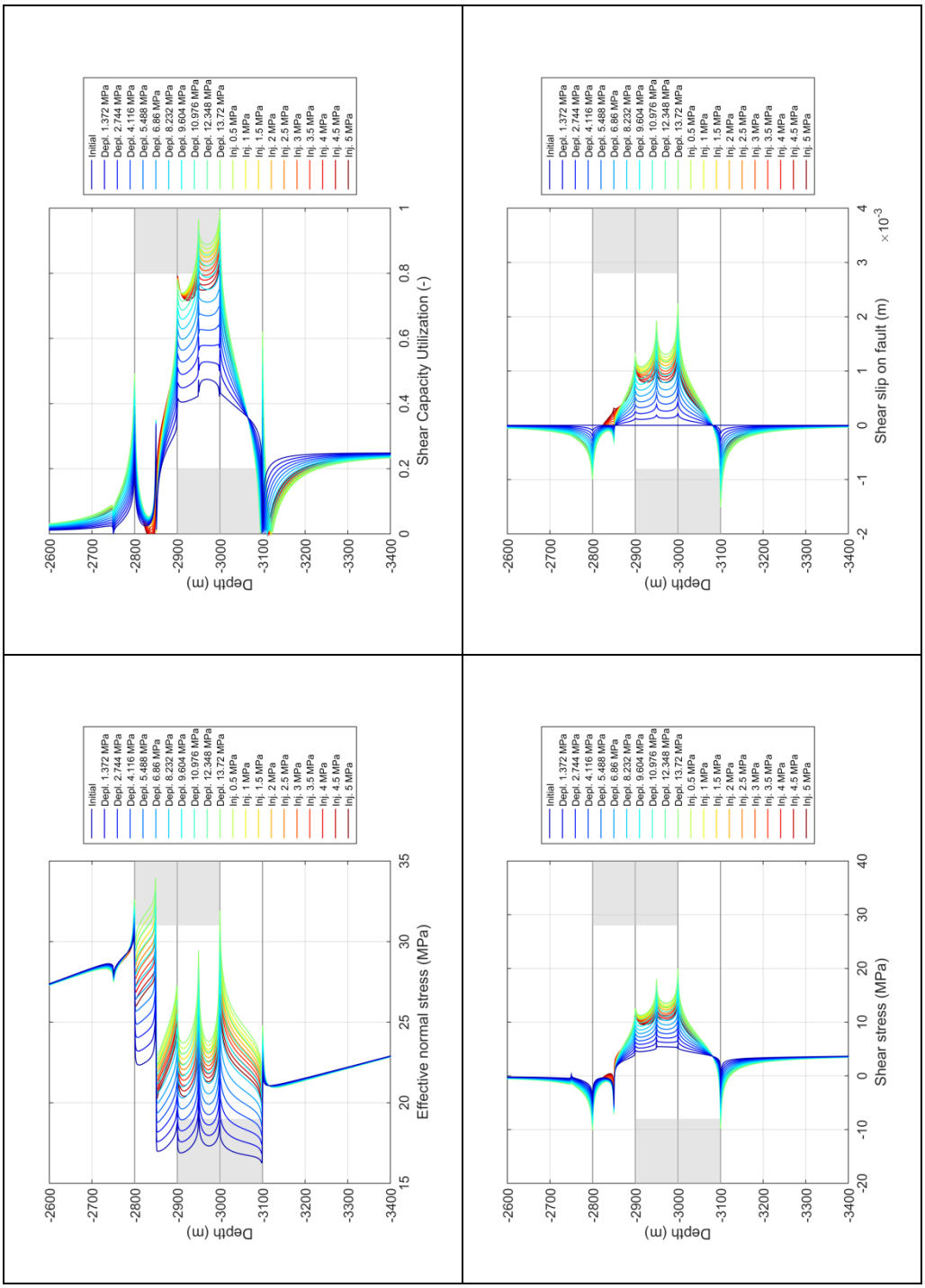

Figure B 28: Evolution of normal effective stress, shear capacity utilization (SCU), shear stress and fault slip (both elastic and plastic) during depletion and injection for the scenario of no slip during depletion.

Mechanism 2: No slip during depletion

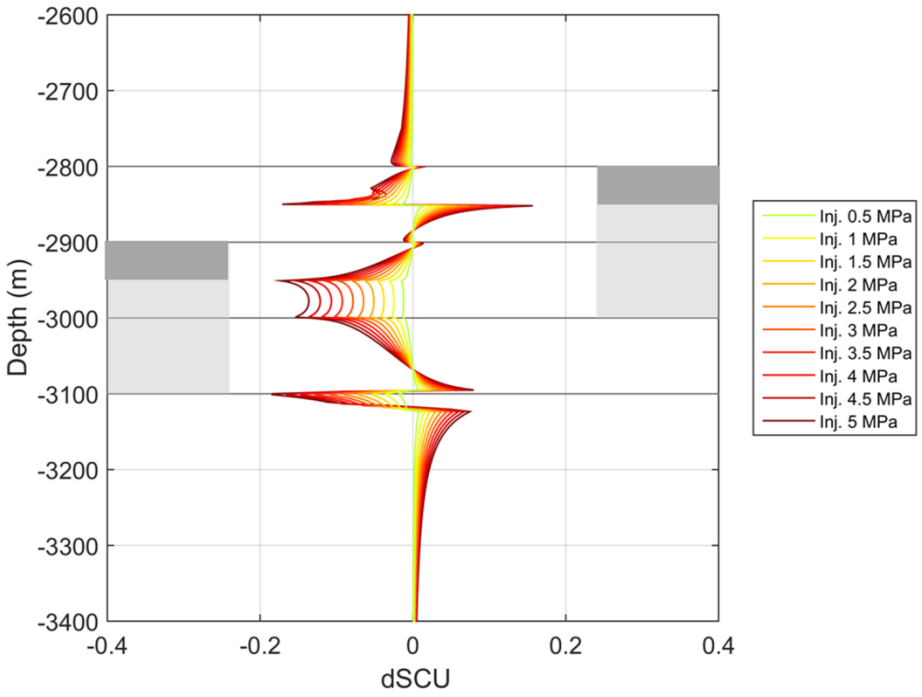

Figure B 29: Change in shear capacity utilization for the scenario of no slip during depletion.

Mechanism 2: Increased depletion

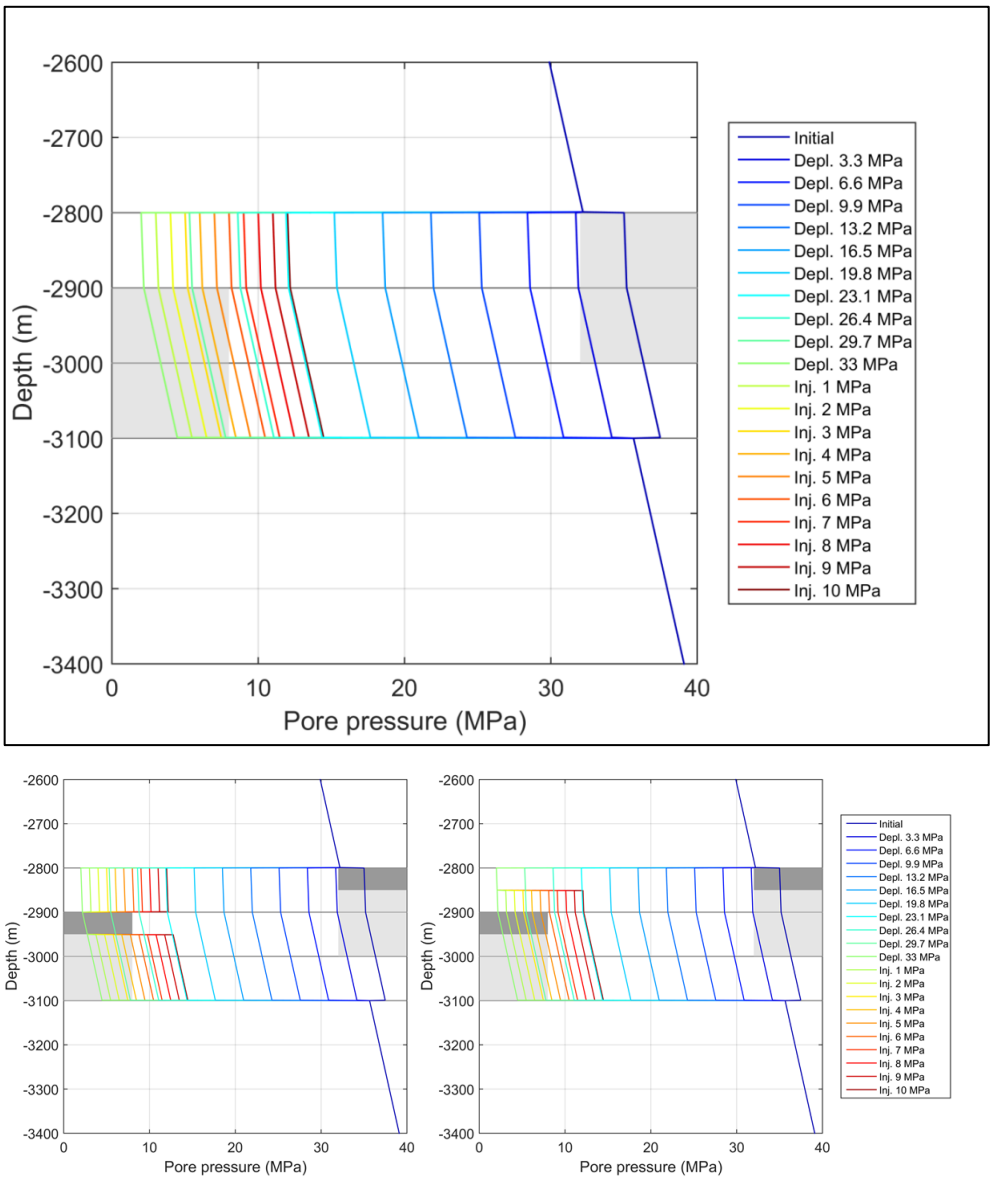

Figure B 30: Upper plot: Pore pressure loading *within the fault* for the scenario of increased depletion. Lower left: Pore pressure loading *outside the fault*, hanging wall block. Lower right: Pore pressure loading *outside the fault*, footwall block.

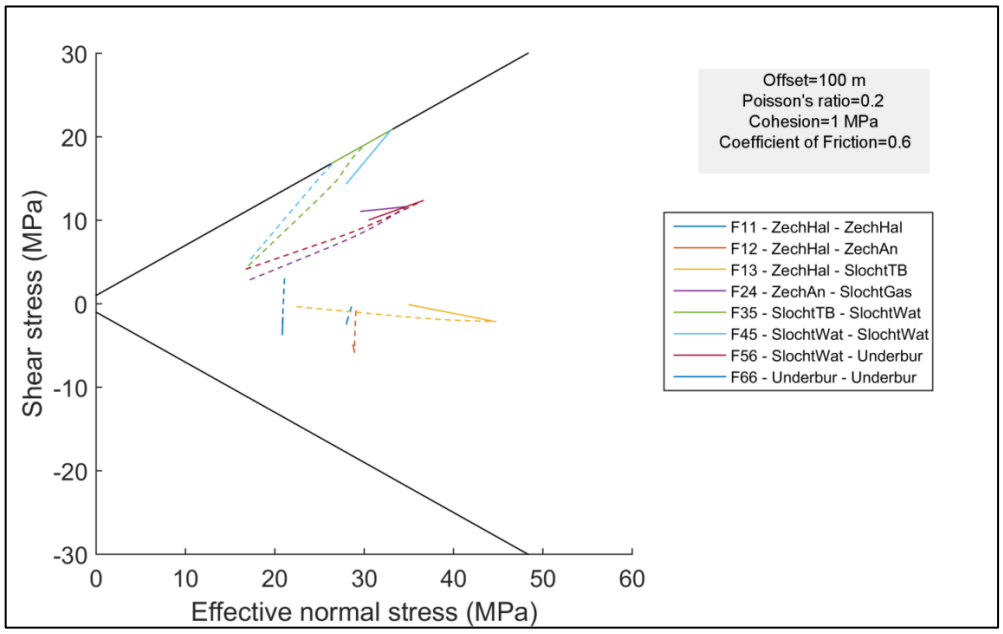

Figure B 31: Stress paths for the scenario of mechanism 2 with increased depletion. Dashed lines present the stress paths during depletion, solid lines the stress paths during injection.

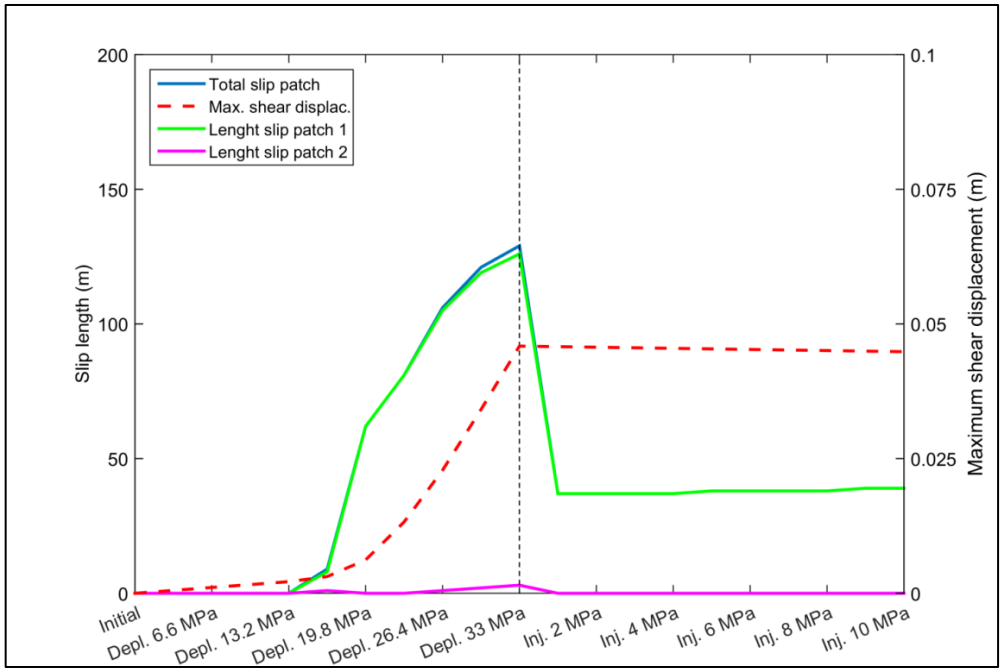

Figure B 32: Evolution of slip length and maximum relative shear displacement for scenario of increased depletion.

Mechanism 2: Increased depletion

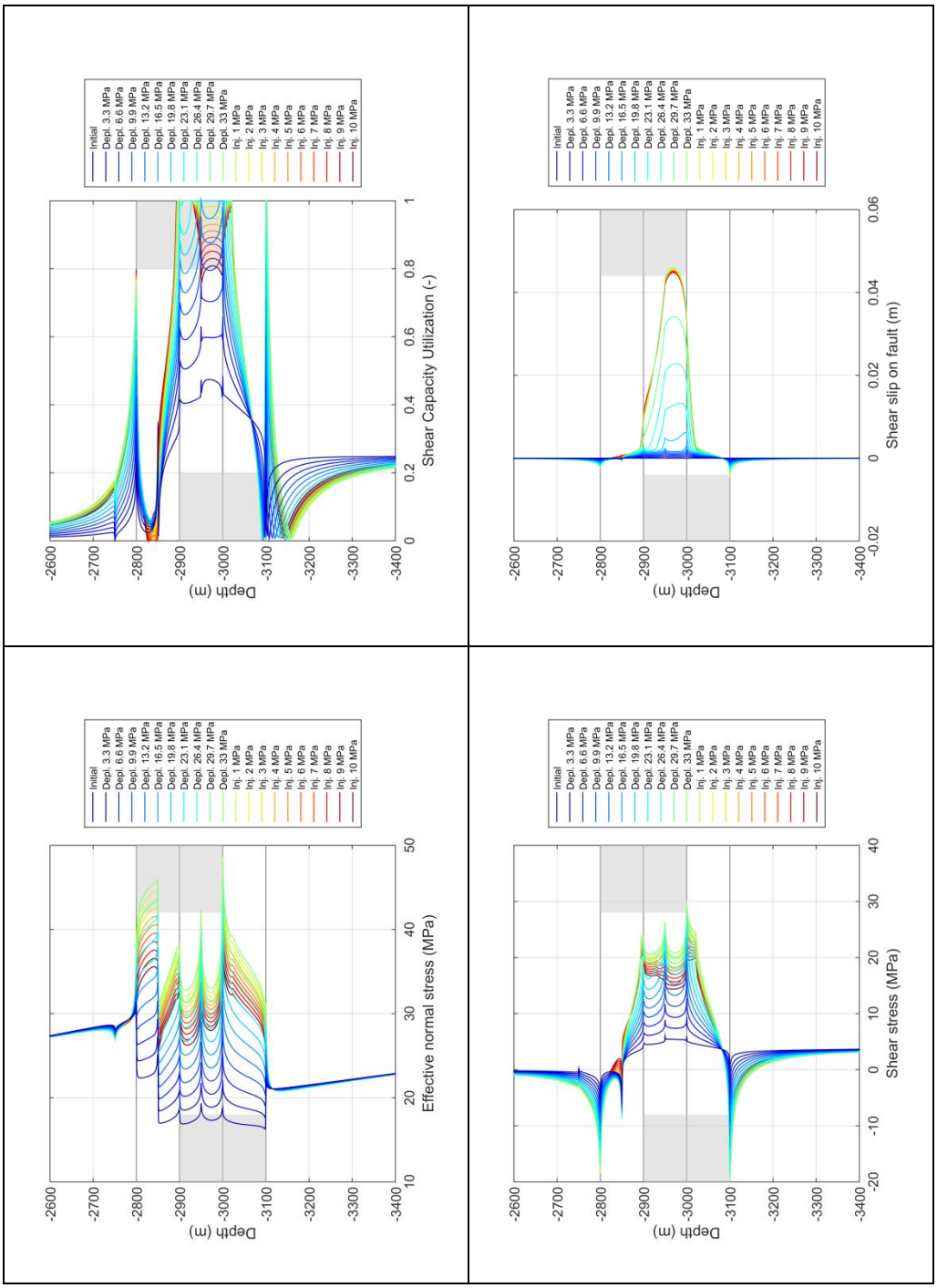

Figure B 33: Evolution of normal effective stress, shear capacity utilization (SCU), shear stress and fault slip (both elastic and plastic) during depletion and injection for the scenario of increased depletion scenario.

Mechanism 2: Increased depletion

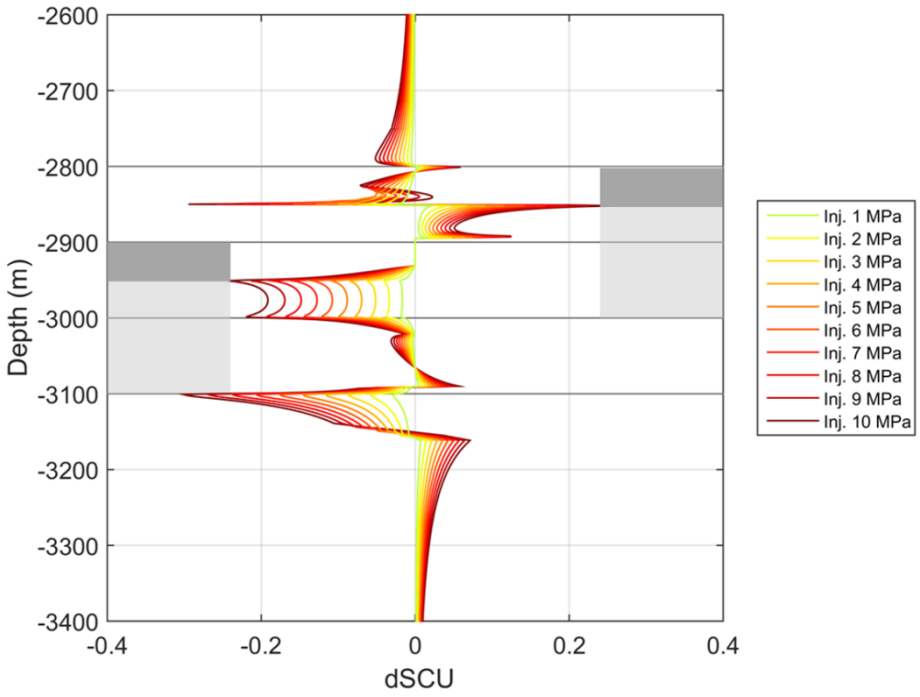

Figure B 34: Change in shear capacity utilization (dSCU) for the scenario of increased depletion.

Mechanism 2: Offset = 0 m

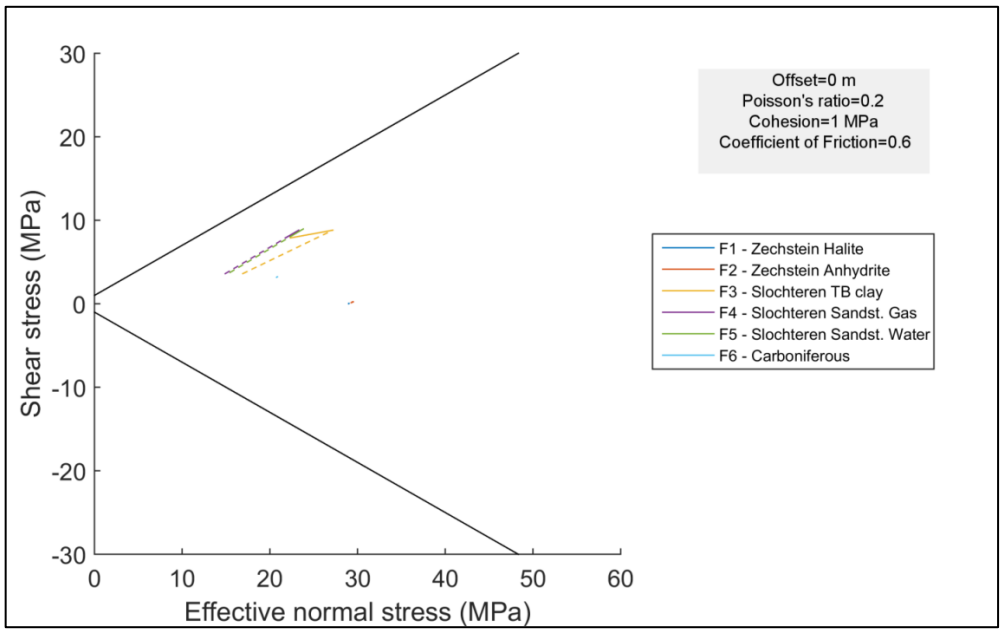

Figure B 35: Stress paths for 0 m offset scenario of mechanism 2. Dashed lines present the stress paths during depletion, solid lines the stress paths during injection.

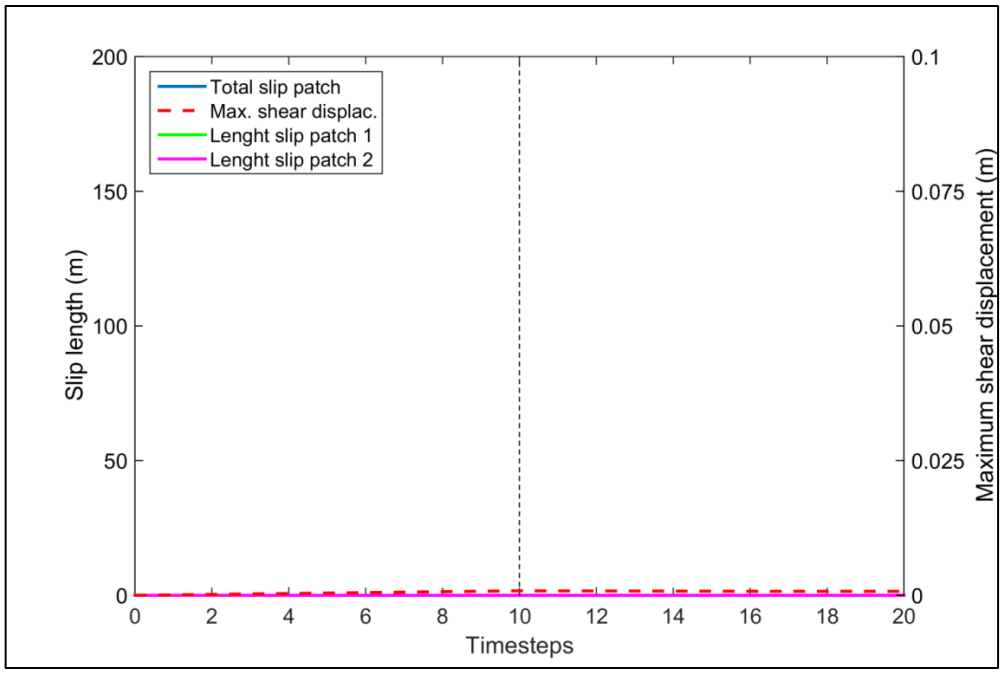

Figure B 36: Evolution of slip length and maximum relative shear displacement for 0 m offset scenario.

Mechanism 2: Offset = 0 m

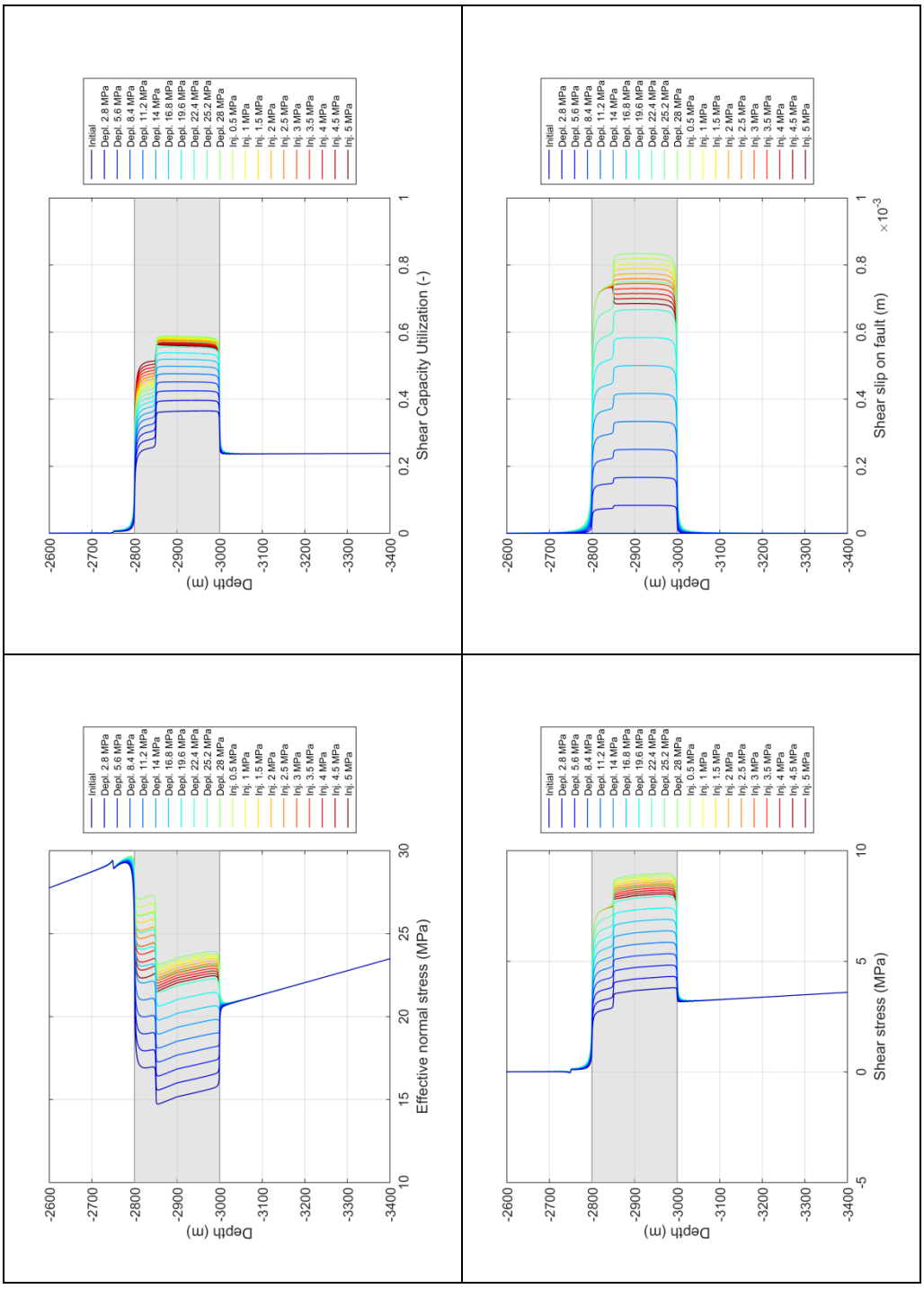

Figure B 37: Evolution of normal effective stress, shear capacity utilization (SCU), shear stress and fault slip (both elastic and plastic) during depletion and injection for the 0 m offset scenario.

Mechanism 2: Offset = 200 m

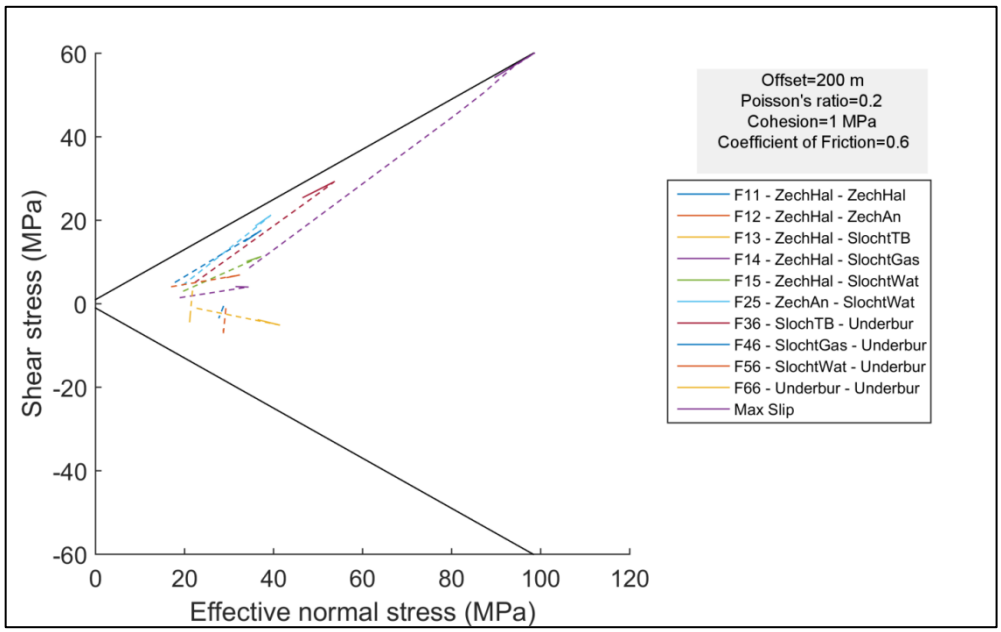

Figure B 38: Stress paths for 200 m offset scenario of mechanism 2. Dashed lines present the stress paths during depletion, solid lines the stress paths during injection.

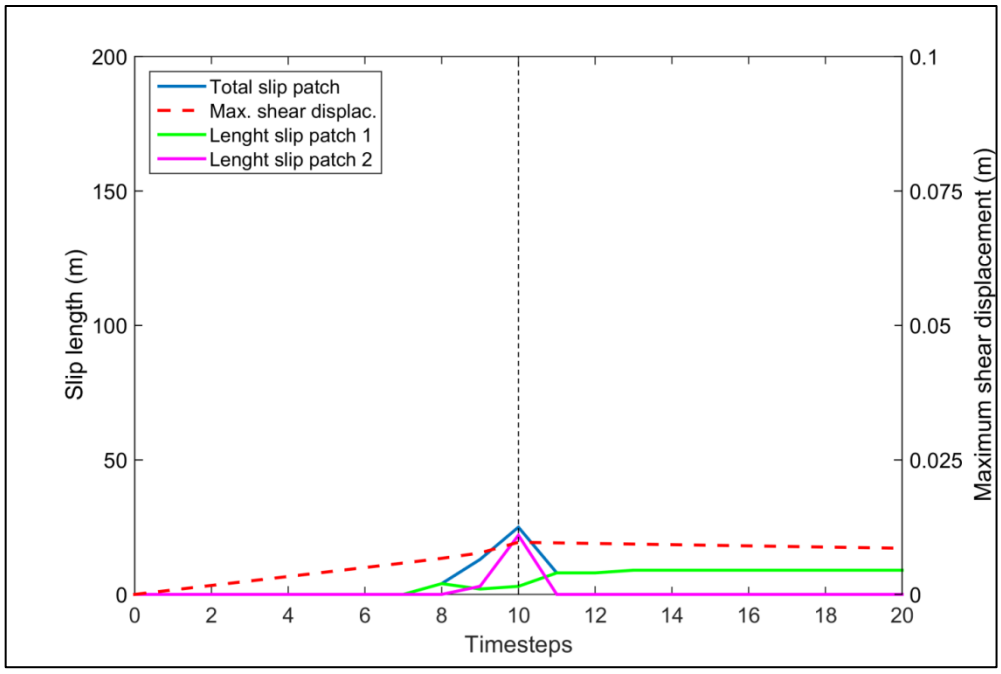

Figure B 39: Evolution of slip length and maximum relative shear displacement for 200 m offset scenario.

Mechanism 2: Offset = 200 m

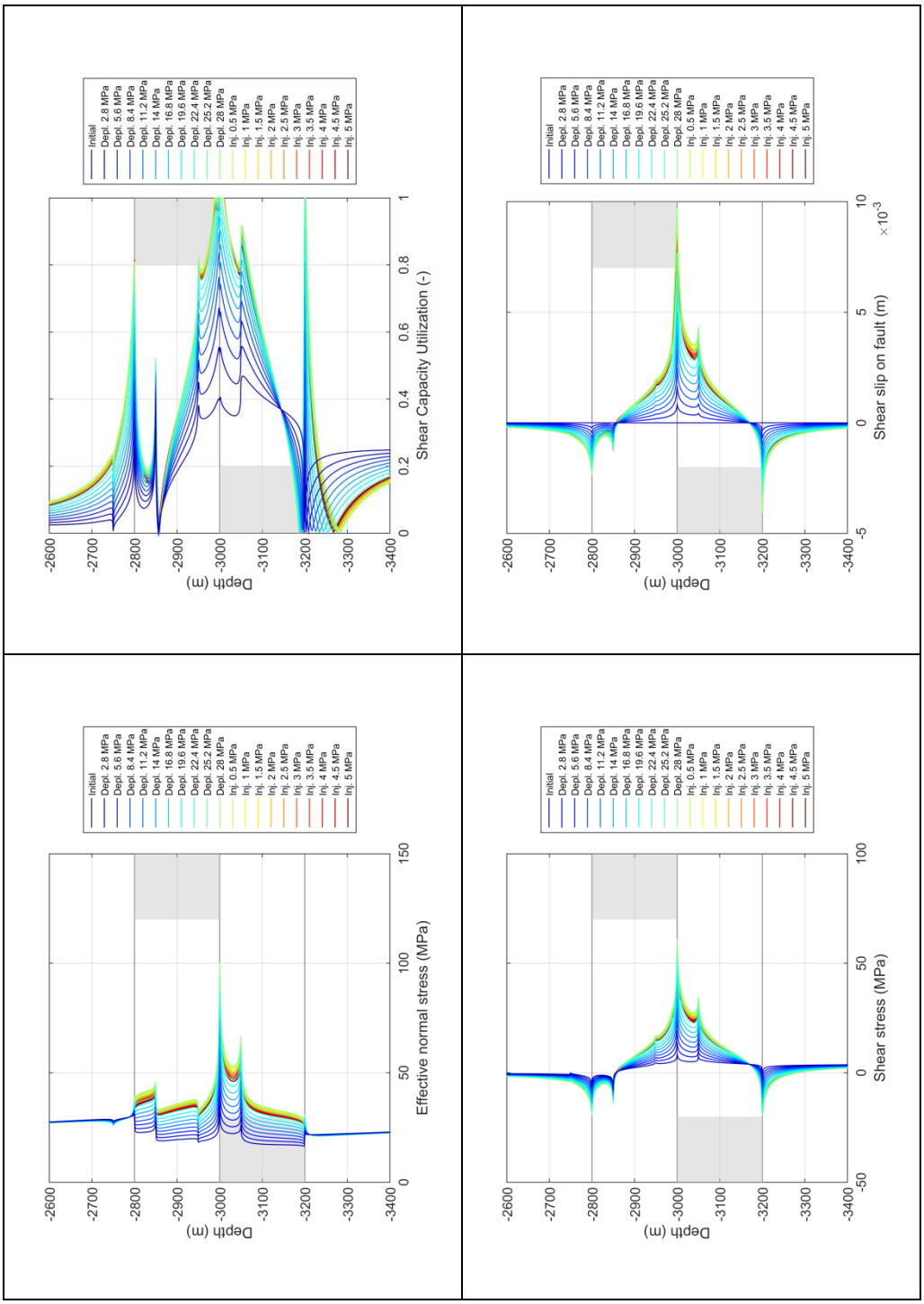

Figure B 40: Evolution of normal effective stress, shear capacity utilization (SCU), shear stress and fault slip (both elastic and plastic) during depletion and injection for the 200 m offset scenario

Mechanism 2 Fault offset 0 m and 200 m

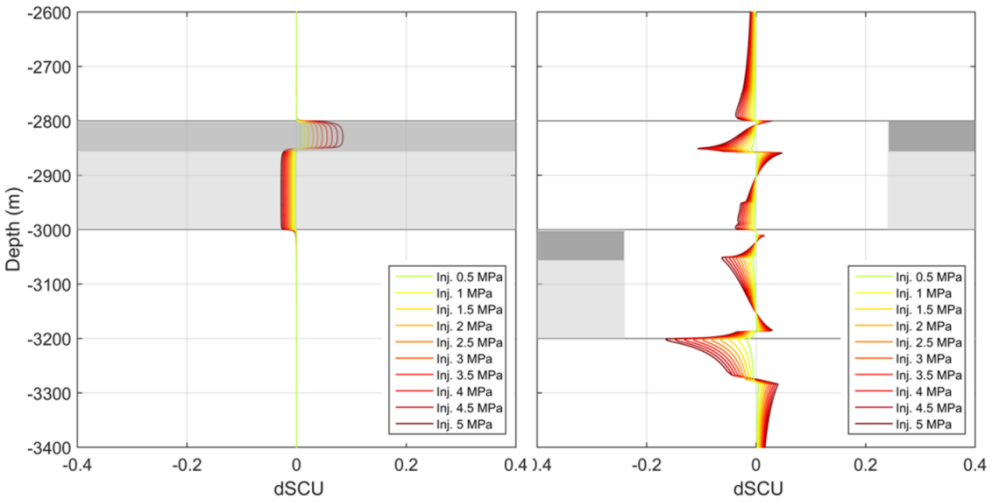

Figure B 41: Change in shear capacity utilization for the scenario of 0 m offset (left) and 200 m offset (right).

C Appendix – Irreversible stress paths during production and injection

Mechanism 3: $v_{injection}$ = 0.30

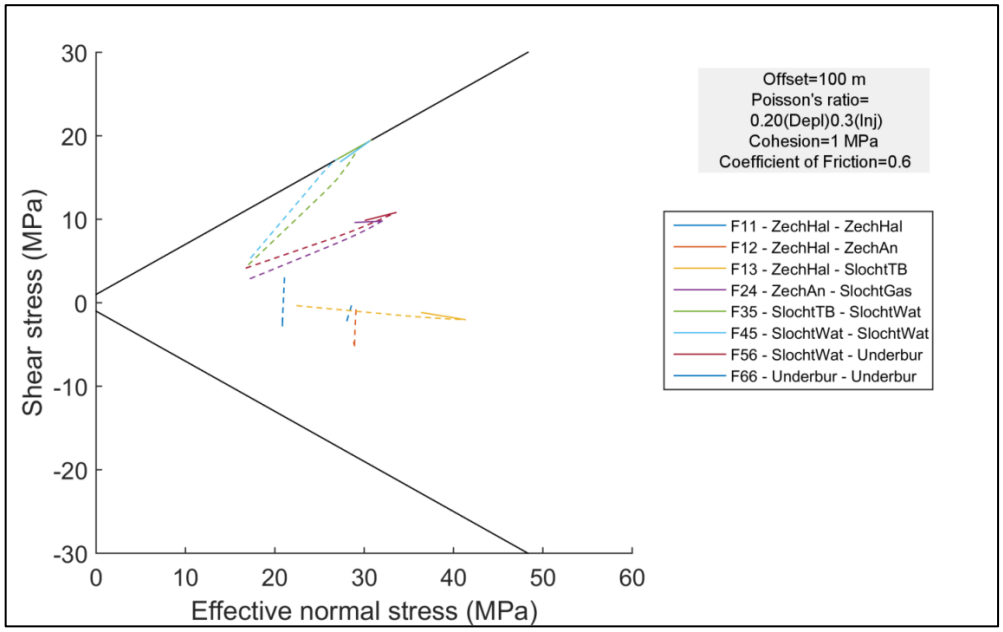

Figure C 1: Stress paths for the scenario of mechanism 3 with $v_{injection}$ =0.30. Dashed lines present the stress paths during depletion, solid lines the stress paths during injection.

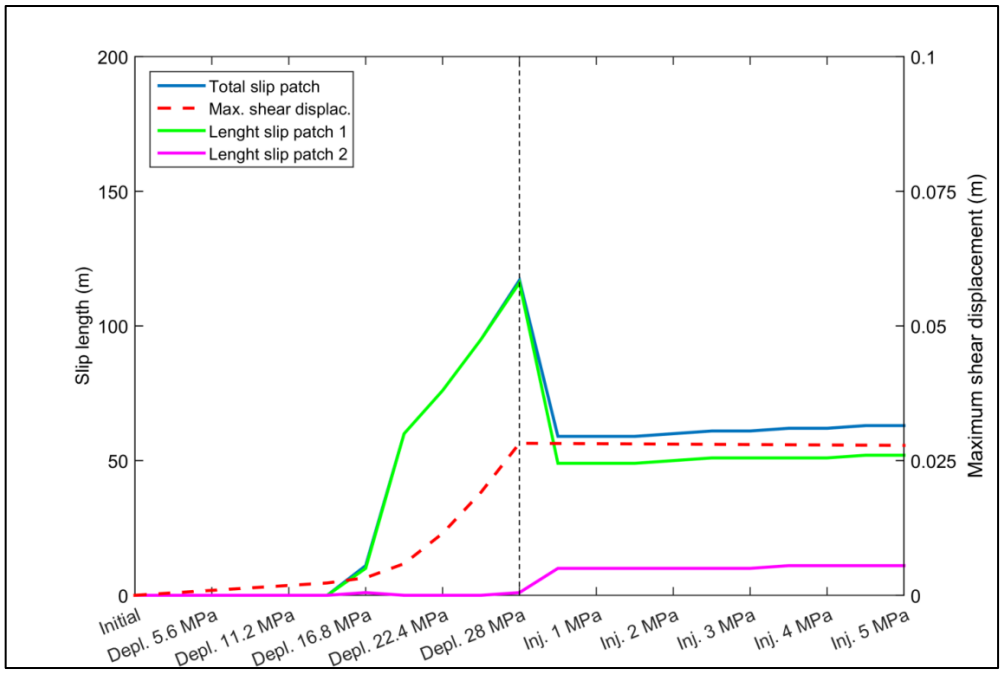

Figure C 2: Evolution of slip length and maximum relative shear displacement for the scenario of mechanism 3 with $v_{injection}$ =0.30.

Mechanism 2: $v_{injection}$ = 0.30

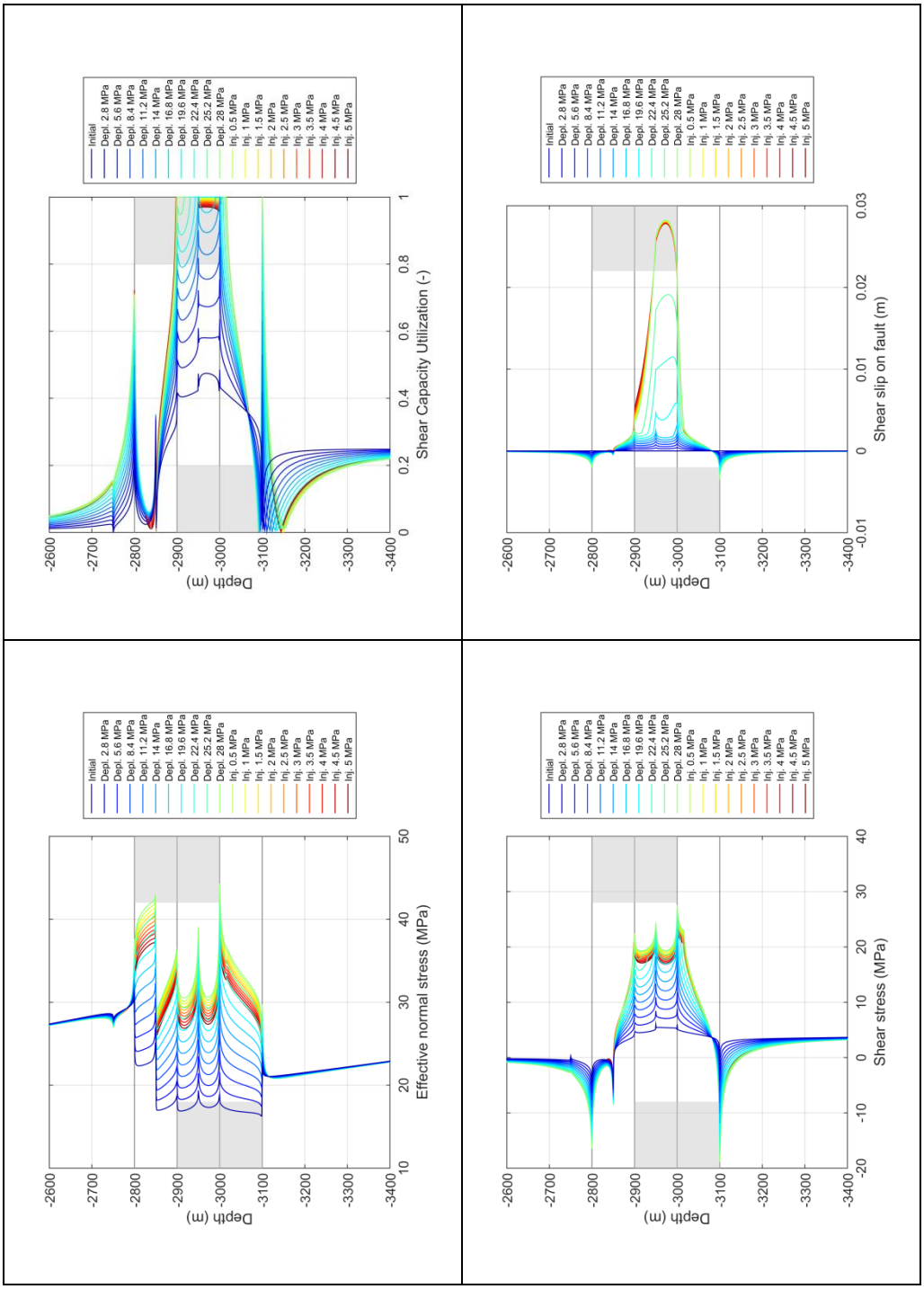

Figure C 3: Evolution of normal effective stress, shear capacity utilization (SCU), shear stress and fault slip (both elastic and plastic) for the scenario of mechanism 3 with $v_{injection}$ =0.30.

Mechanism 3: $v_{injection}$ = 0.40

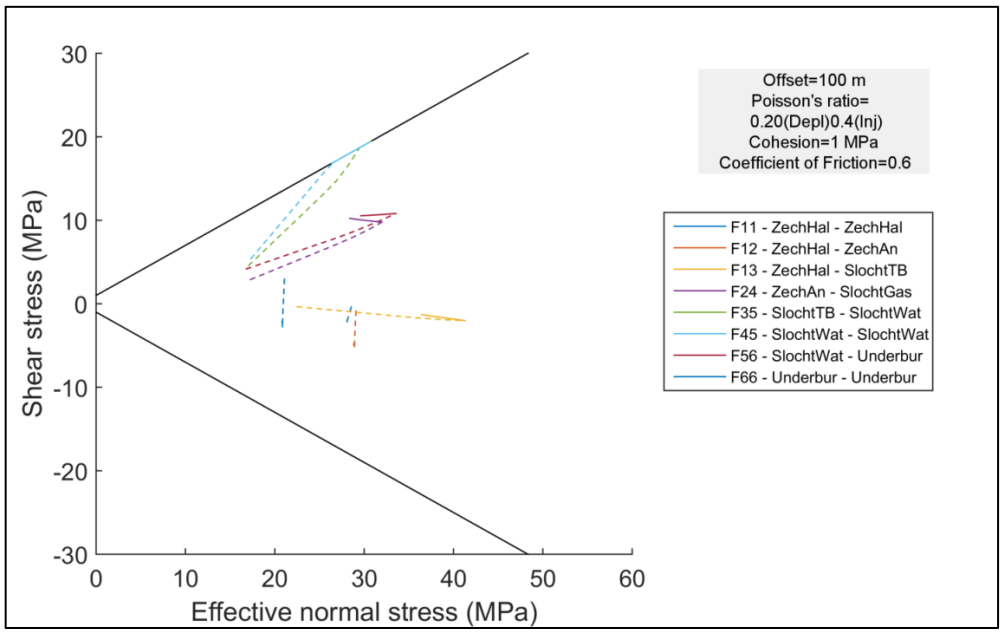

Figure C 4: Stress paths for the scenario of mechanism 3 with $v_{injection}$ =0.40. Dashed lines present the stress paths during depletion, solid lines the stress paths during injection.

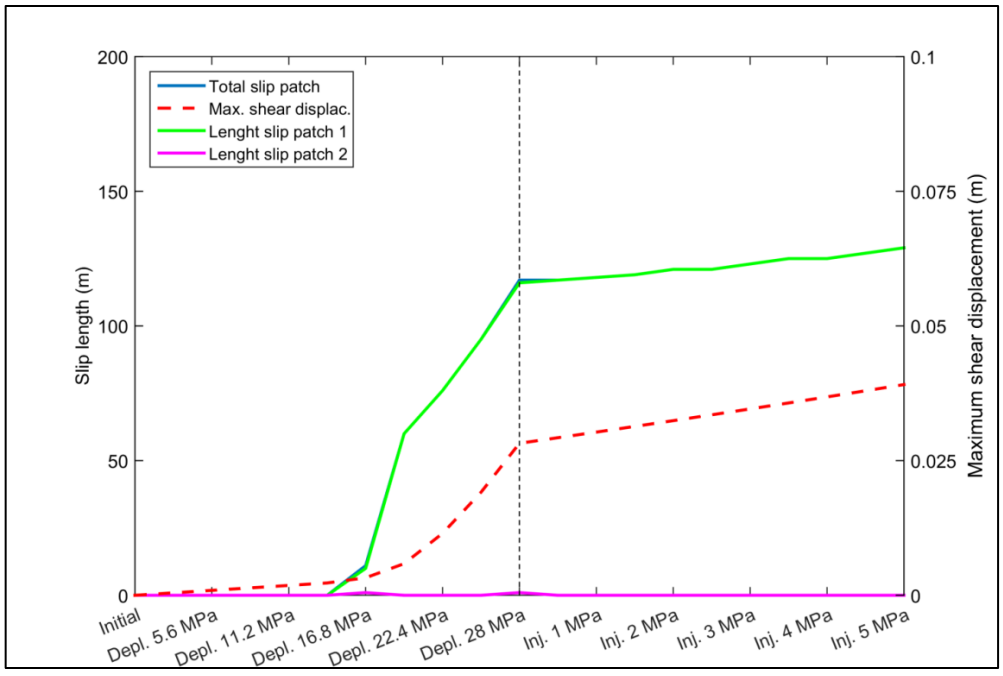

Figure C 5: Evolution of slip length and maximum relative shear displacement for the scenario of mechanism 3 with $v_{injection}$ =0.40.

Mechanism 2: $v_{injection}$ = 0.40

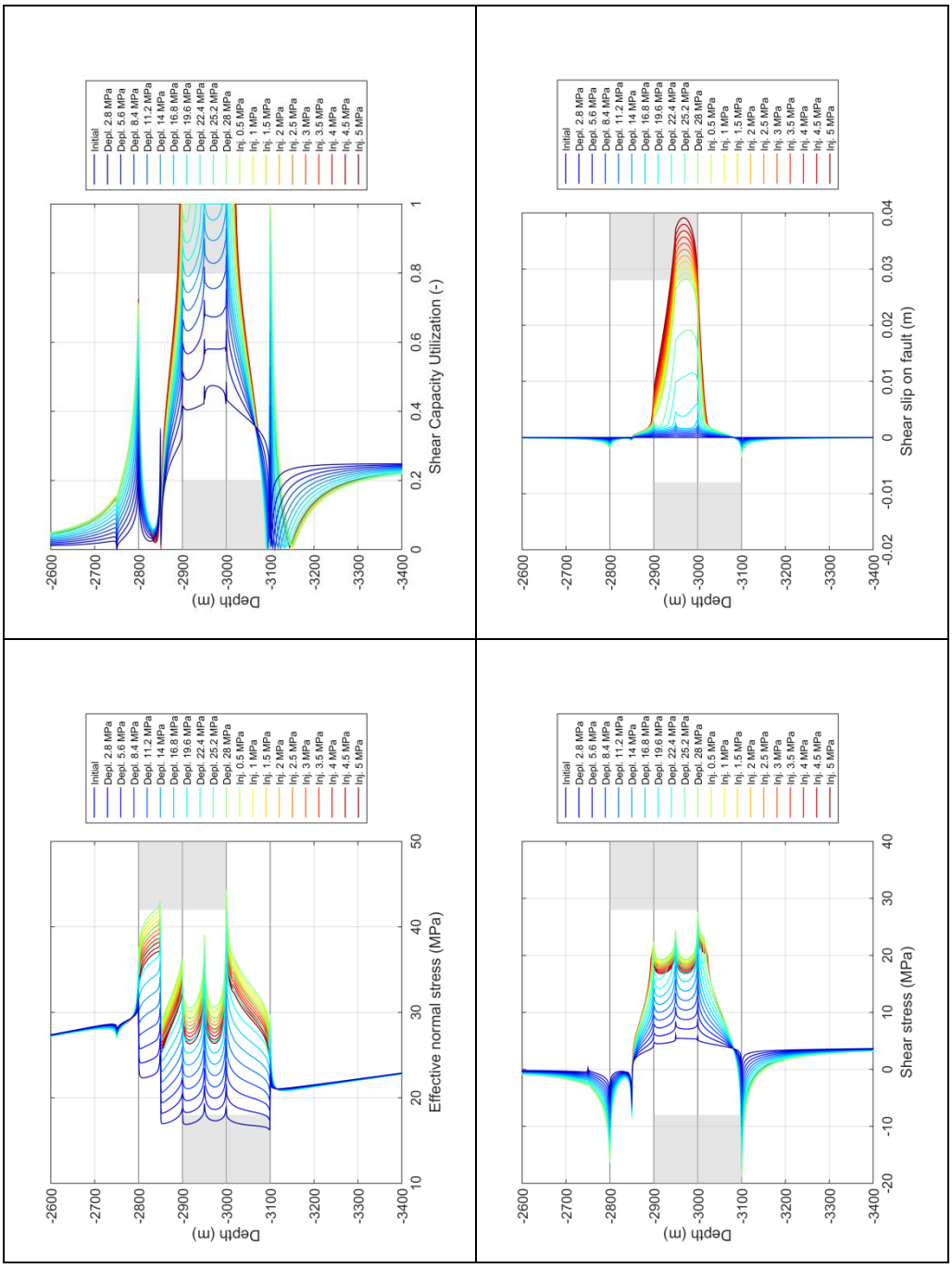

Figure C 6: Evolution of normal effective stress, shear capacity utilization (SCU), shear stress and fault slip (both elastic and plastic) for the scenario of mechanism 3 with $v_{injection}$ =0.40.

Mechanism 3: $v_{injection}$ = 0.48

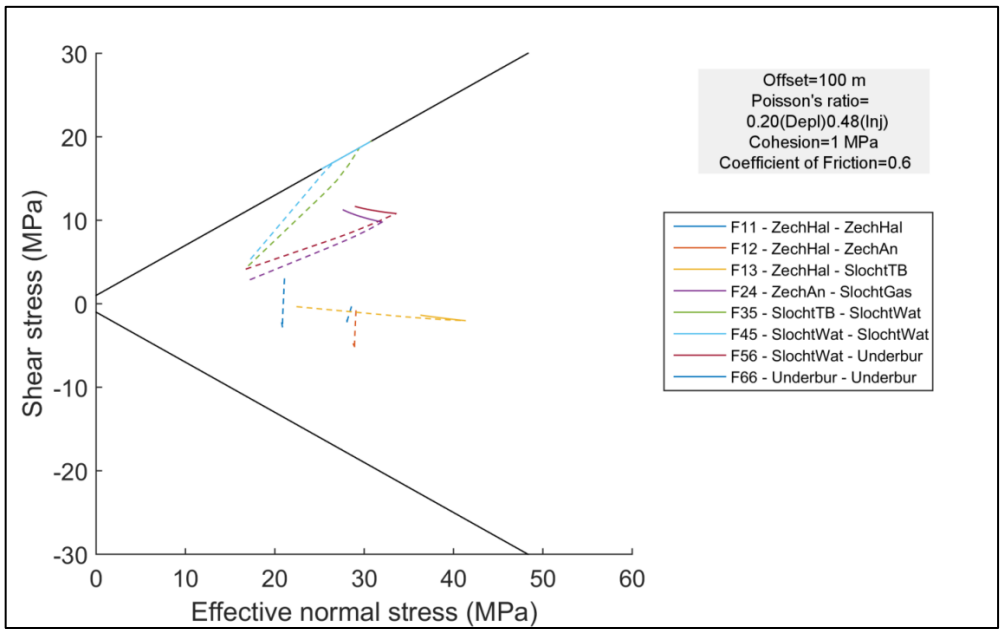

Figure C 7: Stress paths for the scenario of mechanism 3 with $v_{injection}$ =0.48. Dashed lines present the stress paths during depletion, solid lines the stress paths during injection.

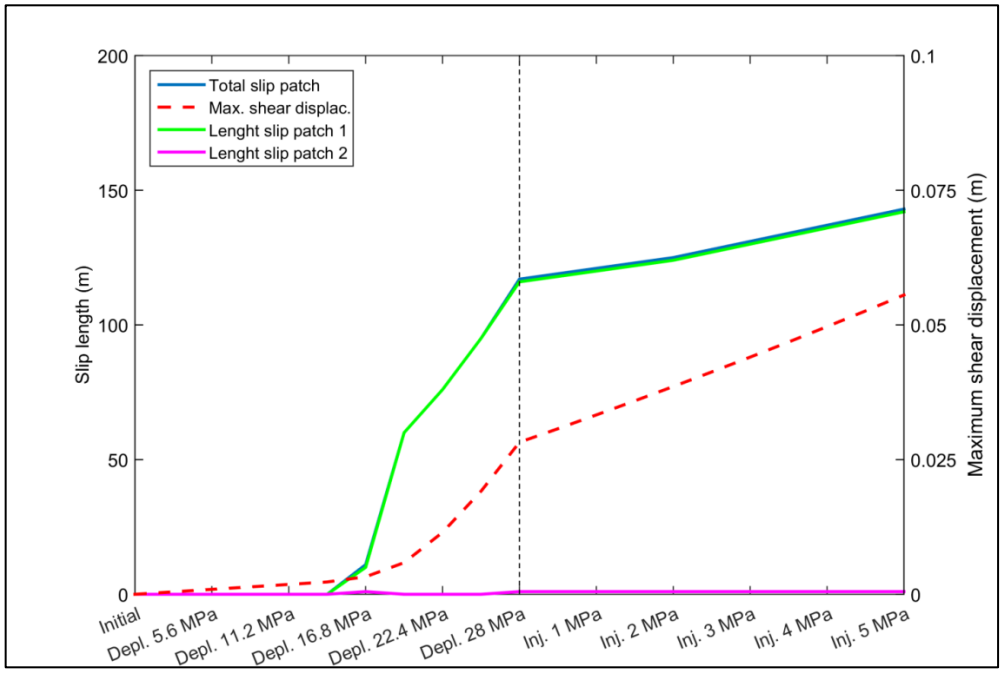

Figure C 8: Evolution of slip length and maximum relative shear displacement for the scenario of mechanism 3 with $v_{injection}$ =0.48.

Mechanism 3: $v_{injection}$ = 0.48

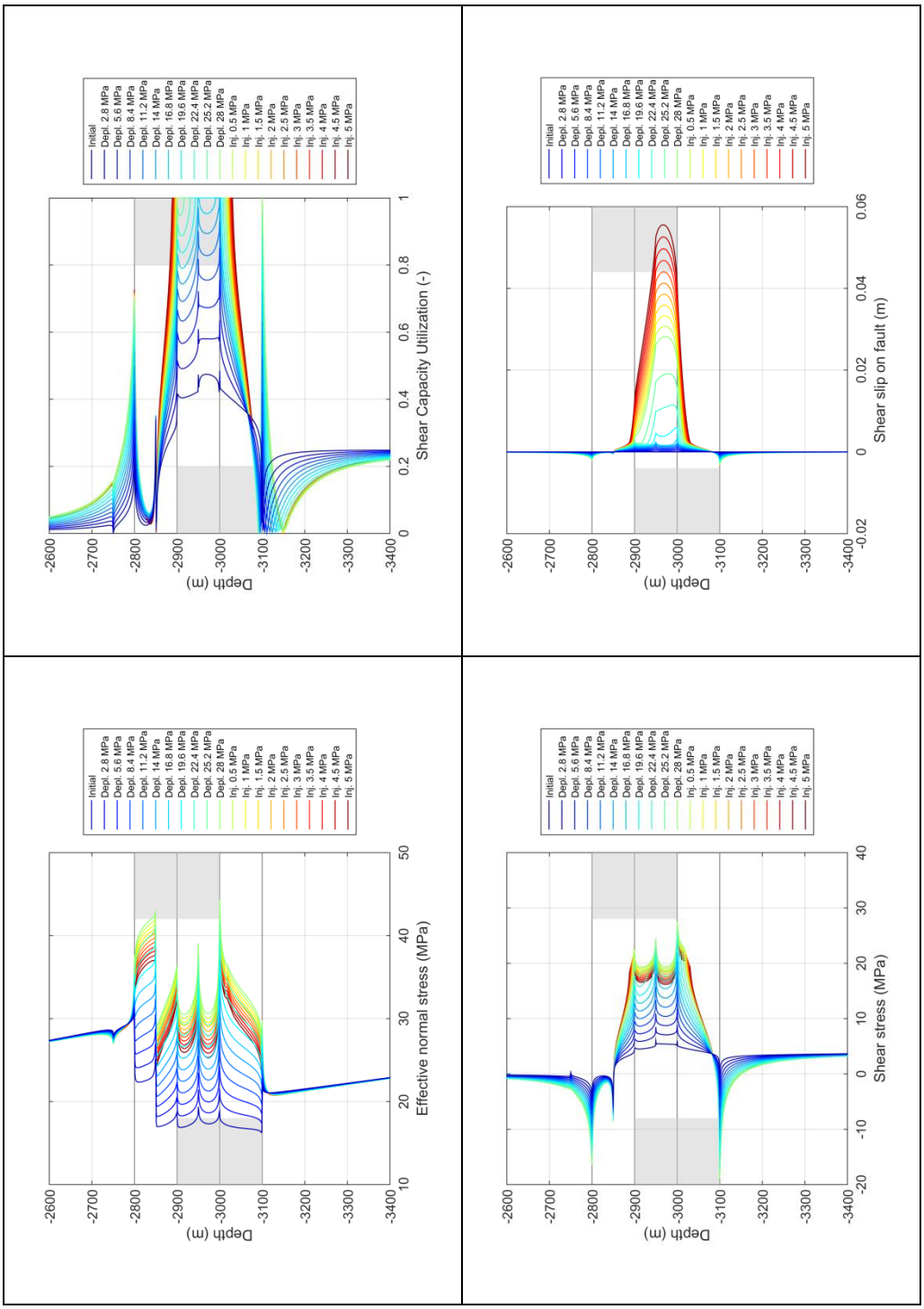

Figure C 9: Evolution of normal effective stress, shear capacity utilization (SCU), shear stress and fault slip (both elastic and plastic) for the scenario of mechanism 3 with $v_{injection}$ =0.48.

Mechanism 3: $v_{injection}$ = 0.30, = 0.40 and = 0.48, and base case scenario

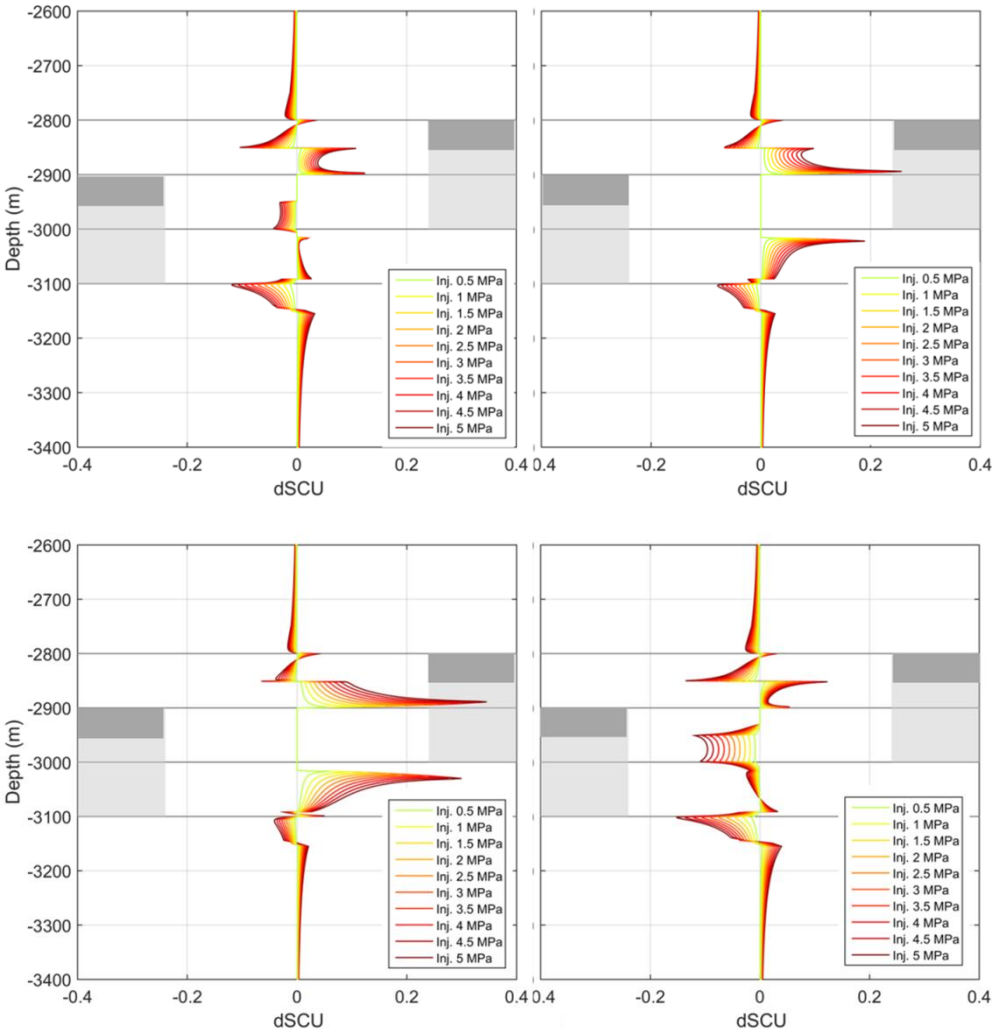

Figure C 10: Change in shear capacity utilization for the scenarios of mechanism 3 with $v_{injection}$=0.30 (top left), $v_{injection}$=0.40 (top right), $v_{injection}$=0.48 (bottom left) and base case scenario $v_{injection}$=0.20 (bottom right).

Mechanism 3: $v_{injection}$ = 0.30, = 0.40 and = 0.48 compared to ongoing depletion

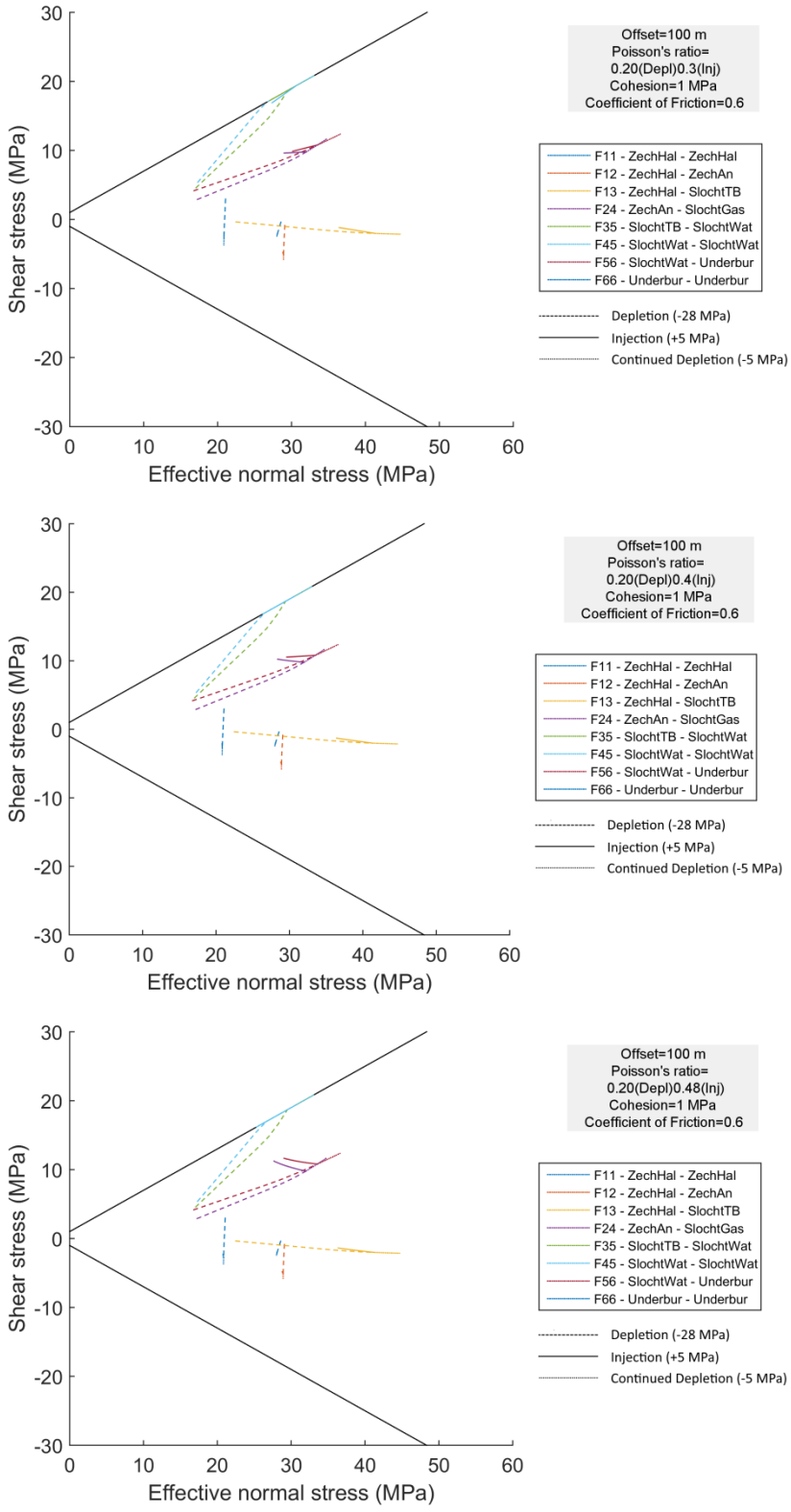

Figure C 11: Stress path for the scenarios of mechanism 3 with $v_{injection}$ = 0.30, $v_{injection}$ = 0.40 and $v_{injection}$ = 0.48, compared to the scenario of ongoing depletion.

Mechanism 3: Ongoing depletion

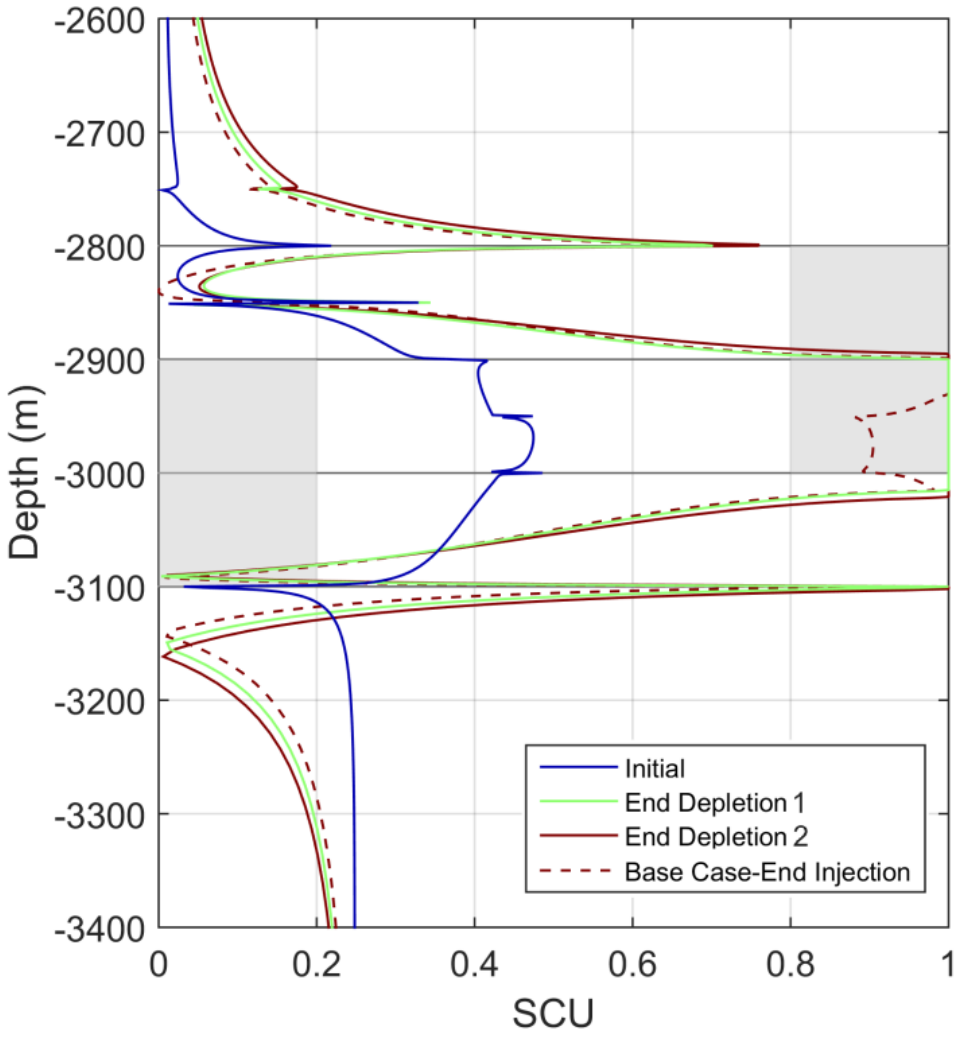

Figure C 12: Shear Capacity Utilization for the scenario of ongoing depletion for mechanism 3 compared to the base case scenario. End Depletion 1 refers to the end of 28 MPa depletion, whereas End Depletion 2 refers to the end of an additional 5 MPa depletion.

D Appendix – Cooling and thermal stresses due to injection of cold nitrogen

Figures and results mechanism 4 – temperature effects

Table D 1: Nitrogen properties at 10 ^{0}C (NIST).

Pressure (bar)	Density (kg/m^3)	Bg (rm^3/sm^3)	Viscosity (cP)
1	1.1903	71.73768	0.017112
11	13.134	6.501409	0.017282
21	25.139	3.396636	0.017463
31	37.187	2.296217	0.017655
41	49.257	1.733584	0.017859
51	61.328	1.392366	0.018076
61	73.38	1.163692	0.018306
71	85.389	1	0.018549
84	100.9	0.834366	0.018885
98	117.43	0.716905	0.019272
112	133.73	0.629542	0.019685
126	149.74	0.562241	0.020122
140	165.42	0.508958	0.020582
154	180.72	0.465853	0.021065
168	195.62	0.430359	0.021567
182	210.1	0.400707	0.022088
196	224.14	0.37561	0.022624
210	237.72	0.354142	0.023174
224	250.86	0.335612	0.023736
238	263.53	0.319465	0.024308
252	275.76	0.305296	0.024888
266	287.55	0.292777	0.025475
280	298.92	0.281647	0.026066
294	309.87	0.271696	0.026661
308	320.42	0.262746	0.027259
322	330.59	0.254664	0.027858
336	340.4	0.247323	0.028458

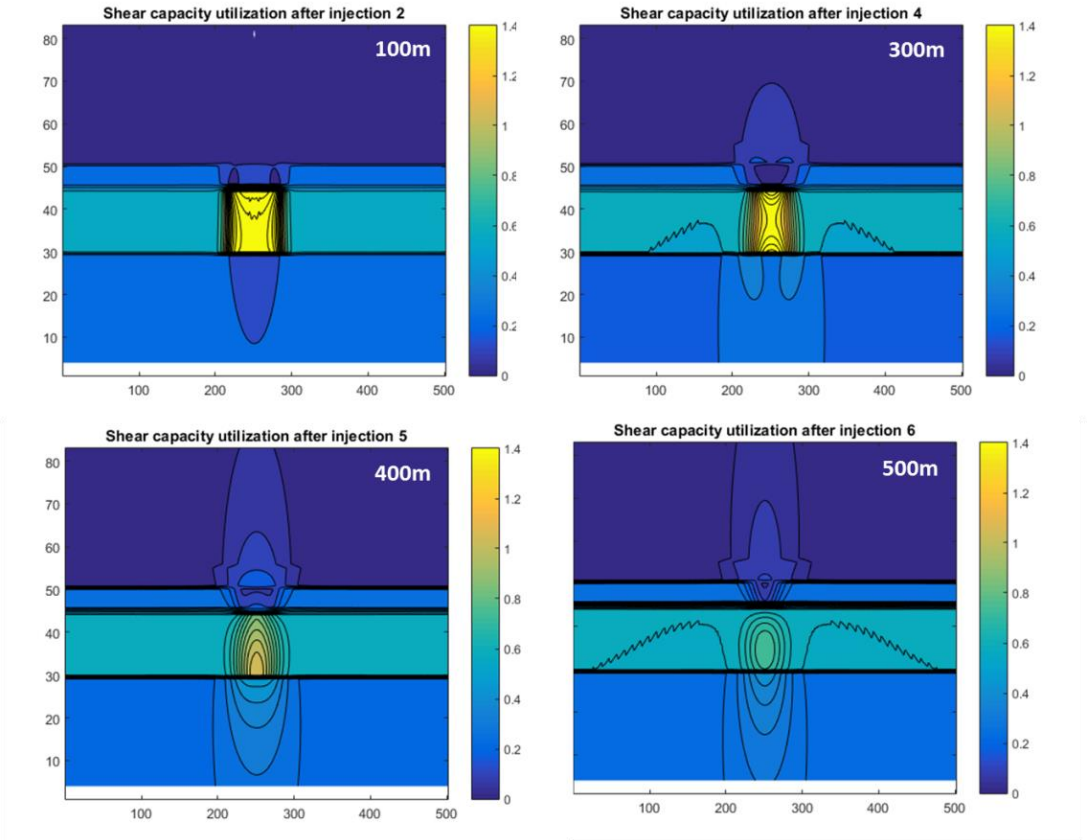

Figure D 1: Shear capacity utilization (SCU) projected onto a fault plane at distance of 100 m, 300 m, 400 m and 500 m from the injection well. Faults dip at 75^0 away from the injection well.

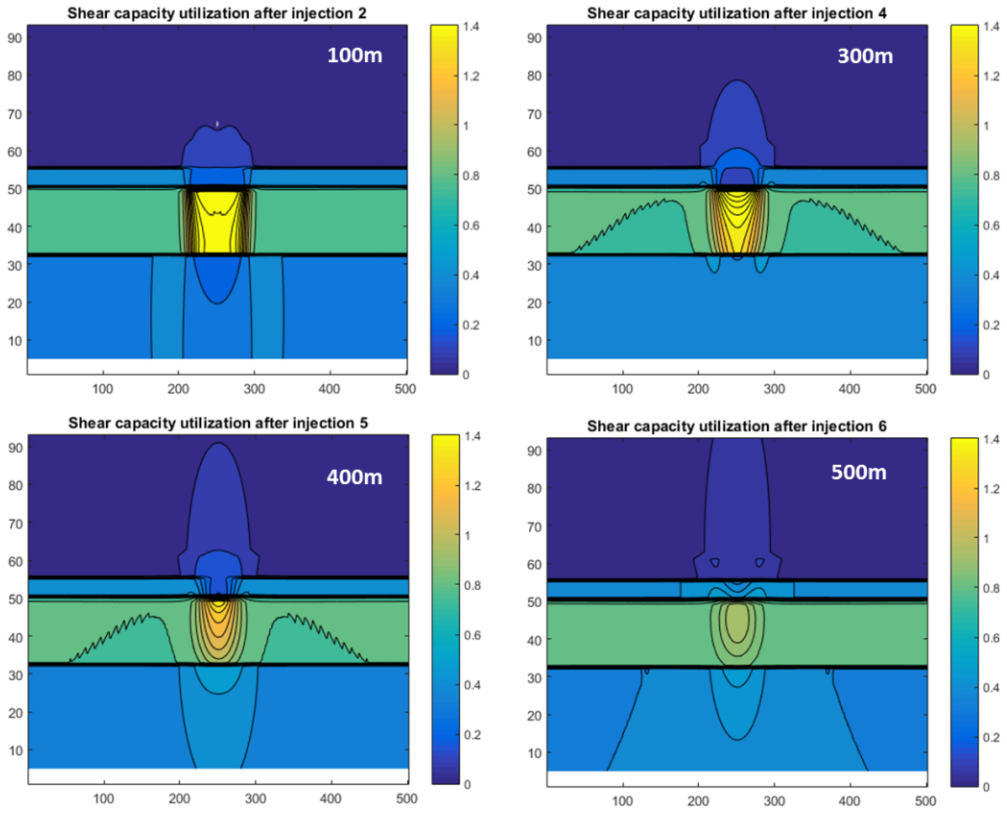

Figure D 2: Shear capacity utilization (SCU) projected onto a fault plane at distance of 100 m, 300 m, 400 m and 500 m from the injection well. Faults dip at 60^0 away from the injection well.

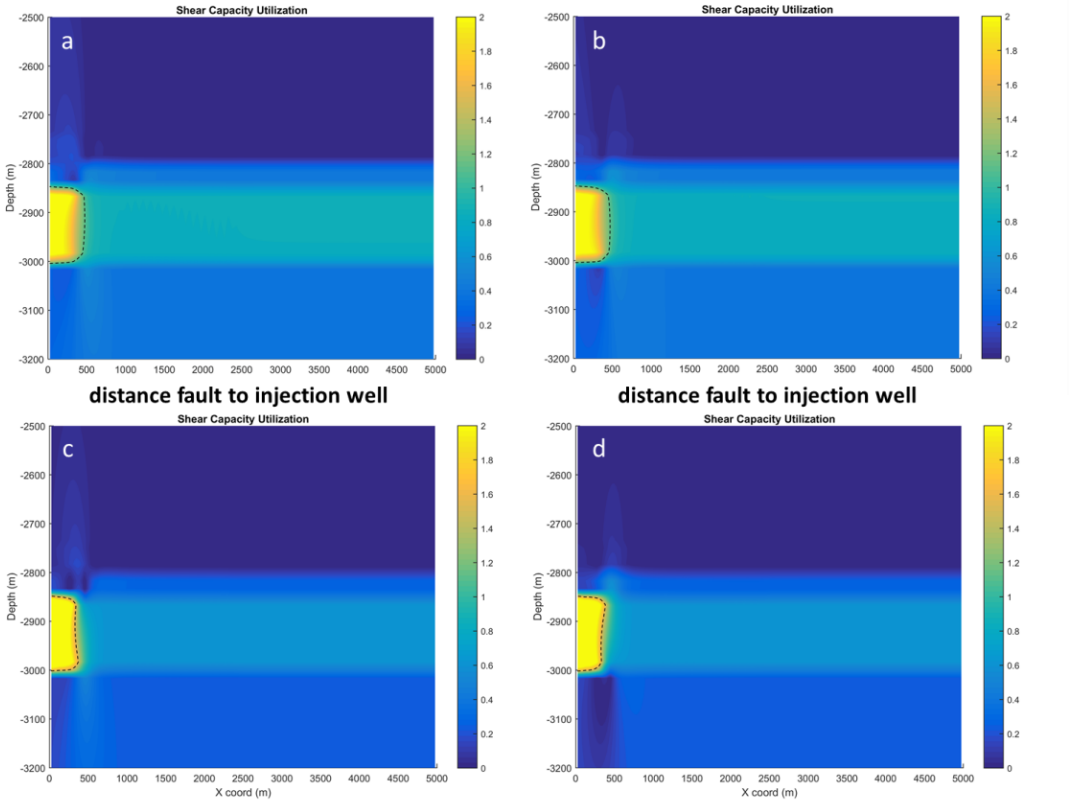

Figure D 3: Shear capacity utilization (SCU) at the end of injection along a vertical section perpendicular to the strike of the faults. a) SCU fault dip 60^0, dip direction away from injection well, b) SCU fault dip 60^0, dip direction towards injection well, c) SCU fault dip 75^0, dip direction away from injection well d) SCU fault dip 75^0, dip direction towards injection well.